THE TRIUMF E497
PARITY VIOLATION EXPERIMENT
IN THE 221 MeV $\vec{p}p$ SYSTEM:
A complete analysis of the Feb97, Jul98, and May99 data runs

By

Jason Bland

A thesis

submitted to the faculty of graduate studies

in partial fulfillment of the requirements

for the degree of

MASTER OF SCIENCE

in

particle/nuclear physics

DEPARTMENT OF PHYSICS AND ASTRONOMY

THE UNIVERSITY OF MANITOBA

WINNIPEG, MANITOBA

CANADA

THE UNIVERSITY OF MANITOBA

FACULTY OF GRADUATE STUDIES

*****

COPYRIGHT PERMISSION PAGE

THE TRIUMF E497 PARITY VIOLATION EXPERIMENT IN THE 221 MeV $\vec{p}p$ SYSTEM: A complete analysis of the Feb97, Jul98 and May99 data runs

BY

Jason Bland

A Thesis/Practicum submitted to the Faculty of Graduate Studies of The University of Manitoba in partial fulfillment of the requirements of the degree of

MASTER OF SCIENCE

Abstract

The longitudinal analyzing power, A_z, has been measured in $\vec{p}p$ elastic scattering at an incident proton energy of 221 MeV. The result obtained is $A_z = (0.84 \pm 0.29(stat.) \pm 0.17(syst.)) \times 10^{-7}$. This experiment is unique in that it selects a single parity-violating transition amplitude ($^3P_2$-$^1D_2$) and consequently constrains the weak meson-nucleon coupling constant h_ρ^{pp}. The experimental value of h_ρ^{pp} is $(-25 \pm 10) \times 10^{-7}$ and is found to be consistent with theoretical predictions, both in sign and magnitude. The experimental result, based on three major data runs, marks the first independent measurement of the h_ρ^{pp} coupling constant.

Acknowledgements

First and foremost, I would like to extend thanks and gratitude to my supervisor and mentor of the past three years. I have learned a great deal from Dr. Shelley Page, not only in regard to this experiment, but also with respect to the graduate student experience-at-large. Dr. Page has taught me the importance of scientific rigour and of maintaining perspective when the experimental results—put simply—did not make any sense. Dr. Page's guidance, particularly over the last twelve months, enabled us to conclude these data and for me to facilitate the writing of this thesis. Thank you.

Another huge thanks goes out to Dr. Jim Birchall for advice on interpreting many statistical issues as well as independently checking many of the crucial aspects of the latter part of the analysis. Thanks Dr. W. T. H. van Oers for your intellectual and moral support.

A special thanks goes to Diane Reitzner and Araz Hamian whose theses were of great help to me as I wrote this thesis. Thanks to the Trailer Aa Parity Lunch club. The lunch club includes Des, Larry, Mike, Trevor, Nikita, Diane, and all visitors and summer students to the trailer. Good luck in the trenches! and thanks all for conversation that never *smelled bad.*

Contents

List of Figures

List of Tables

Chapter 1

Parity non-conservation via weak meson-nucleon coupling

1.1 Introduction

This thesis will present an overview of the TRIUMF E497 parity violation experiment and the final result of the analysis of its three major data runs. The data were acquired during three separate, five week long data taking periods between February 1997 and May 1999.

The aim of the TRIUMF E497 experiment is to observe the weak interaction in intermediate energy proton-proton scattering. The weak nucleon-nucleon (NN) interaction, which is parity non-conserving (PNC), can be characterized at intermediate energy by a sum of amplitudes arising from single meson exchange. Desplanques, Donoghue, and Holstein [1] (DDH) present the first major discussion of the weak amplitudes which determine the parity violating part of the NN interaction by use of the quark model and $SU(6)_W$ symmetry. It is within the specific framework of the quark model that their paper attempts to evaluate the matrix elements arising from a weak meson-NN interaction.

The PNC single meson exchange model is described using one strong, parity conserving (PC) vertex, and one weak, PNC vertex. At the weak vertex, it is assumed that short-range heavy bosons ($W^{\pm}$ and Z^0) decay to form mesons which interact with nucleons at the PC vertex. Figure 1.1 is a Feynman diagram of the weak NN interaction using the weak single meson exchange model.

The reader is encouraged to refer to reference [2] (AAH) for a comprehensive treatment of theoretical considerations relating to this experiment. The purpose of this chapter is to outline a theoretical link between the weak PNC interaction potential and the measured parity violating observable A_z. In $\vec{p}p$ scattering experiments, the parity violating observable is the longitudinal analyzing power A_z and is defined as

$$A_z \equiv \frac{\sigma^+ - \sigma^-}{|P_z|\,(\sigma^+ + \sigma^-)} \tag{1.1}$$

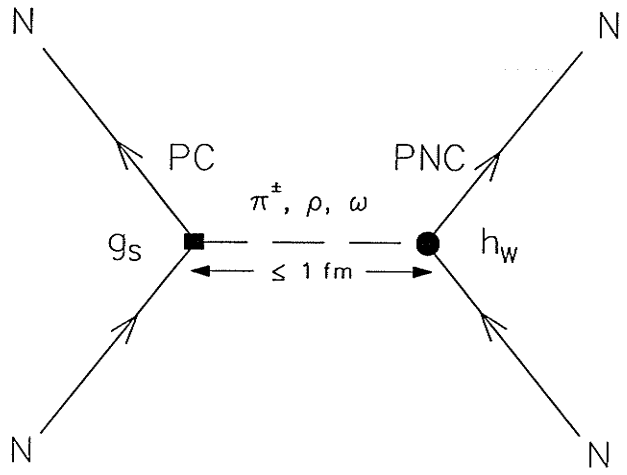

Figure 1.1: *Feynman diagram of weak single meson exchange. Only the $\pi^{\pm}$, ρ, and ω mesons, which are relevant in the context of an intermediate energy weak meson-nucleon exchange model, are shown in the interaction. The square represents the strong vertex and the circle represents the weak vertex of the NN interaction. g_S and h_W are the strong and weak coupling constants, respectively.*

where $|P_z|$ is the *longitudinal beam polarization*, and $\sigma^{\pm}$ is the scattering cross section of the target for helicity ± 1 of the incident proton. Due to the small coupling strength of the weak nuclear force, A_z is expected to be of the order 10^{-7}.

1.2 Weak meson exchange model

In the weak meson exchange model, only low mass mesons are considered, with mass less than 800 MeV/c^2. This is due to the hard core of the strong NN interaction [3]. Since the π^0 mesons are their own anti-particles, they must violate CP conservation if they are parity non-conserving (Barton's theorem); this suppresses their interaction strength by a factor of approximately 2×10^{-3} relative to other interacting mesons and eliminates the π^0 mesons from

consideration in $\vec{p}p$ elastic scattering. The mass, spin and parity (J^P) of the remaining mesons are summarized in Table 1.1 [4].

Meson	J^P	Mass (MeV)
$\pi^{\pm}$	0^-	140
ρ	1^-	770
ω	1^-	782

Table 1.1: *The mesons comprising the weak NN meson exchange model [4].*

Multiple meson exchange, such as the 2π, can contribute to the interaction potential; however, these terms are often ignored due to their small coupling amplitude [1]. The predicted contribution of the 2π exchange to A_z is at least an order of magnitude smaller [5] than other meson exchange contributions based on an intermediate state $N\Delta$ excitation model [6] and energy considerations [2]. Thus, only single meson exchange, in the form of π, ρ, and ω mesons are included in the basic PNC interaction potential. The weak PNC interaction potential in the single meson exchange model takes the form

$$V^{PNC} = V_\pi + V_\rho + V_\omega \,. \tag{1.2}$$

1.3 Weak meson-nucleon coupling constants

At low and intermediate interaction energies, the coupling constants governing the strong NN interaction are well understood. The knowledge of the strong coupling is exploited in determining the coupling of the weak NN interaction. This is accomplished by replacing one PC vertex in the strong NN interaction by a weak PNC vertex (as shown in Figure 1.1) and replacing the corresponding strong coupling constant, g_S, by the weak coupling constant, h_W.

The PNC potential (equation 1.2) is derived using the quark model approach and $SU(6)_W$ symmetry [1]. The weak meson-nucleon coupling con-

stants are then found by evaluating matrix elements of the form, e.g. $\langle p|H_W|n\pi^+\rangle = f_\pi$ for the weak pion nucleon coupling at the NN vertices.

The model assumes that at the weak vertex, the $W^\pm$ and Z^0 bosons (left-handed particles which violate parity) decay to the longer-range exchange mesons. The exchange mesons are responsible for mediating the strong interaction at the strong vertex. The PNC potential for a pair of interacting nucleons is given by [1]

$$\begin{aligned} V_{12}^{PNC} &= \frac{f_\pi g_{\pi NN}}{2\sqrt{2}} i(\vec{\tau}_1 \times \vec{\tau}_2)_z (\vec{\sigma}_1 + \vec{\sigma}_2)\cdot \vec{u}_\pi \\ &\quad -g_\rho (h_\rho^0 (\vec{\tau}_1\cdot\vec{\tau}_2) + \frac{h_\rho^1}{2}(\vec{\tau}_1+\vec{\tau}_2)_z + \frac{h_\rho^2}{2\sqrt{6}}(3\tau_{1z}\tau_{2z} - \vec{\tau}_1\cdot\vec{\tau}_2)) \\ &\quad \times ((\vec{\sigma}_1 - \vec{\sigma}_2)\cdot\vec{v}_\rho + i(1+\chi_v)(\vec{\sigma}_1\times\vec{\sigma}_2)\cdot\vec{u}_\rho) \\ &\quad -g_\omega (h_\omega^0 + \frac{h_\omega^1}{2}(\vec{\tau}_1+\vec{\tau}_2)_z)\times((\vec{\sigma}_1-\vec{\sigma}_2)\cdot\vec{v}_\omega + i(1+\chi_s)(\vec{\sigma}_1\times\vec{\sigma}_2)\cdot\vec{u}_\omega) \\ &\quad -\frac{1}{2}(g_\omega h_\omega^1 - g_\rho h_\rho^1)(\vec{\tau}_1-\vec{\tau}_2)_z(\vec{\sigma}_1+\vec{\sigma}_2)\cdot\vec{v}_\rho \\ &\quad -\frac{g_\rho h_\rho'^1}{2} i(\vec{\tau}_1\times\vec{\tau}_2)_z(\vec{\sigma}_1+\vec{\sigma}_2)\cdot\vec{u}_\rho \end{aligned} \tag{1.3}$$

where the subscripts 1 and 2 represent nucleons 1 and 2, respectively. The $\vec{u}_\nu$ and $\vec{v}_\nu$ are the following commutation and anticommutation operations, respectively:

$$\vec{u}_\nu = \left[\frac{\vec{p}_1 - \vec{p}_2}{2M}, f_\nu(r)\right]$$

$$\vec{v}_\nu = \left\{\frac{\vec{p}_1 - \vec{p}_2}{2M}, f_\nu(r)\right\}$$

in which $\vec{p}_1$ and $\vec{p}_2$ are the nucleon momenta, and M is the nucleon mass. The functions

$$f_\nu(r) = \frac{1}{4\pi r} e^{-m_\nu r}, \quad \nu = \pi, \rho, \omega \tag{1.4}$$

are the Yukawa potentials for mesons ν with masses m_ν. The h_ν^i are the weak coupling constants for mesons ν with isospin change of $\Delta I = i$. The coupling constant f_π is the weak pion coupling constant which is purely isovector;

therefore, $\Delta I = 1$ and the superscript is omitted. The other symbols in equation 1.3 are: g_ν, the strong coupling constant for meson ν; σ_i, the Pauli spin matrices for nucleon i; τ_i, the isospin matrices for nucleon i; and χ_s/χ_v, the isoscalar/isovector nucleon anomalous magnetic moments.

From equation 1.3, it is seen that there exist seven independent weak coupling constants: $(f_\pi, h^0_\rho, h^1_\rho, h^2_\rho, h^0_\omega, h^1_\omega, h'^1_\rho)$. The prediction of the weak coupling constants is very difficult from first principles due to uncertainties in how the bare weak couplings are renormalized by the strong interaction. For this reason, DDH quote "best guess" values of h_W and "reasonable ranges" corresponding to realistic theoretical uncertainties at the $\pm 100 - 200\%$ level.

For this analysis, h'^1_ρ is predicted, on the scale of the other coupling constants, to be small [7] and is assigned a value of zero. Thus, there are, effectively, six unknown weak coupling constants in this sector. As stated above, TRIUMF E497 is a proton-proton scattering experiment, thus charge conservation prevents $\pi^\pm$ exchange in the interaction. This excludes the f_π coupling constant from contributing to the PNC effect in this experiment.

Table 1.2 summarizes the experimental best fit determination of the weak coupling constants as determined by Adelberger and Haxton [3] (AH). AH used the theoretical formalism of DDH for the Glashow-Weinberg-Salam model and the experimental results of three independent measurements of A_z at 13.6 MeV [8], 45 MeV [9], and 800 MeV [10]; together with other nuclear parity violation data in order to constrain the most likely values of the weak coupling constants.

The effective coupling constants involved in weak meson exchange in the proton-proton system are linear combinations of the weak constants and given by:

$$h^{pp}_\rho = h^0_\rho + h^1_\rho + h^2_\rho/\sqrt{6} \quad and$$
$$h^{pp}_\omega = h^0_\omega + h^1_\omega \,. \tag{1.5}$$

These five coupling constants, relevant to experiments measuring $\vec{p}p$ elastic scattering, are all allowed on the basis of isospin conservation. The total isospin of the $\vec{p}p$ system is $I = 1$, therefore, interactions may proceed via intermediate states $\Delta I = 0, 1, 2$.

Weak coupling	Range [1]	"Best guess" value [1]	Experimental best fit [2]
f_π	$0 \rightarrow 11$	4.6	0.8
h_ρ^0	$-31 \rightarrow 11$	-11.4	-11.2
h_ρ^1	$-0.4 \rightarrow 0.4$	-0.19	-0.3
h_ρ^2	$-10 \rightarrow -6$	-9.5	-7.3
h_ω^0	$-12 \rightarrow 3$	-1.9	-8.2
h_ω^1	$-3 \rightarrow -1$	-1.1	-2.5
h_ρ^{pp}	$-35 \rightarrow 14$	-15.5	-14.5
h_ω^{pp}	$-14 \rightarrow 2$	-3.0	-10.7

Table 1.2: *Theoretical predictions [1] and experimental best fit values of the weak coupling constants following the procedure of AH [2] in units of* 10^{-7}. *The values in the "best guess" and best fit column have relative uncertainties of a few hundred percent.*

The TRIUMF E497 experiment is designed to isolate the h_ρ^{pp} coupling constant by measuring A_z at the zero-crossing energy of the $^1S_0$-$^3P_0$ partial wave amplitude. The significance of the beam energy choice in this experiment will be presented in the remaining sections of this chapter.

1.4 Longitudinal Analyzing Power, A_z

A natural digression at this juncture is to discuss the longitudinal analyzing power and parity violating observable, A_z. The longitudinal analyzing power is a dimensionless quantity which is proportional to the dependence of the scattering cross section in $\vec{p}p$ interactions on the helicity of the polarized beam.

The helicity, H, of a particle is defined as the fraction of the component of the particle spin in the momentum direction using a righthanded coordinate system. Thus,

$$H \equiv \frac{\vec{s} \cdot \vec{p}}{sp} = P_z \,, \tag{1.6}$$

where $\vec{s}$ and $\vec{p}$ are the particle spin and momentum, respectively.

The range of values the helicity of a particle can take is $(-1 \rightarrow +1)$. For example, a particle with spin axis parallel to its momentum has a helicity of $+1$. In contrast, if a parity inversion is performed on the coordinate system, then the radial vector, $\vec{r}$, is inverted such that

$$\vec{r} \rightarrow -\vec{r} \,,$$

which leads to the transformation:

$$\vec{p} \rightarrow -\vec{p} \quad and$$
$$\vec{s} \rightarrow \vec{s} \,;$$

where $\vec{p} = m\, d\vec{r}/dt$, and $\vec{s}$ is an angular momentum which transforms like the cross product of position and momentum, and does not change sign under a parity inversion. Thus, the helicity will change sign under a parity inversion.

If any dependence exists on particle helicity in the $\vec{p}p$ interaction then the interaction is said to be PNC, or parity violating. The form of the PNC scattering cross-section is

$$\sigma^{\pm} = \sigma^0 \left(1 + P_z A_z\right) \,, \tag{1.7}$$

where σ^0 is the unpolarized scattering cross-section determined by the strong nuclear interaction and the longitudinal polarization, P_z, is ± 1. It is immediately apparent that if P_z changes sign, then the scattering cross-section will also change by an amount proportional to the longitudinal analyzing power A_z.

In general, the weak PNC potential, described at the end of section 1.2, can be used to predict parity violating observables. The observables have the form

$$A^{PNC} = h_W \langle f | V^{PNC} | i \rangle \, ,$$

where h_W is a linear combination of the seven weak meson-nucleon coupling constants, and $\langle f|$ and $|i\rangle$ are the final and initial wave functions for the NN system, respectively. For the TRIUMF E497 experiment, the effective coupling constant in the above relation is the h_ρ^{pp} coupling constant.

1.5 TRIUMF E497 beam energy and partial wave analysis

The longitudinal analyzing power in $\vec{p}p$ scattering can also be described using a sum of parity-mixed partial wave scattering amplitudes. Using $^{(2S+1)}L_J$ notation, the three lowest PNC partial waves are the $^1S_0$-$^3P_0$, $^3P_2$-$^1D_2$, and $^1D_2$-$^3F_2$. These transitions are allowed by requiring that the total $\vec{p}p$ wavefunction be anti-symmetric in the interaction, and angular momentum conservation. Higher partial wave contributions are assumed to be insignificant at interaction energies lower than the pion production threshold (280 MeV).

At energies less than pion production, A_z is effectively a linear combination of the three lowest partial wave amplitudes. Moreover, the $^1D_2$-$^3F_2$ transition is insignificant in relation to the other two available transitions at interaction energies less than 1000 MeV [11]. Figure 1.2 shows a prediction of the three lowest partial wave contributions to the total A_z at low and intermediate energies. The contributions of the three partial wave amplitudes in $\vec{p}p$ elastic scattering that are shown in the figure were calculated by Driscoll and Miller [11] (DM) using the DDH "best guess" weak coupling constants [1]. Of important

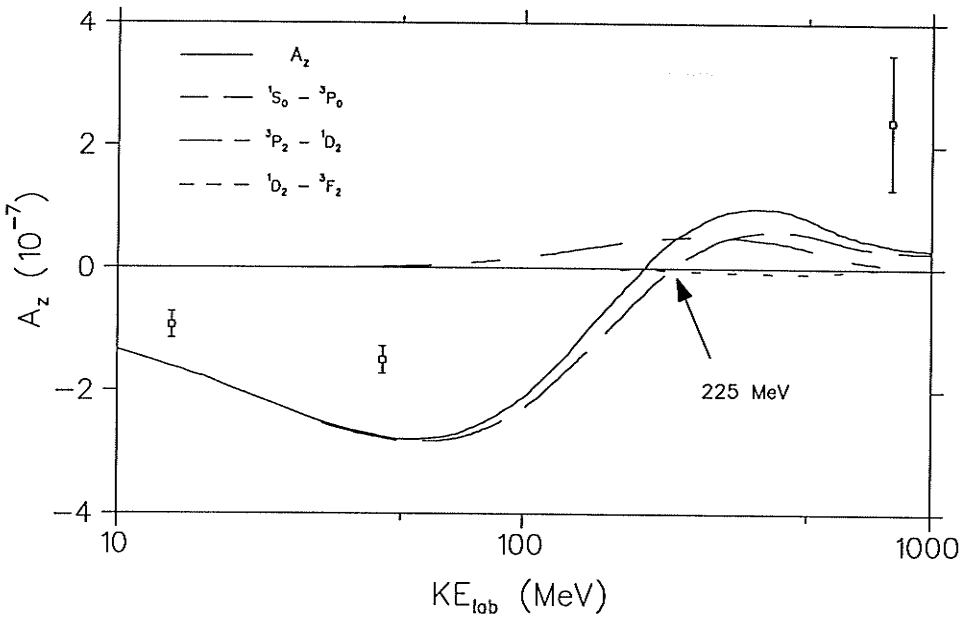

Figure 1.2: *The three lowest partial wave contributions to the total A_z at low and intermediate energies as predicted by DM [11] using the DDH "best guess" coupling constants [1]. The TRIUMF E497 experiment is conducted with an incident proton energy of 221 MeV_{lab} which corresponds to the zero crossing energy of the $^1S_0$-$^3P_0$ partial wave amplitude. Also shown are three other high precision measurements of A_z at other energies [8][9][10].*

note in the figure is the zero crossing energy of the $^1S_0$-$^3P_0$ transition at 225 MeV. The zero crossing energy is determined by the strong interaction phase shifts and corresponds to infinitesimal target thickness and perfect detector geometry. The zero crossing energy corresponds to an incident (lab) proton energy of 221 MeV averaged over the geometry of the TRIUMF E497 experimental apparatus [12]. Thus, the TRIUMF E497 experiment will attempt to determine A_z at an energy for which the $^3P_2$-$^1D_2$ partial wave amplitude essentially dominates.

The $^3P_2$-$^1D_2$ partial wave amplitude at the $^1S_0$-$^3P_0$ zero-crossing energy depends only on ρ meson exchange [11][13]. Thus, a measurement of A_z in $\vec{p}p$ scattering at 221 MeV will also, in theory, isolate the h_ρ^{pp} weak coupling

constant. Integrating over the detector acceptance from 0° to 90° (center of mass) gives [14]

$$h_\rho^{pp} = -30.2 A_z \, . \tag{1.8}$$

Comparing with Table 1.2, using DDH "best guess" couplings and reasonable ranges for h_ρ^{pp}, together with the DM calculation, the predicted longitudinal analyzing power at 221 MeV becomes

$$A_z = (0.5^{+0.7}_{-1.0}) \times 10^{-7} \, . \tag{1.9}$$

An alternative mechanism for a PNC meson exchange interaction is provided by Iqbal and Niskanen [15] (IN). In this model, PNC effects occur due to weak boson exchange between quarks within the exchanged mesons. From this mechanism alone, IN predicted an A_z of approximately 0.6×10^{-7} at the TRIUMF E497 energy. A later analysis [16] extended the model to include Δ isobar excitation in pp scattering and when adding this contribution to the DM meson exchange calculation, the predicted longitudinal analyzing power at 221 MeV becomes $A_z = 0.8 \times 10^{-7}$.

The TRIUMF E497 experiment was originally designed to measure A_z to a total uncertainty of $\pm 0.2 \times 10^{-7}$ in transmission geometry [17]. At this level of precision, the sign of h_ρ^{pp} should be determined, and the experimental uncertainty will be comparable to the high precision measurements of A_z shown in the above figure. The particular significance of the TRIUMF E497 experiment is that it attempts, for the first time, to isolate the h_ρ^{pp} coupling constant by measuring A_z at the $^1S_0$-$^3P_0$ zero crossing energy. By combining the results of the lower energy experiments, which have determined linear combinations of h_ρ^{pp} and h_ω^{pp}, with the TRIUMF E497 result, further constraints can be placed on the weak meson nucleon coupling constants.

Chapter 2

TRIUMF E497

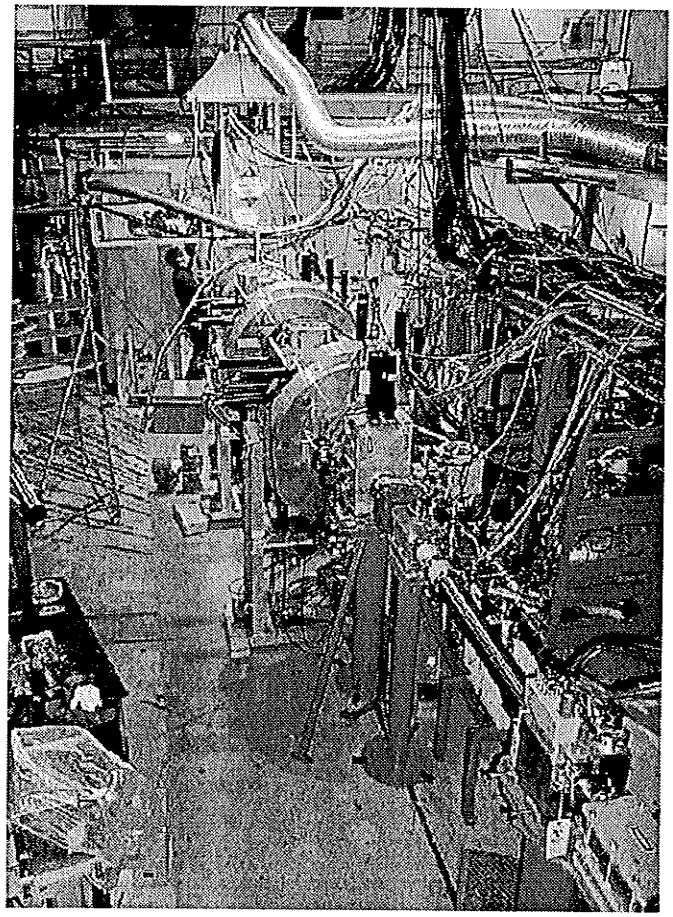

Figure 2.1: *A parity collaborator inspects the main LH_2 coolant line [18].*

2.1 Experimental method and apparatus

The method by which the measurement is performed is a "transmission mode" measurement where the difference in the transmission of longitudinally polarized protons through a liquid hydrogen target is measured for the two helicity states of the incident polarized proton beam. The transmission, $T^{\pm}$, through a thin target is given by

$$T^{\pm} = \exp^{-\sigma^{\pm} nl} \simeq 1 - \sigma^{\pm} nl = 1 - S^{\pm}$$

where n is the number density and l is the length of the target. Recall, from equation 1.1 that:

$$A_z = \frac{\sigma^+ - \sigma^-}{|P_z|\,(\sigma^+ + \sigma^-)}\,.$$

Therefore,

$$A_z = \frac{(\sigma^+ - \sigma^-)\,nl}{2|P_z|S}$$

where S is the average fraction of scattered protons. The transmission asymmetry is given by

$$A_t = \frac{T^+ - T^-}{T^+ + T^-} = -\frac{(\sigma^+ - \sigma^-)\,nl}{2T}$$

where T is the average fraction of transmitted protons. Thus, the parity violating difference in the transmission of a beam with longitudinal polarization $|P_z|$ is given by

$$A_t = -\frac{S}{T}|P_z|A_z \tag{2.1}$$

where A_t is the measured scattering difference. With $S = 0.04$, and $T = 0.96$, $A_t \sim 10^{-9}$.

The layout of the TRIUMF E497 experimental apparatus is shown in Figure 2.2. The experimental apparatus is composed of three main systems: (i) polarized ion source, (ii) cyclotron, and (iii) target and detector system. A brief discussion of these three systems and their subcomponents is presented in the remainder of this section. The rest of the chapter discusses the data acquisition system and presents the systematic errors which are expected to occur during the measurement of A_z.

2.1.1 Optically pumped polarized ion source *OPPIS*

The TRIUMF optically pumped polarized ion source (OPPIS) [19] produces a longitudinally polarized H^- source beam for injection into the cyclotron.

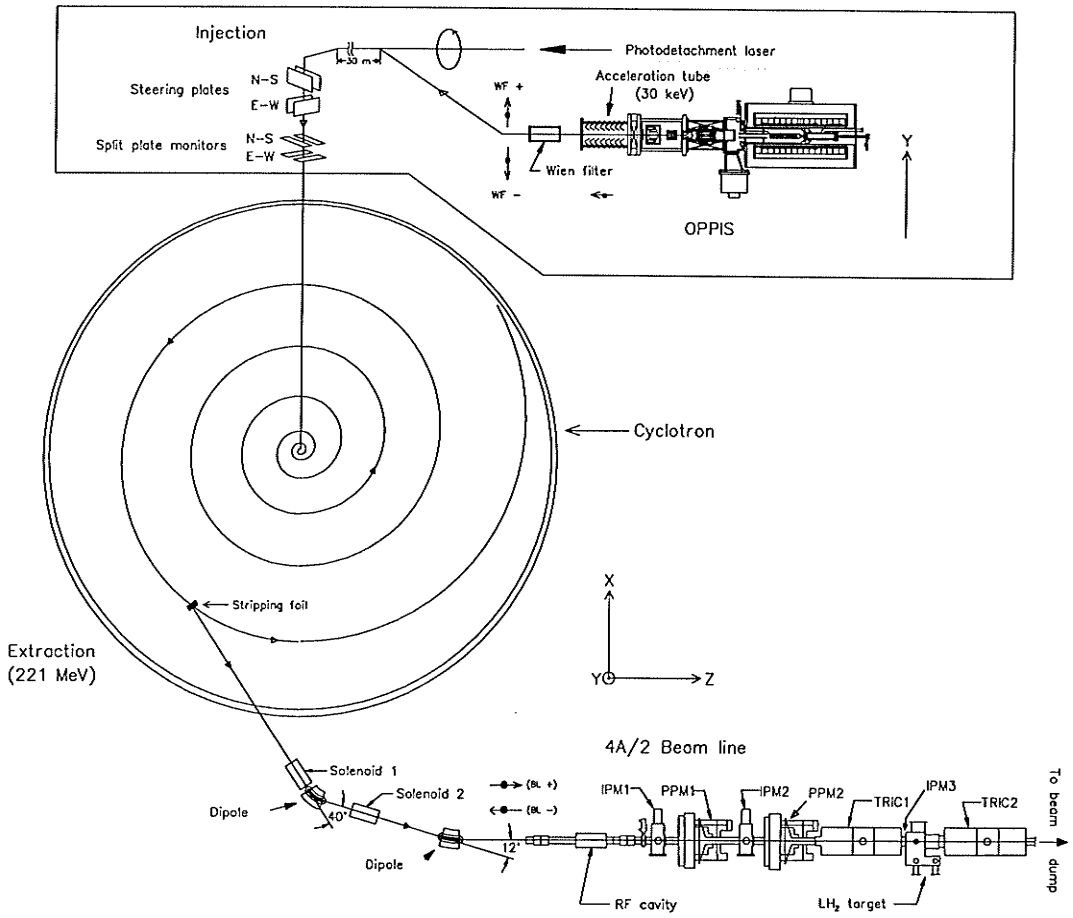

Figure 2.2: *The TRIUMF E497 experimental apparatus.*

Figure 2.3 shows the main components of OPPIS. The main components include: an electron cyclotron resonance cavity (ECR), optically pumped rubidium vapour cell, Sona transition region [20], and a sodium vapour ionizer cell. A more thorough examination of the physics and operation of the optically pumped ion source and its optimization for this experiment is presented in an M.Sc. thesis [21]. Here, the main components of the source and injection system related to the production of the polarized H^- beam are briefly discussed.

Protons (H^+) of 3 keV energy are extracted from the ECR plasma cavity. The protons are accelerated toward the optically pumped rubidium cell where they pick up a polarized electron ($\vec{e}^-$). The electrically neutral hydrogen atoms

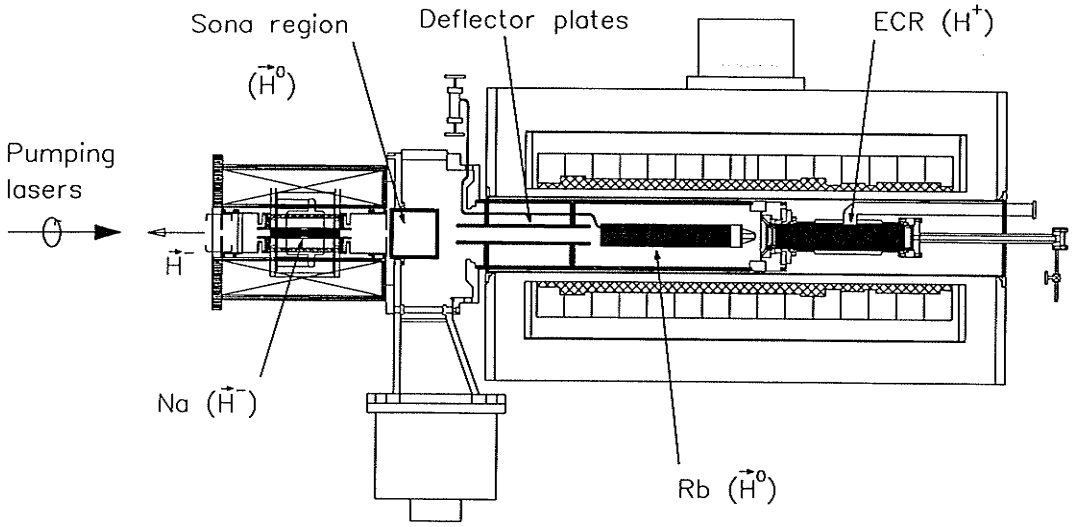

Figure 2.3: *The TRIUMF optically pumped polarized ion source (OPPIS). The ion source produces nuclear-polarized hydrogen ions for acceleration into the cyclotron.*

(H^0) are then subjected to a diabatic magnetic field reversal (Sona transition region) where the spin of the $\vec{e}^-$ is effectively transferred to the H^0 nucleus. In the sodium cell, an additional electron is picked up by the nuclear-polarized hydrogen atom ($\vec{H}^0$) and the *negative ion* ($\vec{H}^-$) is electrostatically accelerated to 300 keV and injected into the cyclotron.

The polarization of the electrons in the rubidium vapour is reversed every 25 ms by changing the frequency of the light produced by the pumping lasers. The deflector plates sweep away any charged species which remain in the beam between the rubidium neutralization cell and the Sona transition region.

ECR plasma cavity

The ECR plasma cavity contains neutral hydrogen atoms in a magnetic field of 1 Tesla. During operational mode, 800 W of 28 GHz microwaves are applied to the cavity at the electron cyclotron resonance frequency thus creating energetic electrons in the cavity. The energetic electrons ionize the surrounding

hydrogen gas—creating a hydrogen plasma. The cavity is embedded within a superconducting solenoid and 3 kV high voltage field which accelerates the H^+ toward the neutralization cell.

Rb neutralization cell

The protons created and accelerated by the ECR cavity enter the optically pumped rubidium neutralization cell and pick up a polarized electron from the rubidium vapour through charge exchange. The charge exchange reaction is given by

$$\vec{Rb} + H^+ \longrightarrow Rb^+ + \vec{H^0}\,.$$

The rubidium cell is subjected to a 2.5 Tesla magnetic field which induces Zeeman splitting of the energy levels of the rubidium atom's n=5 valence electron. In the 2.5 Tesla regime, the Zeeman splitting leaves an energy gap between the $^2S_{1/2}$ ground state and the $^2P_{1/2}$ 1st excited state of the n=5 valence electron (using $^{(2S+1)}L_J$ notation). The transition energy corresponds to a photon with a frequency of approximately 377.11 THz. The Zeeman fine splitting of magnetic spin states for these energy levels leads to a further splitting of transition energy of 46.75 GHz. The valence electron is then polarized by an optical pumping process. Figure 2.4 shows a schematic of the Zeeman splitting of the energy levels of the valence electron.

The pumping process works by supplying energy to the valence electron and exciting the electron to a higher energy level. Excitation energy is supplied by two 9 W titanium-sapphire (TiS) lasers. The lasers are tuned to frequencies of light at 377.16 THz for spin up and 377.06 THz for spin down. The excited electrons decay to the ground state (in 1 ns) with equal probability of occupying either spin state of the $^2S_{1/2}$ ground state. However, since the pumping lasers are very intense, they effectively depopulate one of the two magnetic

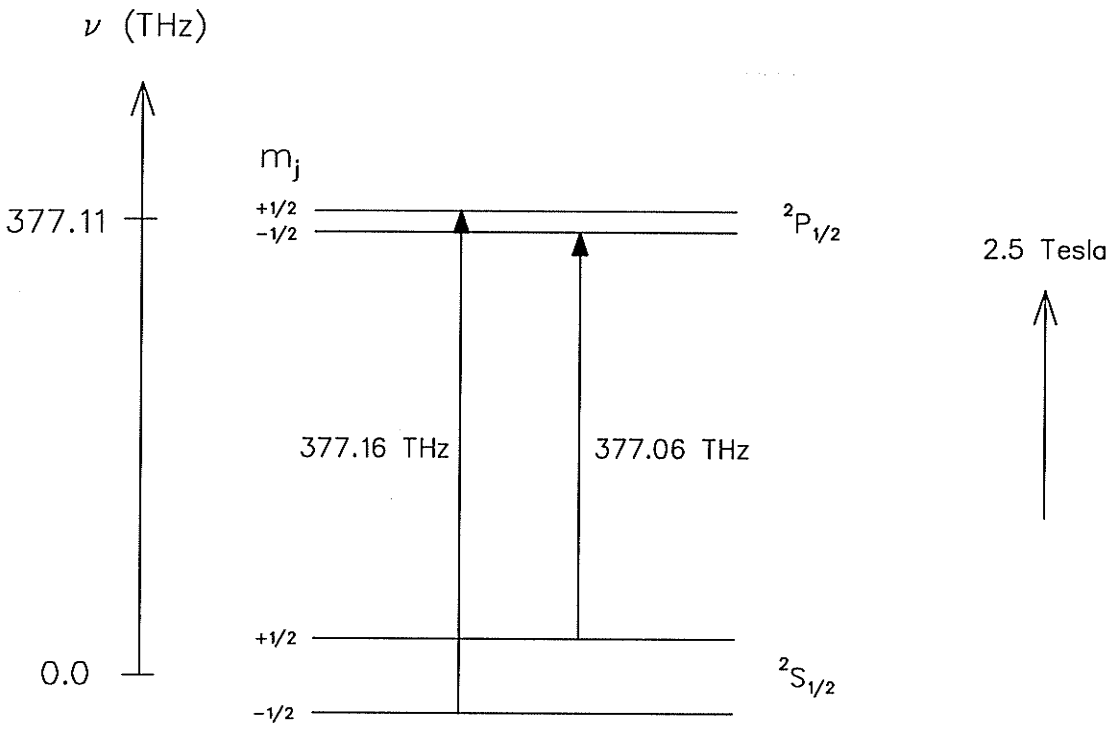

Figure 2.4: *Zeeman splitting of the n=5 valence electron energy levels in the rubidium atom in a 2.5 Tesla magnetic field. The diagram is not to scale. The population of valence electrons with a particular spin in the ground state can be altered by optical pumping.*

substates of the $^2S_{1/2}$ ground state level. Figure 2.5 shows a schematic of the pumping laser system. The pumping lasers polarize the valence electrons in the longitudinal direction with respect to the momentum direction of the incoming H^+ beam.

During regular data taking, the frequency of the pumping lasers must be carefully tuned to produce the same polarization in the rubidium cell in the two polarization states of the source. A systematic polarization mismatch between the two helicity states will produce an intensity modulation of the source beam which is correlated to the spin switching pattern. Intensity modulation will lead to a systematic error in the measurement of A_z. Refer to section 2.4 for a discussion of the systematic errors which originate at OPPIS.

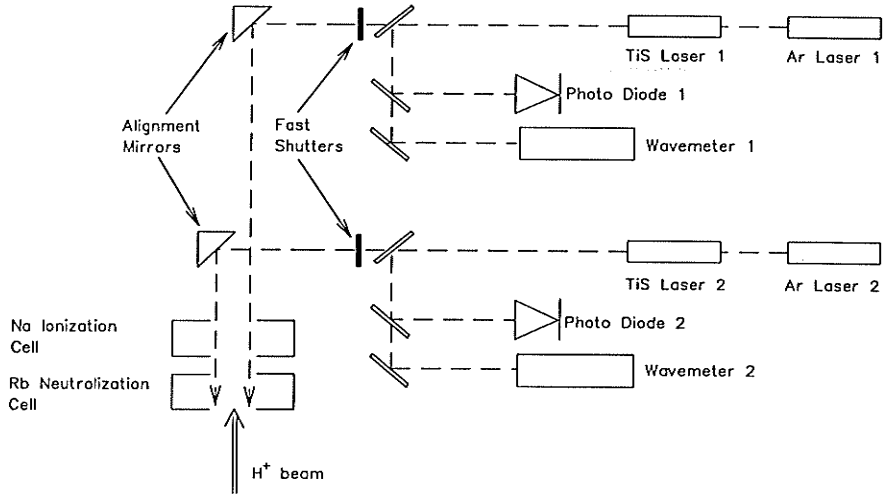

Figure 2.5: *The TRIUMF OPPIS laser system [2]. The helicity of the beam—which depends on the frequency of light used to optically pump the rubidium vapour—is reversed between longitudinally forward and backward every 25 ms. The spin state sequence is controlled by the parity data acquisition system.*

Faraday rotation measurement system

The function of the Faraday rotation measurement system is to measure the thickness and electronic polarization of the rubidium vapour cell [22]. The measurement is performed by exploiting the optical qualities of the rubidium vapour.

Due to the high magnetic field in the cell, the gas becomes optically active and rotates the plane of polarization of linearly-polarized light which propagates through the cell. This effect is called Faraday rotation. Figure 2.6 shows the Faraday rotation measurement system.

In the measurement system, an argon laser pumps a titanium-sapphire probe laser which emits 100 mW light at a frequency of 384.22 THz. This frequency corresponds to the $^2P_{3/2}$-$^2S_{1/2}$, or "D_2", transition in the rubidium atom's valence electron energy levels. The TiS probe laser is not tuned to the D_1 transition (which is used to optically pump the rubidium vapor) because the

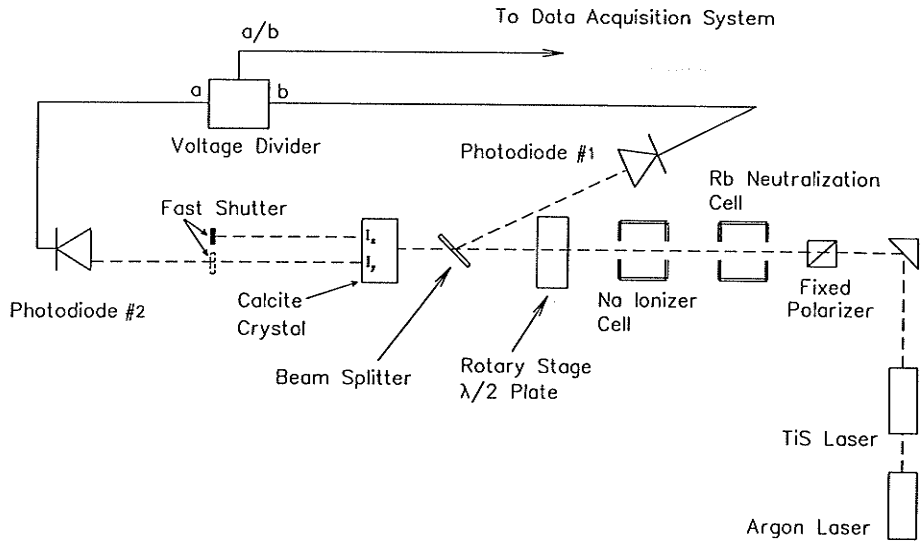

Figure 2.6: *Schematic of the Faraday rotation measurement system [21]. The measurement determines the polarization and thickness of the rubidium cell.*

pumping lasers would create too large a background signal and could damage the photodetector [21].

The probe light is linearly polarized and transmitted along the longitudinal axis of the rubidium cell. Due to the Faraday effect, the plane of polarization of the probe light is rotated by an angle θ after traversing the rubidium cell.

The angle of rotation for polarized rubidium is given by

$$\theta = \theta_0 + P_c \Delta\theta \,, \tag{2.2}$$

where θ_0 is the Faraday rotation for the probe light in an unpolarized rubidium cell, P_c is the polarization of the rubidium cell as a fraction of unity, and $\Delta\theta$ is the additional rotation due to the polarization in the cell. Equation 2.2 can be rewritten in terms of the polarization as

$$P_c = \frac{1}{\alpha}\left(\frac{\theta - \theta_0}{\theta_0}\right) \,, \tag{2.3}$$

where $\alpha = \frac{\Delta\theta}{\theta}$ is a constant under the normal operating conditions of the rubidium cell. During typical operating conditions $\theta_0 \simeq 3.2°$, and $\alpha = -3.118 \pm 0.001$ [2].

The angle of rotation is measured by splitting the probe laser light into two orthogonally polarized components (I_x and I_y) and comparing the intensity of each component to the total probe laser intensity. The probe light is split by passing through a birefringent calcite crystal. A fast shutter blocks one of the two orthogonal components of the probe light from photodiode #2 and the resulting intensity is compared to the intensity at photodiode #1. Measurements of the polarization are normalized by comparing the intensity at photodiode #2 to the intensity at photodiode #1 using an analog voltage divider. The signal from the divider is processed by a voltage to frequency, (V:F), converter and sent to the parity data acquisition system. The rotation angle is given by

$$\theta = Tan^{-1}\left(\sqrt{\frac{I_y}{I_x}}\right) . \tag{2.4}$$

The unpolarized rotation angle θ_0 is measured by blocking the pumping lasers. θ_0 is related to the thickness of the rubidium cell through a constant of proportionality called the Verdet constant. The Verdet constant is a function of the probe laser frequency, the transition frequency and the magnetic field strength in the rubidium cell. The relation is given by

$$\theta_0 = VNl\,, \tag{2.5}$$

where V is the Verdet constant and Nl is the vapour thickness in cm^{-2}. During typical operating conditions $V = 1.121 \times 10^{-13}\ cm^2$ [2].

Sona transition region and sodium ionizer cell

The Sona transition region is a diabatic magnetic field reversal region. In this region, the spin polarization of the electron in the $\vec{H}^0$ atom is transferred to the proton via the Sona transition. The optical pumping process prepares a population of polarized valence electrons. When the electrons combine with

H^+ to form neutral hydrogen atoms, the spins of the two particles can couple to create total spin angular momentum of either 1 or 0 units of $\hbar$.

In the transition region, the magnetic field reverses direction quickly enough to prevent the spin 1 state from precessing about the radial field components (which arise as a result of the field reversal). However, the field must also reverse slowly enough to permit a quantum mechanical evolution of the spin 0 state atoms. In the latter case, the spin of the electron and proton also reverse. OPPIS has been designed to meet these requirements. Protons exiting the transition region are polarized in the direction of the polarized electrons in the Rb neutralization cell.

Approximately 10% of the nuclear-polarized $\vec{H}^0$ atoms pickup an additional electron through charge exchange with sodium atoms in the sodium vapour ionization cell. The charge exchange reaction is given by

$$Na + \vec{H}^0 \longrightarrow Na^+ + \vec{H}^- \, .$$

Upon exiting the sodium cell, the 3 keV beam intensity has been reduced to 40 μA from 20 mA at the ECR cavity.

Injection

The 40 μA beam is accelerated to 300 keV and diverted into the injection line by electrostatic benders. Any neutral atoms that remain in the beam after the ionization cell are effectively removed from the beam. The beam passes through an elaborate transport system with many slits and collimation devices, and the intensity is reduced to approximately 8 μA at the entrance to the cyclotron.

The injection line is approximately 35 metres in length and contains many steering and focusing elements. Along the injection line there are also two N-S and two E-W steering plates which are integrated into a feedback system.

The plates, along with quadrupole magnets, steer and focus the beam into the center of the cyclotron. The feedback system is designed to compensate for small, slow drifts of the beam intensity by changing the amount of current injected into the cyclotron. The maximum range of this system is $\pm 2nA$; for a nominal beam intensity of $200nA$ at the parity apparatus, the feedback system reduces the effect of non-linearity of the detector response. Split plate monitors also exist in the injection line which monitor the stability of the beam position. Two other main components in the injection system include a Wien filter and photodetachment laser.

The function of the Wien filter is to rotate the longitudinal polarization of the hydrogen nuclei in the beam to the vertical direction relative to the plane of the cyclotron and is tuned for maximum polarization of the extracted beam. Particle spin in the vertical direction will not precess during acceleration in the cyclotron because the magnetic field in the cyclotron is vertical.

It is important at this point to note the sign convention regarding spin direction of particles in the beam. In the rubidium vapour, the valence electrons can be polarized in two directions. Using a right-handed coordinate system, the valence electrons possessing spin $\uparrow$ in the rubidium vapour are considered to have positive longitudinal polarization (also named *spin + at the source*). The Wien filter rotates the spin direction into the positive vertical direction at the cyclotron ($+y$-axis in the figures).

Physical rotation of the Wien filter assembly enables an additional reflection of the polarization of the beam—i.e. spin + at the source goes to $-y$ at the cyclotron entrance. This technique is used to explore systematic errors which may be correlated to the spin direction at the source.

The photodetachment laser

A 20 W argon laser, also known as the photo-neutralization laser, is used in the injection line for diagnostic purposes. A small fraction of the H^- ions

are neutralized by this process. The neutral atoms fail to be deflected by electrostatic benders into the cyclotron entrance, thus lowering the beam intensity.

Fast shutters, controlled by the data acquisition system, periodically block the laser light thus producing a controlled modulation of the beam intensity. The purpose of enhancing the modulation is to calibrate the parity apparatus to systematic fluctuations of the beam intensity. The photodetachment laser is used while the pumping lasers are blocked so that the beam is unpolarized.

The photodetachment laser is capable of producing correlated modulations of the beam intensity of between 0.1 and 0.2 % of the nominal beam intensity (as measured at the target area). Correlated intensity modulation (CIM) of this magnitude is approximately two orders of magnitude larger than intrinsic intensity modulation measured during regular operation of the parity apparatus.

2.1.2 Cyclotron

The TRIUMF cyclotron [23] laboratory is located on the campus of the University of British Columbia in Vancouver, BC. The TRIUMF cyclotron is a sector-focusing or AVF (azimuthally varying field) cyclotron capable of accelerating protons to 520 MeV kinetic energy for simultaneous extraction to several proton and meson beam lines. Figure 2.7 shows a picture of the then completed lower magnet assembly of the TRIUMF cyclotron. The photograph was taken in 1972 and is shown for purposes of illustration.

A cyclotron is a particle accelerator relying on perpendicular electric and magnetic fields to accelerate and confine an energetic ion beam in circular orbits whose radii increases with the particle energy. Typically an ion source, a large DC magnet, and a precisely tuned RF resonant cavity system are the main components of such a device. The electric field reversal is precisely synchronized to the frequency of the ions as they accelerate in the cyclotron

Figure 2.7: *The completion of the lower magnet assembly of the TRIUMF cyclotron. The six main bending magnets are shaped to account for relativistic mass increase as particles accelerate to hundreds of MeV. Photograph taken in 1972 [24].*

according to the following relation:

$$\frac{NeB}{m} = n\,\omega_C$$

where N is the number of unit electric charges on the ion, e is the fundamental unit of electric charge, B is the magnetic field strength of the cyclotron bending magnets, m is the mass of the ion, $n\,\omega_C$ is the electric field reversal frequency, n is an odd integer, and ω_C is defined as the cyclotron frequency of the ions in the magnetic field.

As the velocity of the ion is accelerated to relativistic values, however, the ion mass increases and either the electric fielad reversal frequency (cyclotron RF) must be decreased, or the B field increased in order to maintain synchronization. The main bending magnets in the TRIUMF cyclotron are custom shaped to account for relativistic mass increase at higher energy by slowly increasing the field strength at large radii thus enabling the cyclotron RF to

remain constant. The main advantage to the TRIUMF design is the ability to produce a constant current, or DC, source of relativistic ions for extraction. The minimum magnetic field in the TRIUMF cyclotron is 0.3 T, and the RF operates at the fifth harmonic which corresponds to 23 MHz.

Precise tuning of the cyclotron RF is required to minimize noise in the extracted beam parameters. Cyclotron RF instability can be caused by temperature fluctuations in the RF cavities and is correlated to enhanced position modulation of the beam at extraction. During normal parity data taking, the cyclotron RF is tuned to produce a constant radial density of beam particles near the region of extraction. This has been found to minimize the sensitivity of the parity apparatus to fluctuations in the cyclotron RF [21]. The optimum RF for stable beam conditions in the parity beam line varies by a few hundred Hz and is set by TRIUMF operations personnel in response to a beam current signal from the parity apparatus.

Stripping foil

A thin (2.5-5 mg/cm^2) carbon foil strips the electrons off nearly 100% of the H^- ions to produce a beam of protons. The magnetic force on the protons spirals the beam out of the cyclotron and into the beam line 4 magnetic transport system. The nominal 200 nA beam intensity extracted from the circulating beam is set by the size and position of the stripping foil in the cyclotron.

During each of the major data runs, a different stripping foil was used, and it was found that thinner foils decreased the amount of halo in the beam, with the disadvantage that they are less mechanically stable and need to be replaced more often. Beam halo consists of particles outside of the acceptance windows of the position monitors (IPMs) but within the entrance windows of the main detectors (TRICs). Figure 2.8 is a schematic of a typical stripping foil used during a data run in 1998.

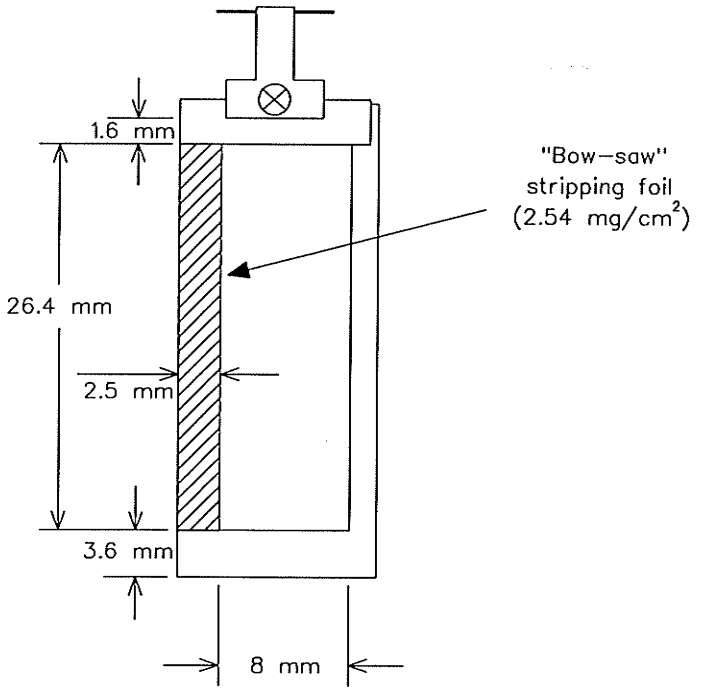

Figure 2.8: *Schematic of typical "Bow-saw" mounted stripping foil. The foil was installed at the commencement of the July 1998 parity data run.*

2.1.3 $4A/2$ beam line

Once the proton beam exits the cyclotron, it is transported to the parity detection apparatus by the $4A/2$ beam line. Two SD (solenoid-dipole) magnet pairs, and several sets of quadrupole magnets (the last of which is a quadrupole triplet) rotate the beam polarization into the longitudinal direction and focus the beam at the target. Positive beam line tune is defined as the combined magnet setting which rotates the beam polarization from the $+y$ direction in the cyclotron to the $+z$ direction in the beam line. Figure 2.9 shows the main components in the last section of the $4A/2$ beam line.

The final quadrupole triplet allows for small adjustments to be made to the beam focus near the target. The ferrite core steering magnets, coupled to a beam position feedback loop, make fast changes to the beam position to ensure the beam remains on the *polarization neutral axis* (see section 2.5.1).

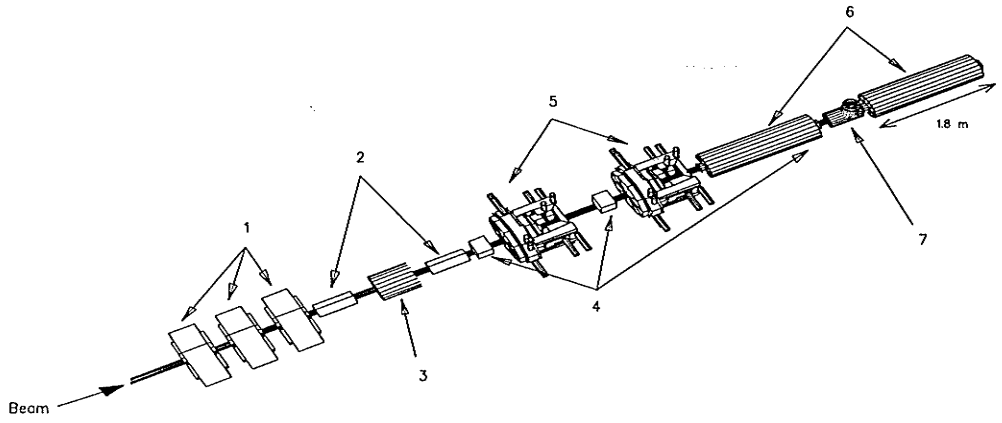

Figure 2.9: *The $4A/2$ beam line. The numbered components shown in the figure are: 1- quadrupole triplet, 2- ferrite core steering magnets (FCSMs), 3- RF cavity, 4- intensity profile monitors (IPMs), 5- polarization profile monitors, 6- transverse electric field ion chambers (TRICs), and 7- liquid hydrogen (LH_2) target.*

The RF cavity is used to perform measurements of the sensitivity of the parity apparatus to modulations of the beam energy. The intensity profile monitors (IPMs) read the intensity of the beam as a function of position in the transverse plane. Data from the IPMs are used to calculate the position and size of the beam. The polarization profile monitors (PPMs) measure the distribution of transverse polarization of the beam as a function of position in the transverse plane. The transverse electric field ionization chambers (TRICs) measure the beam intensity before and after the beam interacts with the target. The LH_2 target is liquid hydrogen maintained at 19 Kelvin and 1 Atm. Table 2.1 lists the z positions of the main components in the $4A/2$ beam line downstream of IPM1. Each of these elements in the beam line is briefly described in the sections that follow.

LH_2 target and TRICs

The LH_2 target contains unpolarized liquid hydrogen maintained at an operating temperature of $(19.3 \pm 0.2)\,°K$ and pressure of 1.13 Atm [2]. The target is

Component	Feb97 Position (mm)	Jul98 and May99 Position (mm)
IPM1	0	0
PPM1	474	431
IPM2	1837	1842
PPM2	2249	2195
TRIC1	4339	4242
IPM3	5241	5212
LH_2 target	5592	5556
TRIC2	6853	6780

Table 2.1: *The positions along the beam line (in z) of the main components of the parity apparatus used in the measurement of A_z. The measurement uncertainty of each position is ± 3 mm. The position of each component is respect to the center of its active volume. The equipment was repositioned and resurveyed prior to the Jul98 data run.*

cooled by an A20 refrigerator with 40 W of nominal cooling power, absorbing the radiant and conductive heat loads plus the 5.4 W of power deposited by the 200 nA, 221 MeV beam during normal data taking. The temperature of the liquid, during beam on, is monitored by a dedicated target feedback system which performs necessary adjustments to a heating element in the cryostat in order to keep the target temperature constant. Fluctuations in the target temperature are usually linked to variations in the beam intensity.

Figure 2.10 displays the target assembly. The length of the target along the z direction is 40 cm and has been optimized to produce the largest scattering probability while keeping multiple scattering within tolerable limits. Another important consideration in determining the optimal length of the target is the sensitivity of the parity apparatus to the systematic effect of beam energy fluctuations. Sensitivity to beam energy fluctuations increases with target length.

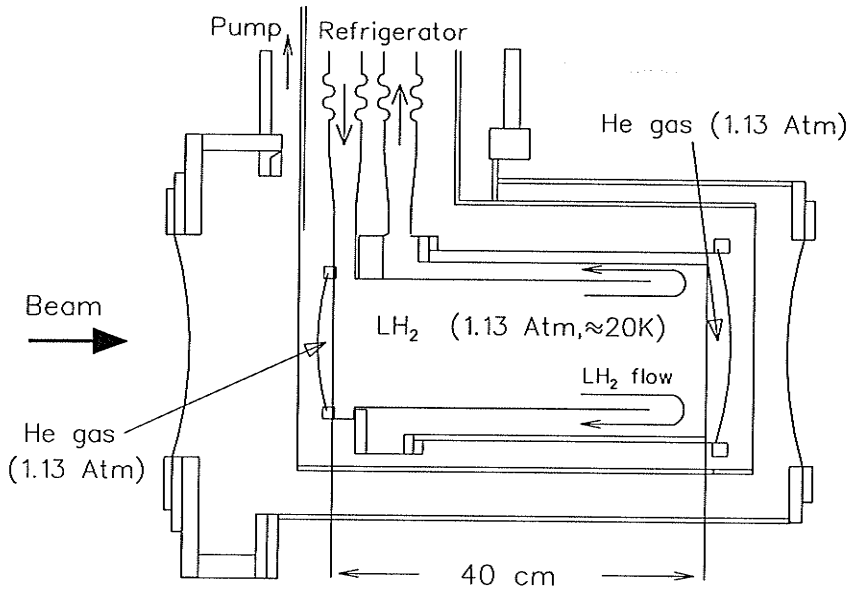

Figure 2.10: *The LH_2 target [2].*

The TRICs are the main detectors in this experiment. They are current mode parallel plate ionization detectors which measure the intensity of the beam upstream and downstream of the target. The active volume of the TRICs is 15 cm by 15 cm in x and y by 60 cm in z. The active volume is filled with hydrogen gas at a pressure of 150 Torr. Figure 2.11 shows the LH_2 target and TRICs.

The top electric plate in the ion chambers is at a potential of -8 kV with respect to the grounded bottom plate. When hydrogen gas is ionized by protons in the beam, the e^- produced are drawn to the bottom plate, and the resulting intensity signals from both ion chambers are fed to the data acquisition system.

The main asymmetry signal, proportional to A_z, is calculated by subtracting the difference in intensity read from both TRICs during the positive and negative helicity modes of the beam at the target. This measurement is performed by a precision analog subtractor module (see section 2.1.4).

The TRICs have been designed to minimize noise from attachment, recom-

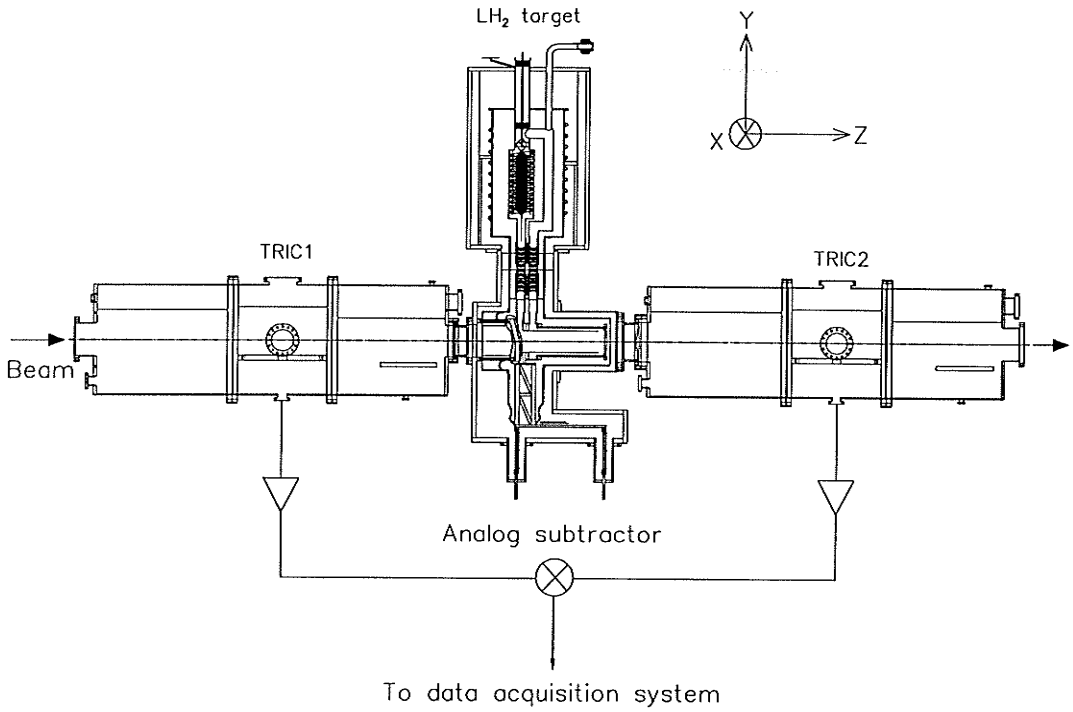

Figure 2.11: *LH_2 target and transverse electric field ionization chambers. The intensity of the beam is read by both TRICs and the TRIC signals are subtracted by an analog subtractor module. The subtracted signal is measured in both the positive and negative helicity states of the beam and the difference of these two measurements is proportional to the longitudinal analyzing power A_z.*

bination, spallation, delta ray, and space charge effects [25]. After construction of the TRICs, a mock data taking experiment was performed, which showed that the ionization chambers are intrinsically able to measure A_z to a statistical accuracy of $\pm 2 \times 10^{-8}$ after 300 hours of TRIC integration time, assuming a liquid hydrogen target of length 40 cm and a longitudinal beam polarization of 80%. In practice, the integration time required to achieve this level of statistical accuracy is larger by roughly a factor of two due to unstable beam conditions which lead to enhanced ion detector noise in current mode.

It is perhaps important to mention here that many of the systematic errors encountered in the measurement of the longitudinal analyzing power are the

result of spin dependent strong scattering by the target. A change in beam geometry can occur due to a change, for example, in beam size or position—which would then alter the path length of the beam passing through the TRIC2 active volume. Systematic errors of this type lead to a systematic asymmetry in the subtracted signal and a *false analyzing power*. False analyzing powers, systematic modulation of beam parameters, minimizing the helicity-correlated fluctuations in beam parameters, and corrections for systematic errors will be discussed throughout the remainder of this thesis, along with the final result of this analysis of the E497 parity experiment.

2.1.4 Beam property measurements

The following subsections briefly outline the instrumentation used to measure beam properties during regular data taking. These instruments include intensity profile monitors (IPMs) and polarization profile monitors (PPMs), the analog subtractor module, and the beam energy spectrometer (located in the injection line). The analog subtractor module measures the main asymmetry signal at the target. The IPMs and PPMs are located in the $4A/2$ beam line and are used simultaneously with measurements of A_z (online measurements). The beam energy spectrometer can not be integrated during online data taking and is instead used at interleaved data taking periods to infer the sensitivity of the parity apparatus to beam energy modulation.

Intensity Profile Monitors (IPMs)

The Intensity Profile Monitors, IPMs [26], are current mode beam position sensors. Each monitor has 31 nickel strips—forming an IPM readout *harp*—in both the vertical and horizontal directions. The nickel strips measure the intensity of the beam (at fixed position) by way of secondary electron emission (SEM) in vacuum. Aluminum collector foils—at a bias of $+100V$—sandwich

the harp packs and collect the secondary electrons.

The total thickness of nickel and aluminum in each detector is between 6 and 20 μm nickel and between 24 and 40 μm aluminum. The actual thickness of material depends on the detector (IPM1, IPM2, or IPM3) and has been optimized to produce the least possible amount of multiple scattering in the beam. Figure 2.12 is a schematic of a typical IPM foil pack.

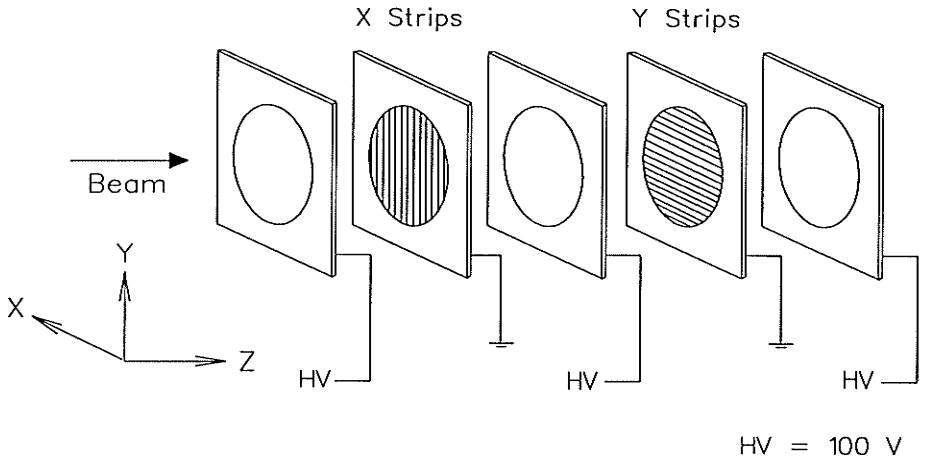

Figure 2.12: *Schematic of an IPM foil pack [21]. The foil strips are* 3 μm *Ni. Each IPM harp contains 31 strips spaced apart by 2 mm. The harp packs are sandwiched between collector foils which collect the secondary electron emission at a bias of* $+100V$.

The approximate gain of each strip is 4-5 electrons per 100 beam protons. The gain is sufficient to provide a measurement with approximately 10^{-4} relative counting error per strip over an integration time of $(\frac{1}{60})\ s$ at $200\ nA$ intensity. Thus, the statistical resolution in position during the TRIC/IPM integration gate is roughly 500 nm assuming the standard deviation of the particle distribution in the beam envelope is 5 mm. In practice, however, beam instabilities plus pickup from mechanical vibrations of the foil assemblies dominate the uncertainty in the determination of the beam centroid position, and the resolution is usually lower by roughly an order of magnitude than the ideal case.

Each strip signal is amplified by a dedicated current to voltage preamplifier. The voltage signals are digitized using (V:F) converters and are fed to LeCroy 4434 32-channel scalers. Figure 2.13 displays the IPM strip preamp circuitry. The parity data acquisition system (DAQ) logs the output of all six IPM harps onto magnetic tape and processes the data for online data analysis.

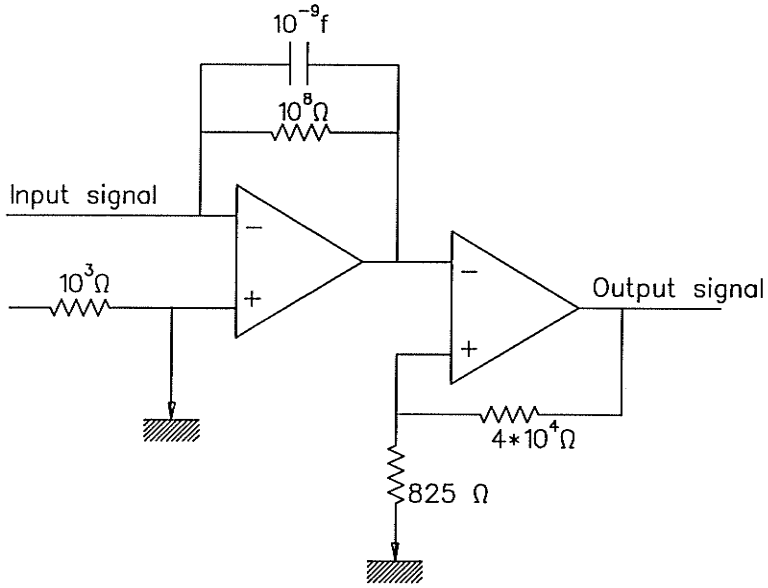

Figure 2.13: *IPM harp foil preamp circuitry [21]. BurrBrown OPA 128 LM amplifier current-to-voltage chips are used on each strip.*

The IPM harps are calibrated during regular data taking by measuring the pedestal profiles [27]. Pedestal measurements are performed roughly every three days and with no beam. The pedestals show random signal variation arising due to differences in strip circuitry as well as differences in the idling rates of the V:F converters. The relative gain on each strip was measured by steering the beam a known distance in the horizontal and vertical directions and observing the response of the strips. Before analyzing the intensity profiles, the DAQ subtracts the most recent pedestal measurement from the harp signals and multiplies the real signal by the relative gain on each strip.

Data analysis software evaluates the vertical and horizontal beam intensity

profiles and determines the nominal beam size and position relative to the fixed center of the strips. The *size* of the beam is defined as the standard deviation of the distribution of particles in the beam envelope.

Polarization profile monitors (PPMs)

The polarization profile monitors, PPMs [28], measure the distribution of transverse polarization in the beam as a function of position in the vertical and horizontal directions. Two polarization profile monitors exist in the $4A/2$ beam line; both are upstream of the target. Figure 2.14 is a schematic of one of the PPMs designed for the parity experiment. Both PPMs are constructed in the same fashion. The figure displays the PPM blade housing along with the left branch of the polarimeter, which is used in coincidence with the right branch, to measure vertical polarization components in the beam.

Each PPM has two target wheels, each wheel containing two scanning blades. The four scanning blades scan the beam twice in the vertical and twice in the horizontal direction during each full rotation of a PPM. The scanning sequence of the two PPMs is set so that the beam is scanned by all 8 blades, at equal intervals, during each full rotation of both PPMs.

The scanning blades of the polarization monitors are made of CH_2. CH_2 is used because it has a large transverse analyzing power in $\vec{p}p$ scattering (0.3 at 17.5°). The devices which detect the scattered protons are fast plastic scintillators coupled via light guides to RCA 8575 photomultipier tubes and placed in a "4-branch polarimeter" configuration.

Each PPM has four coincidence branches which detect a counting rate asymmetry in the left-right and down-up directions. The left-right branches measure transverse polarization in the vertical (y-axis direction) while the down-up branches measure transverse polarization in the horizontal (x-axis direction). Figure 2.15 is a schematic of the left-right coincidence branches. If

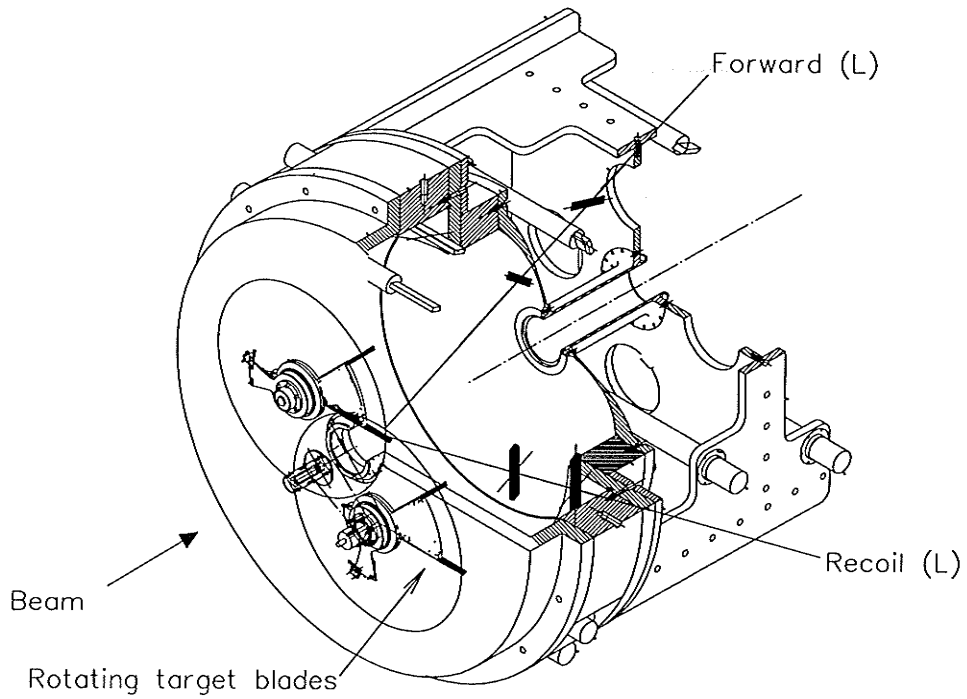

Figure 2.14: *Schematic of a PPM blade housing and coincidence detector arrangement. The detectors shown are arranged in order to measure the distribution of protons in the incident beam which contain spin in the y direction. Each PPM has three additional detection arrangements in order to measure the distribution of transverse polarization components, $P_y(x)$ and $P_x(y)$, in the beam.*

n_L denotes the number of left branch coincidence events and n_R denotes the number of right branch coincidence events during the same time interval then

$$A_t P_y = \frac{n_L - n_R}{n_L + n_R} \tag{2.6}$$

where A_t is the transverse analyzing power of the CH_2 target and P_y is the polarization component of the beam along the y-direction. A similar expression holds for the $P_x(y)$ component. Both components, $P_x(y)$ and $P_y(x)$, are measured during online data taking and external calibration studies, so that systematic error corrections to the measured A_z can be made for the effect of transverse moments of polarization. This is important, as it will be seen in

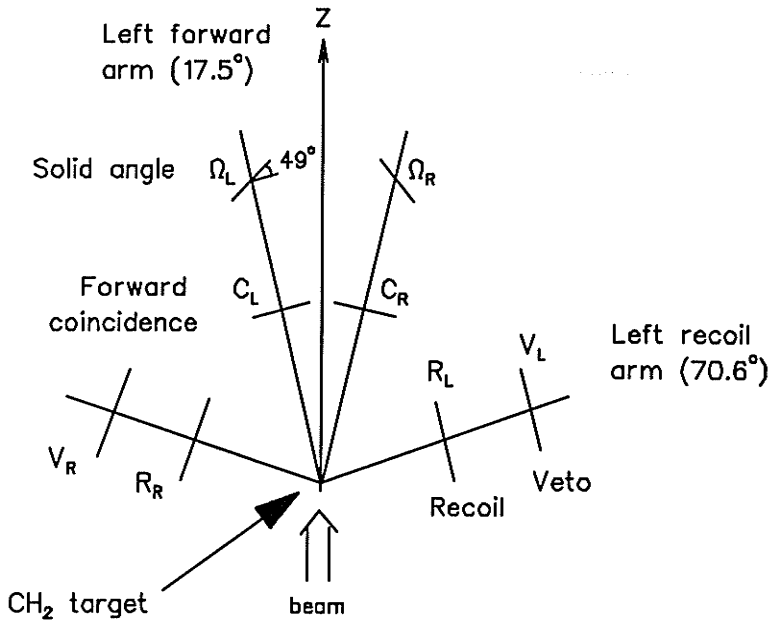

Figure 2.15: *Schematic of the left-right coincidence branches. A proton in the beam possessing spin in the $+y$ direction will elastically scatter with a proton in the CH_2 target triggering a coincidence in the left branch. Scattering events in the left branch are characterized by the four-fold coincidence $(C_L \cdot \Omega_L) \cdot (R_L \cdot \bar{V}_L)$. Scattering events in the right branch are characterized by the four-fold coincidence $(C_R \cdot \Omega_R) \cdot (R_R \cdot \bar{V}_R)$. The left-right counting asymmetry is proportional to the vertical beam polarization.*

chapter 3 that an important contribution to systematic error in this experiment is for these effects.

In order to differentiate between elastically and inelastically scattered protons, recoil detectors are placed at 88.1° relative to the forward coincidence (in the scattering plane). The recoil scintillators are 6.35 *mm* thick detectors which, together with 1.6 *mm* thick aluminum shields behind the detectors, absorb elastically scattered protons (having a mean energy of less than 22 MeV). Higher energy protons from inelastic collisions in the carbon nuclei will give a signal in the veto detector. Thus, a $(\mathrm{R} \cdot \bar{V})$ event will indicate the presence of a proton possessing momentum of no more than 22 MeV and travelling along

the recoil direction.

A solid angle scintillator is placed downstream of the forward coincidence scintillator and is rotated 49° to the normal of the forward coincidence direction. The rotation accounts for the variation in differential scattering cross-section and solid angle with blade position and allows for a uniform response of the PPM over approximately 6 mm of beam width [2].

The PPM blade position is read by a 2500 line incremental tick shaft encoder rotating at 5 Hz, each tick corresponding to 80 μs. Encoder advancement is governed by a PC-based system capable of locking the blade rotation period to within one tick per revolution. Because the spin state sequence requires as many different spin states as there are scanning blades (8 in all, see section 2.2.1), two complete cycles of the PPMs are required to determine the transverse polarization. This is required to ensure each of the eight blades sample both helicity states during a measurement of the transverse polarization.

The coincidence counts are binned in LeCroy 3521A multichannel scalers (MCS). The MCS scalers contain 80 channels; each channel is reserved for the scattering asymmetry of transversely polarized protons at a particular position in the beam envelope. The clock pulses generated from the shaft encoders also send channel advance signals to the multichannel scalers. Thus, each of the 80 MCS scaler channels corresponds to a distinct blade position in the beam envelope.

The scalers are cleared at the end of the PPM rotation and the data are sent to the acquisition computer which performs online profiling of the transverse polarization characteristics of the beam. The data from the 80 channels are also logged onto magnetic tape for further analysis offline.

Analog subtractor

The primary asymmetry signal measured by the ion chambers is processed by

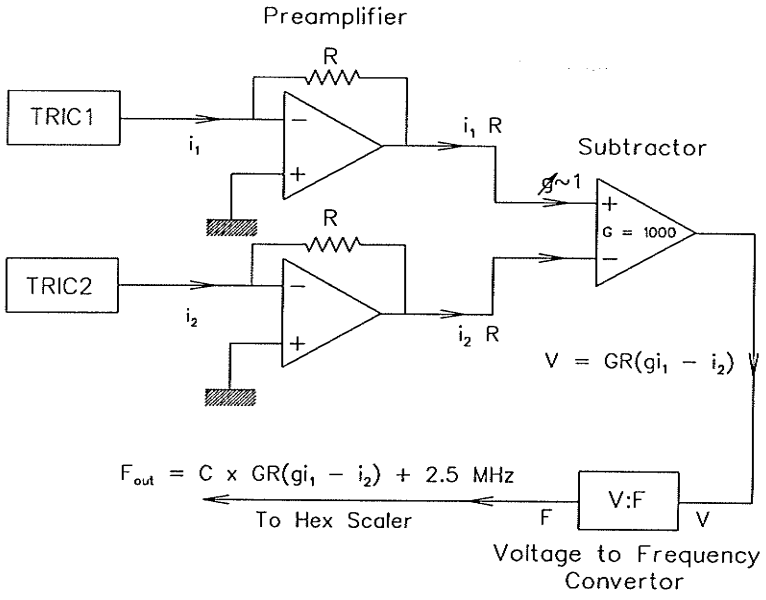

Figure 2.16: *Schematic of the precision preamplifier and subtractor box [21]. The TRIC current is converted to a voltage by the preamplifiers. The voltages from both TRICs are fed to the subtractor module where the difference signal is amplified by a factor of* $G = 1000$.

a custom built preamplifier and analog subtractor box [2]. Figure 2.16 shows a schematic of the analog subtractor module.

The current read from the chambers is converted to a voltage by a Burr Brown OPA 111 BM preamplifier. The conversion factor is $13.6 \times 10^{-5} \frac{V}{nA}$. Both TRIC signals are input to the analog subtractor module where the subtracted signal is amplified by a factor of 10^3. The subtractor box output is roughly proportional to the difference in beam current passing through TRIC1 and TRIC2. It is not quite proportional due to a variable fine gain adjustment on the TRIC1 preamplifier output. The gain is very close to one and allows the subtraction to be fine tuned for best common mode rejection. The subtractor box output is fed to a precision (V:F) module with conversion factor $0.5 \frac{MHz}{V}$.

The V:F output, denoted F_{out}, is given by

$$F_{out} = C \times GR(gi_1 - i_2) + 2.5MHz, \tag{2.7}$$

where g is the variable fine gain on the TRIC1 preamp output, R is the preamp conversion factor, G is the subtractor gain, C is the (V:F) conversion factor, and $2.5MHz$ is the built-in idling rate of the V:F. The longitudinal analyzing power A_z is proportional to the ratio of the difference of F_{out} in the two helicity states to the average beam current. In symbols

$$A_z \equiv \Phi \frac{F_{out}^{+} - F_{out}^{-}}{i_1} = \Phi \frac{\Delta F_{out}}{i_1}, \tag{2.8}$$

where Φ is a scale factor equal to 1.84 nA/MHz for the parity electronics.

During regular parity data-taking, small adjustments of the fine gain, g (the DC level), can be made to minimize systematic error caused by correlated intensity modulation. The minimization procedure is called a "box balance" and is performed every 1-3 days during regular data taking. Section 2.6.4 describes the "box balance" procedure.

Beam energy modulation spectrometer

The beam energy modulation spectrometer is used during regular data taking to estimate the intrinsic beam energy and position modulation produced coherently at the ion source. It can also be used to introduce a coherent modulation of the beam energy for diagnostic purposes (see section 2.6.3). Figure 2.17 shows a schematic of the instrumentation, installed at OPPIS in 1997, which is used to perform measurements of the coherent energy modulation.

The 3 keV $\vec{H}^-$ beam is steered using electrostatic deflection plates, and the coherent beam position modulation is measured at a movable 16 channel profile monitor. The polarity of the steering plates can be reversed and the position monitor moved in order for the position modulation to be measured on both sides of the beam line. This allows separation of coherent beam position and energy modulation.

The coherent beam position modulations, Δx_L and Δx_R shown in the

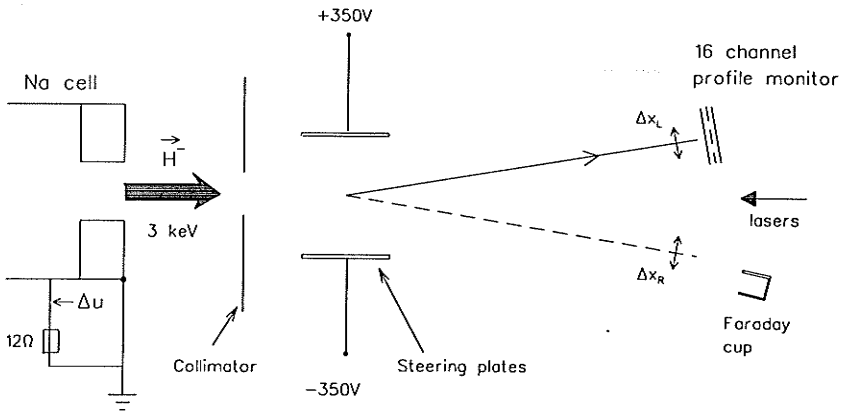

Figure 2.17: *Schematic of the beam energy modulation spectrometer [2]. The apparatus was installed in the injection line in order to measure coherent beam position and energy modulation produced at OPPIS.*

figure, are related to coherent beam position and energy modulations in the injection line by

$$\Delta x_L = \Delta x_{OPPIS} + a_L \Delta E$$

$$and$$

$$\Delta x_R = \Delta x_{OPPIS} - a_R \Delta E \quad , \tag{2.9}$$

where Δx_{OPPIS} and ΔE are the coherent beam position and energy modulation, respectively, produced at the source. The calibration factors a_L and a_R are determined by adding a square wave voltage bias to the sodium ionizer cell and measuring Δx_L and Δx_R. The bias, of amplitude $\pm 50mV$, is applied in phase with the spin flip pattern with the pumping lasers blocked.

2.2 Data acquisition

The DAQ [29] is a complex network of system modules and computer processors. The DAQ is responsible for sending spin request information to OPPIS; controlling the TRIC, IPM, and PPM data collection; and processing the data

stream. Processing the data stream includes writing the parity data buffer to magnetic tape (DLOG) as well as providing beam diagnostic information during regular parity data taking. Figure 2.18 is block diagram of the DAQ.

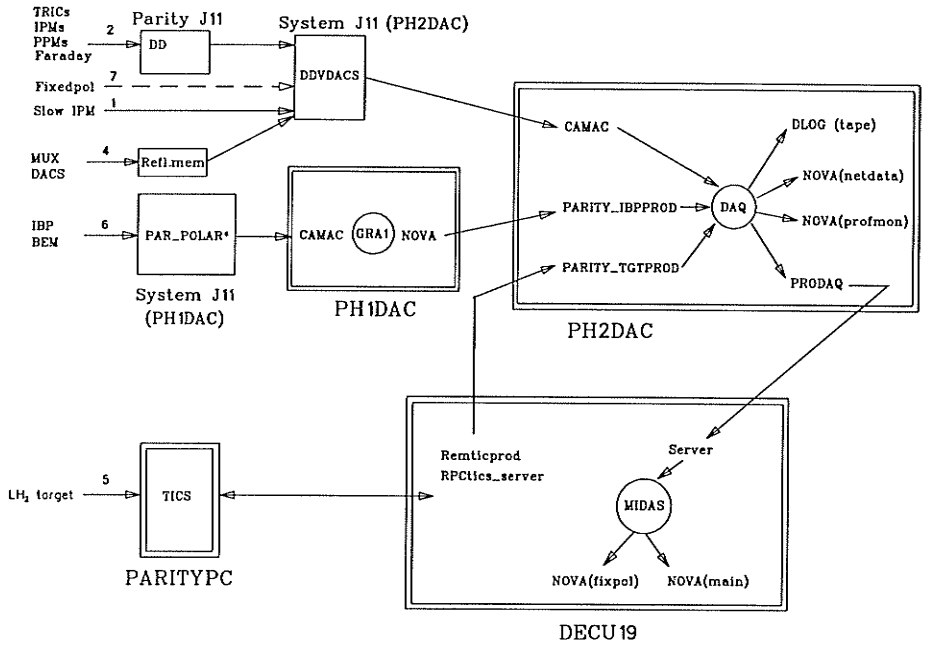

Figure 2.18: *Block diagram of the TRIUMF E497 data acquisition system [21].*

Data stream processing is performed by the histogramming software package NOVA [30]. NOVA subroutines evaluate the 31 channel harp signals from the IPMs and the 80 channel (MCS) scaler output from the PPMs (see section 2.1.4). NOVA subroutines calculate beam parameter profiles such as average and helicity-correlated beam position, size, and transverse moments of polarization. The beam profiles are then averaged over 16 consecutive spin states of the beam (two complete PPM rotation cycles). Helicity-correlated variables are calculated by subtracting the averages of beam variables for consecutive eight spin state "events" (a sixteen blade event, 2-event, or *event pair*). Other important functions performed by the DAQ and NOVA include determining the average and helicity-correlated beam intensity read from the TRICs, tracking LH_2 target parameters (such as target temperature), the average beam energy, as well as determining the polarization of the rubidium cell.

2.2.1 Timing

One parity substate samples the beam using one of the 8 PPM blades. The substate is 25 ms in duration, and two-thirds of this time (exactly 1 period of the AC line frequency, 16.667 ms) is dedicated to TRIC and IPM integration where the main parity asymmetry signal and beam position information is read. The remaining time of the substate is dedicated to stabilization of the polarization in the source, PPM integration, and "dead time". The dead time is a 1.1 ms delay at the end of the substate which allows for fluctuation of the PPM rotation rate. An additional 0.8 ms delay at the beginning of the substate provides time for the source polarization to stabilize. During each substate, the beam is sampled with either positive or negative helicity and the particular spin state of the source during the substate is controlled by the DAQ. The spin request is sent to the source by the DAQ at the beginning of the 0.8 ms stabilization delay. Figure 2.19 is a schematic of the substate integration gates.

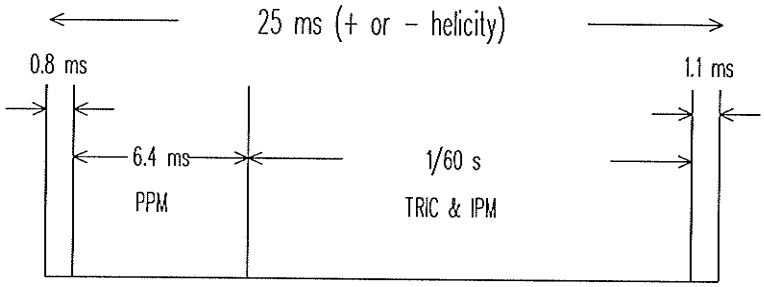

Figure 2.19: *One 25 ms substate [2]. The main parity asymmetry signal is measured during the TRIC/IPM integration gate. The length of the TRIC/IPM integration is* $(\frac{1}{60})$ *s and is designed to eliminate noise at 60 Hz.*

Events are grouped into 8 substate cycles, where 1 cycle samples the beam with all 8 PPM blades and, therefore, the length of 1 cycle is 200 ms. The spin sequence, or spin state pattern, for the 8 blade cycle is one of the following two sequences: $+--+-++-$ or $-++-+--+$. As is evident by the pattern,

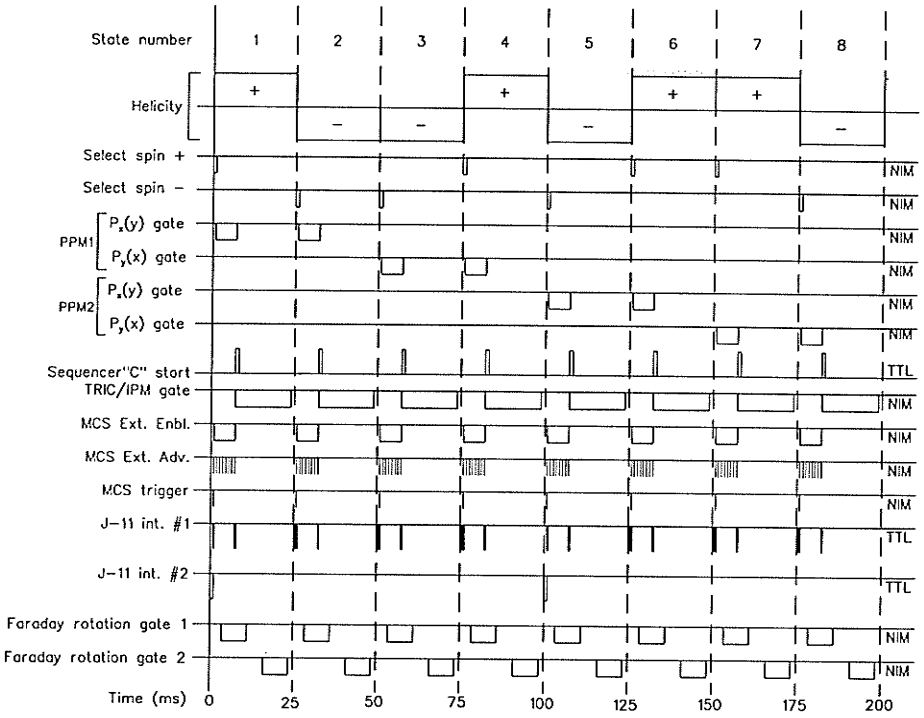

Figure 2.20: *A chart indicating the trigger timing of gate signals during an eight blade cycle [21].*

linear and quadratic terms in the beam parameter drift (over the time period of the cycle) are removed.

The eight blade event sequence samples the subtractor box signal over a period of 200 ms. The spin flip pattern is particularly sensitive to noise at 5 and 15 Hz, but not to the 60 Hz line frequency which considerably reduces statistical uncertainty in measured A_z.

The 8 blade cycles, or *eight blade events*, form part of a larger structure called a supercycle. A supercycle contains eight consecutive cycles. The spin state sequence of the supercycle is similar to the eight blade event in that the first event in each cycle follows one of the eight state sequences above. The spin state of the first event of a supercycle is chosen at random by the DAQ. Figure 2.20 shows the timing of integration gate signals and spin request signals for the eight blade cycle.

During regular data taking, the DAQ controls how much data is acquired in spin-on mode versus spin-off mode via an adjustable parameter which is set prior to the beginning of a run. The parameter is usually set at four spin-on supercycles followed by one spin-off supercycle. Every second spin-off supercycle contains enhanced CIM produced by the photodetachment laser.

2.2.2 Data storage

DLOG writes all data that are handled by the DAQ to magnetic tape. A magnetic tape, which has a storage capacity of 2.0 GBytes, can store approximately twenty average one-hour runs. Each average one-hour run consists of approximately 140,000 parity substates.

The raw parity data event buffer includes raw data from the MCS scalers, IPM readout harps, TRICs, MUX/DAC readouts, Faraday rotation measurements, and all other scalers processed by the DAQ. The tapes are read by an offline PC and the buffer is reduced by averaging data over sixteen blade *event pairs*.

Tape reduction

Offline data reduction is performed by the histogramming package NOVA. NOVA determines the ion source spin state of an event in the buffer and which PPM blade scanned the beam. The program then calculates helicity-averaged and helicity-correlated quantities of beam parameters. The beam parameters are used to calculate the sensitivity of the parity apparatus to modulations of beam parameters and to estimate systematic errors during the measurement of A_z.

The output of NOVA contains three data types: spin-on event pairs (normal parity data, 80% of the data stream), spin-off event pairs (10% of the data

stream), and CIM event pairs (unpolarized beam with enhanced CIM—10% of the data stream). Data from each event pair are written in binary real numbers to a permanent storage disk in the same sequence the data are originally measured during data taking. The NOVA reduction process compresses the amount of data by roughly a factor of 16. NOVA then writes the compressed data to magnetic disk.

The amount of compressed data is further reduced by applying data quality cuts on beam parameters. The data reduction procedure is presented in section 3.3.

2.3 Systematic errors

There are two classifications of systematic errors: helicity-correlated beam parameter modulations at OPPIS and helicity-correlated beam parameter modulations in beam line $4A/2$. Ultimately, all systematic errors arise from coherent instabilities at the ion source, however, an amplification of the modulations can occur due to the cyclotron and beam line components. For this reason, systematic errors are grouped into the two categories above. The final sections in this chapter discuss the definition, calibration, and minimization of the two classes of experimental systematic error.

In general, a systematic error (also referred to as a false analyzing power) is defined as

$$\Delta A_z = \alpha \frac{\zeta^+ - \zeta^-}{2} = \alpha \Delta\zeta \tag{2.10}$$

where α is the sensitivity of the parity apparatus to helicity-correlated beam parameter $\Delta\zeta$. Systematic error corrections are performed on all beam parameters known or expected to contribute a significant (non-zero) false analyzing power during the measurement of A_z.

The measurement of A_z is not sensitive to average (or DC) beam parameters, but by tracking the average beam parameters, the systematic effect of helicity-correlated beam parameter modulations can be minimized. For example, in the case of transverse moments of polarization, the sensitivity of the parity apparatus to extrinsic first moments of polarization can be altogether eliminated when the beam travels along its "neutral axis". In general, the average beam parameters corresponding to equation 2.10 are given by

$$\zeta = \frac{\zeta^+ + \zeta^-}{2} . \tag{2.11}$$

2.4 Intrinsic modulations at OPPIS

2.4.1 Intensity modulation

A systematic polarization mismatch between the spin $\uparrow$ and spin $\downarrow$ valence electron states produced in the rubidium vapour cell will lead to a systematic modulation of beam intensity. The mismatch can occur if one or both of the pumping lasers are not tuned to their optimal frequency, or if the pumping lasers irradiate the vapour cell with a difference in power. These differences will affect the intensity of the $\vec{H}^0$ beam entering the sodium ionization cell as a function of beam helicity. Thus, the beam intensity will modulate coherently with the spin flip pattern at the target and a false asymmetry will occur if the detectors and readout electronics have a non-linear response.

Correlated intensity modulation (CIM) is measured relative to the average beam intensity at TRIC1; thus,

$$CIM \equiv \frac{\Delta I}{I} = \left(\frac{i_1^+ - i_1^-}{i_1^+ + i_1^-} \right) , \tag{2.12}$$

where i_1^+ is the beam intensity (measured by TRIC1) in + helicity.

Typical sensitivities of the parity apparatus to CIM—on a run by run basis—are of the order of (100-200) $\times 10^{-7}/\%$. Therefore, relative beam

intensity modulations must be maintained at the 10^{-5} level or below in order to maintain the false analyzing power arising from CIM at the 10^{-8} level.

Via the photodetachment laser, enhanced CIM can be created in the injection line and used to track the sensitivity online. As previously discussed, the enhanced modulation data is taken during a separate data taking phase of the data acquisition process and is stored on magnetic tape for analysis offline. If a large sensitivity is calculated, a small adjustment to the DC level of the subtractor box can be made to reduce the sensitivity of the apparatus to $\frac{\Delta I}{I}$. Adjustments to the subtractor box DC level are usually made every three hours during regular parity data taking.

2.4.2 Energy modulation

Coherent energy modulation of the beam due to helicity-correlated modulation of the beam energy (at OPPIS) is defined as

$$\Delta E = \frac{E^+ - E^-}{2} . \tag{2.13}$$

A systematic difference in energy between the two spin states produced at OPPIS will lead to a false analyzing power. The error arises due to the nonlinearity of the TRIC response as a function of energy. The 27 MeV beam energy loss in the target changes the slope of the TRIC response curve to a modulation of the beam energy. The result is a false analyzing power in the measurement of A_z. Figure 2.21 shows a schematic of the stopping power of hydrogen gas as a function of beam energy, illustrating how the sensitivity to coherent beam energy modulation arises. It will be seen in the next chapter that ΔE at OPPIS is on the order of meV and that coherent energy modulation of this magnitude can lead to a significant false asymmetry in the measured A_z.

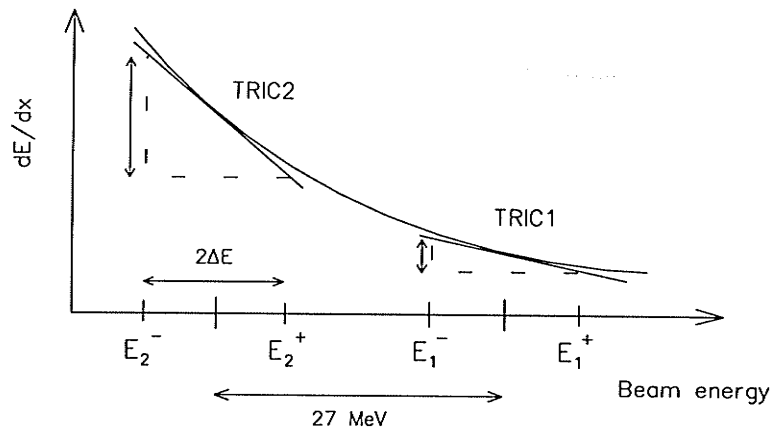

Figure 2.21: *A schematic of the stopping power of hydrogen as a function of energy [2].*

2.4.3 Position modulation

The systematic effect of beam position modulation at the ion source has been measured to be an order of magnitude smaller than the effect due to beam energy modulation. Position modulation originating at the source is also expected to be highly correlated to beam position and size modulation in the $4A/2$ beam line. The latter's effects are well controlled in this experiment and the associated false asymmetry will be seen to be consistent with zero at the 10^{-8} level. Therefore, no separate correction or uncertainty estimates are made for the systematic effect of beam position modulation originating at the ion source.

2.5 Modulations of beam parameters in $4A/2$

2.5.1 Transverse moments of polarization

The differential scattering cross section for a target with non-zero transverse analyzing power $A_t(\theta)$ is

$$\frac{d\sigma}{d\Omega}(\theta,\phi) = \frac{d\sigma}{d\Omega_0}(\theta)\left\{1 + P_t A_t(\theta)\cos\phi + P_z A_z(\theta)\right\}, \qquad (2.14)$$

where $\cos\theta = \hat{k}_{in} \cdot \hat{k}_{out}$, $\cos\phi = \hat{P}_t \cdot \left(\hat{k}_{in} \times \hat{k}_{out}\right)$, $\hat{k}_{in}$ is the incoming direction unit vector, and $\hat{k}_{out}$ is the scattered direction unit vector. As will become evident in section 3.5, the largest systematic error correction to the measurement of A_z is for the systematic effect of transverse polarization.

False analyzing power is generated when the beam contains a net transverse polarization and does not occupy the polarization neutral axis. When this occurs, a false analyzing power is generated when protons are scattered out of the TRIC2 active volume as a function of helicity. Figure 2.22 is a schematic of how the trajactory of a transversely polarized beam can change as a function of beam helicity. The effect has been greatly exaggerated for purposes of illustration. The solid arrows indicate the preferred directions of scattering, which lead to an asymmetry in the TRIC2 detector signal. In general, the distribution of polarization in the transverse plane $\vec{P}_t$ is given by

$$\vec{P}_t \equiv \vec{P}_t(x,y) = P_x(x,y)\hat{i} + P_y(x,y)\hat{j} \tag{2.15}$$

where $\hat{i}$ and $\hat{j}$ are the unit vectors in the x and y directions, respectively.

Polarization neutral axis

The polarization neutral axis is an axis through the target and TRIC system which, no matter how large the component of transverse polarization, leaves the resulting subtracted signal invariant to a helicity-correlated reflection of the transverse polarization. This is achieved when the average path length of scattered particles through TRIC2 does not change during helicity reversal, even if the path direction of the scattered particles do change. The neutral axis, therefore, is a strictly geometrical characteristic of the parity apparatus.

The total first moment of polarization of the beam, $\mathcal{F}_t^{x,y}$, is calculated by integrating the polarization distribution over the horizontal and vertical directions. Thus, at a given time and for a given z position (along the $4A/2$

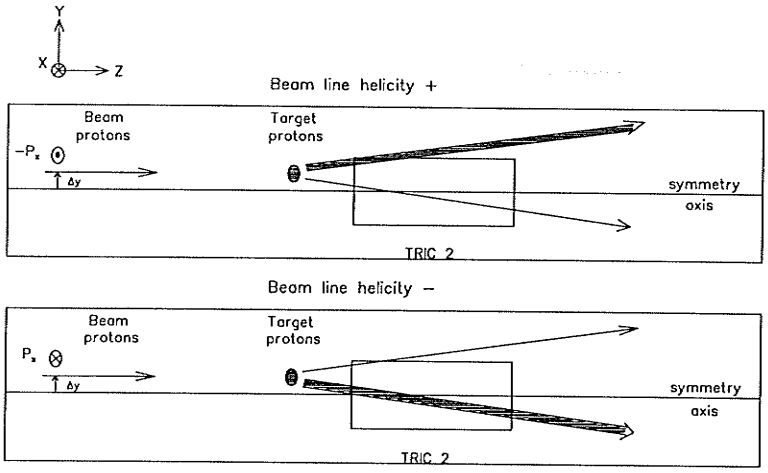

Figure 2.22: *Schematic of the effect of transverse polarization and the polarization neutral axis [2]. In the bottom picture, the net transverse polarization of the beam has been rotated π radians as a result of the spin reversal at the source. The net systematic error is proportional to the distance of the beam from the symmetry axis. The resulting measurement of the analog subtractor box will contain a false asymmetry.*

beam line)

$$\mathcal{F}_t^x \equiv \int x(P_x + P_y)N(x,y)dx$$

and

$$\mathcal{F}_t^y \equiv \int y(P_x + P_y)N(x,y)dy$$

where $N(x,y)$ is the normalized intensity distribution of particles in the transverse plane. The terms containing yP_y and xP_x are expected to contribute a false asymmetry an order of magnitude less than the terms containing xP_y and yP_x, respectively, and are ignored [2]. Thus, the total first moment in the horizontal direction can be approximated to:

$$\langle xP_y \rangle_t = \int xP_y(x)N(x)\,dx = \int x\left\{P_y^0 + P_y^1(x) + P_y^2(x^2) + \cdots\right\}N(x)\,dx\,,$$

where $N(x) = \int dyN(x,y)$. Therefore, to first order and with an analogous

treatment in the vertical direction

$$\langle xP_y\rangle_t = \int x\left\{P_y^0 + P_y^1(x)\right\}N(x)\,dx = \langle x\rangle\langle P_y\rangle + \langle xP_y\rangle,$$
$$\langle yP_x\rangle_t = \int y\left\{P_x^0 + P_x^1(y)\right\}N(y)\,dy = \langle y\rangle\langle P_x\rangle + \langle yP_x\rangle. \qquad (2.16)$$

In equation 2.16, the right-most terms are defined as the intrinsic first moments of polarization of the beam polarization distribution in the transverse directions. The terms preceeding the intrinsic moments are the extrinsic first moments of polarization. The extrinsic first moments are simply the product of the average values of the beam position, relative to the neutral axis, and the average values of the beam polarization. Because the intrinsic moments depend on the distribution of polarization in the transverse plane, they are very difficult to control in the beam line. In section 2.6.2, a beam optics technique is presented which minimizes the systematic effect of the intrinsic moments.

As for the extrinsic moments, they can be minimized in two ways: tune the beam line magnets to reduce transverse polarization, and conduct the experiment so that the parity beam travels along the polarization neutral axis. The next section will calculate the sensitivity of the parity apparatus to transverse polarization and describe a method to determine the neutral axis.

Sensitivity to first moments of polarization

Assuming that the total first moment of polarization varies linearly with z, the false analyzing power measured at the subtractor box due to first moments measured at the PPMs may be given by [2]

$$\Delta A_z = a_1\langle yP_x\rangle_t^1 + b_1\langle xP_y\rangle_t^1 + a_2\langle yP_x\rangle_t^2 + b_2\langle xP_y\rangle_t^2 \qquad (2.17)$$

where $\langle yP_x\rangle_t^{1,2}$ are the total first moments measured at PPM1 and PPM2. Using equation 2.16, the total first moment at PPM1 is

$$\langle yP_x\rangle_t^1 = \left(\langle y_1\rangle - y_1^{na}\right)\langle P_x\rangle + \langle yP_x\rangle_1 \qquad (2.18)$$

where $\langle y_1 \rangle$ is the average beam position at PPM1, y_1^{na} is the neutral axis position in the y-direction at PPM1, $\langle P_x \rangle$ is the average transverse polarization in the x-direction (measured by both polarimeters), and $\langle yP_x \rangle_1$ is the intrinsic first moment measured at PPM1.

Thus, with similar expressions for x and xP_y, the total false analyzing power due to transverse moments of polarization can be represented by

$$\begin{aligned} \Delta A_z &= \langle P_x \rangle (a_1 \langle y_1 \rangle + a_2 \langle y_2 \rangle + a_3) \\ &+ \langle P_y \rangle (b_1 \langle x_1 \rangle + b_2 \langle x_2 \rangle + b_3) \\ &+ a_1 \langle yP_x \rangle_1 + a_2 \langle yP_x \rangle_2 \\ &+ b_1 \langle xP_y \rangle_1 + b_2 \langle xP_y \rangle_2 \end{aligned} \tag{2.19}$$

where a_3 and b_3 are equal to $(-a_1 y_1^{na} - a_2 y_2^{na})$ and $(-b_1 x_1^{na} - b_2 x_2^{na})$, respectively.

Periodically during regular parity data taking, *neutral axis scans* are performed. Neutral axis scans are calibration studies in which the transverse polarization of the beam is enhanced and the response of the subtractor box is mapped over a relatively large spatial extent of the transverse plane. The measured false analyzing power, usually two to three orders of magnitude larger than background during normal parity data taking, is regressed against equation 2.19 and the sensitivities $\{a_1, ..., b_3\}$ are determined. The scans are performed separately, that is, P_y is scanned across x and P_x is scanned across y. The neutral axis is chosen so that $y_1^{na} = x_1^{na} = 0$ (as measured at IPM1). The neutral axis positions at IPM2 are found by projecting the results of the calibration to the z position of IPM2 along the beam line.

There exists a *magic point* along the parity $4A/2$ beam line. If the intrinsic first moment goes through zero at this point, the false A_z will be zero. At this point, the sensitivity of the apparatus is not dependent on the path of the particles in the beam envelope nor the angle of the beam with respect to the z-axis.

To find the magic point, examine equation 2.19 assuming that the experiment is being conducted with the beam on its neutral axis. Then the sensitivity of the apparatus to transverse polarization is only due to intrinsic first moments, and the false asymmetry is given by

$$\begin{aligned} \Delta A_z &= a_1\langle yP_x\rangle_1 + a_2\langle yP_x\rangle_2 \\ &+ b_1\langle xP_y\rangle_1 + b_2\langle xP_y\rangle_2 \,. \end{aligned} \tag{2.20}$$

It becomes immediately apparent that if

$$\frac{\langle yP_x\rangle_1}{\langle yP_x\rangle_2} = -\frac{a_2}{a_1} \quad and \quad \frac{\langle xP_y\rangle_1}{\langle xP_y\rangle_2} = -\frac{b_2}{b_1}$$

then no false asymmetry due to intrinsic first moments is expected. Assuming the ratios of intrinsic first moments satisfy these conditions, the intrinsic first moment will be zero at the magic point.

The magic point is found by extrapolating along the z axis assuming that the first moments vary linearly with z:

$$z_y^{mp} = \frac{a_1 z_{PPM1} + a_2 z_{PPM2}}{a_1 + a_2} \tag{2.21}$$

and

$$z_x^{mp} = \frac{b_1 z_{PPM1} + b_2 z_{PPM2}}{b_1 + b_2} \tag{2.22}$$

where z_y^{mp} and z_x^{mp} are the *magic points* for intrinsic moments $\langle yP_x\rangle$ and $\langle xP_y\rangle$, and z_{PPM1} and z_{PPM2} are the positions of PPM1 and PPM2 along the z axis. Expressions for both intrinsic moments have been given because, in general, the magic point will not be at the same z position for both the horizontal and vertical directions in the transverse plane.

2.5.2 Beam position modulation

The average horizontal beam position at the IPMs is defined as

$$x_i = \frac{\left(x_i^+ + x_i^-\right)}{2} \tag{2.23}$$

where $i = \{1, 2, 3\}$ denotes IPM1, IPM2, or IPM3; and x_i^+ and x_i^- are the beam positions during spin + and − at the source, respectively. Beam position modulation correlated to the spin state of the beam is defined as

$$\Delta x_i = \frac{\left(x_i^+ - x_i^-\right)}{2} . \tag{2.24}$$

Similar expressions give the average and helicity-correlated beam position in the vertical, or y-axis, direction.

The false analyzing power arising from helicity correlated beam position modulations can be written in the form [2]

$$\begin{aligned}\Delta A_z = &\left(\tfrac{\Delta x_1 + \Delta x_2}{2}\right)(a_x x_1 + b_x x_2 + c_x) + \left(\tfrac{\Delta x_1 - \Delta x_2}{2}\right)(d_x x_1 + e_x x_2 + f_x) + \\ &\left(\tfrac{\Delta y_1 + \Delta y_2}{2}\right)(a_y y_1 + b_y y_2 + c_y) + \left(\tfrac{\Delta y_1 - \Delta y_2}{2}\right)(d_y y_1 + e_y y_2 + f_y) .\end{aligned} \tag{2.25}$$

The twelve parameters $(a_x \cdots f_y)$ are determined from calibration testing. During the testing, the beam position is purposely modulated in phase with the spin state sequence and the false asymmetry affected by the modulation is regressed against equation 2.25. For more details on how the calibration scans are performed, see section 2.6.5.

2.5.3 Beam size modulation

The average horizontal beam size at the IPMs is defined as

$$\sigma_{x_i} = \frac{\left(\sigma_{x_i^+} + \sigma_{x_i^-}\right)}{2} \tag{2.26}$$

where $i = \{1, 2, 3\}$ denotes IPM1, IPM2, or IPM3; and $\sigma_{x_i^+}$ and $\sigma_{x_i^-}$ are the standard deviations of the beam intensity distributions in x during spin + and − at the source, respectively. Beam size modulations correlated to the spin state of the beam are defined as

$$\Delta\sigma_{x_i} = \frac{\left(\sigma_{x_i^+} - \sigma_{x_i^-}\right)}{2} . \tag{2.27}$$

Similar expressions give the average and helicity-correlated beam size in the vertical, or y-axis, direction.

The false analyzing power arising from helicity correlated beam size modulations can be written in the form [2]

$$\Delta A_z = \alpha_x \sigma_{x_1} \Delta\sigma_{x_1} + \beta_x \sigma_{x_{2,3}} \Delta\sigma_{x_{2,3}} + \alpha_y \sigma_{y_1} \Delta\sigma_{y_1} + \beta_y \sigma_{y_{2,3}} \Delta\sigma_{y_{2,3}} \ , \quad (2.28)$$

where 2,3 indicates IPM2 or IPM3, respectively. The four parameters are determined from calibration testing. During the testing, the beam size is purposely modulated in phase with the spin state sequence and the false asymmetry affected by the modulation is regressed against equation 2.28. For more details on how the calibration scans are performed, see section 2.6.5.

2.6 Systematic error minimization

The final sections of this chapter present some of the considerations which are made during regular parity data taking so that systematic errors in the measurement of A_z can be minimized.

2.6.1 Wien filter and beam line helicity reversal

The longitudinal analyzing power A_z is a measure of the dependence of the scattering asymmetry on the spin direction *at the target.* Measurements of A_z taken with different orientations of the spin at the ion source and the cyclotron *with respect to the target* provide important checks on the consistency of the results.

An error in the measurement of A_z arising due to systematic errors correlated with the spin state of the beam at OPPIS can be minimized by rotating the Wien filter assembly and, therefore, reversing the spin direction of the beam at the cyclotron entrance. By reversing the polarity of the solenoid

magnets in the $4A/2$ beam line, also referred to as beam line helicity reversal, a further reduction of false A_z can be effectively accomplished by decoupling the systematic effect of coherent beam energy modulation from systematic errors arising due to other helicity-correlated beam parameters. Thus, there are four possible Wien filter/beam line helicity configurations. Table 2.2 shows the effect on the helicity at the target for the various configurations.

Spin state at OPPIS	Wien filter setting	Spin direction in cyclotron	SD-SD polarity	(WF/BL) Configuration	Helicity at target
↑(+)	+	$+y$	+	(+,+)	+
↓(−)		$-y$		1	−
↑(+)	+	$+y$	−	(+,−)	−
↓(−)		$-y$		2	+
↑(+)	−	$-y$	+	(−,+)	−
↓(−)		$+y$		3	+
↑(+)	−	$-y$	−	(−,−)	+
↓(−)		$+y$		4	−

Table 2.2: *Summary of Wien filter/beam line configurations.*

The NOVA reduction code calculates the asymmetry of an event pair based on the difference of the subtractor signal for the two *spin states at OPPIS*. Therefore, the measured asymmetry in configurations 2 and 3 must be multiplied by -1 to obtain the correct sign for A_z. In contrast, helicity-correlated offsets arising from modulations of beam parameters introduced downstream of the source would change sign in configurations 2 and 4 relative to 1 and 3. Let Δ_{OPPIS} denote the intrinsic helicity-correlated offset arising from helicity-correlated parameters at the ion source, such as coherent energy modulation. And let Δ_{cyc} denote the helicity-correlated offset arising from parameters correlated to the spin direction in the cyclotron which are not measured downstream of the ion source, such as beam halo, or spin dependent scattering in

the stripping foil. Any residual helicity-correlated offset arising due to the spin direction at the source or in the cyclotron will manifest as non-zero Δ_{OPPIS} or Δ_{cyc} in the corrected A_z.

The asymmetry (ϵ_1) in configuration 1 is

$$\epsilon_1 = A_z + \Delta_{OPPIS} + \Delta_{cyc} \,, \tag{2.29}$$

where A_z has been corrected for the systematic effects of coherent beam parameters measured in the $4A/2$ beam line. Using similar terms for the other three configurations, a summary of the four configurations and the measured asymmetry is shown in Table 2.3. The parity violating analyzing power is obtained from the 4 types of asymmetry measurements as:

$$A_z = \frac{1}{4}\left(\epsilon_1 - \epsilon_2 - \epsilon_3 + \epsilon_4\right) \,. \tag{2.30}$$

Configuration	Measured asymmetry
1	$\epsilon_1 = A_z + \Delta_{OPPIS} + \Delta_{cyc}$
2	$\epsilon_2 = -A_z + \Delta_{OPPIS} - \Delta_{cyc}$
3	$\epsilon_3 = -A_z + \Delta_{OPPIS} + \Delta_{cyc}$
4	$\epsilon_4 = A_z + \Delta_{OPPIS} - \Delta_{cyc}$

Table 2.3: *Summary of the measured asymmetry in the four Wien filter/beam line tune configurations. The four configurations allow a decoupling of the systematic effect of coherent beam energy modulation from other systematic errors which are measured downstream of the ion source.*

Equation 2.30 assumes an equal amount of data in each of the four configurations during the measurement of A_z. If the condition for equal statistics is not met, then the calculation of A_z must include a proper weighting function. Also implicit in the equation is that the systematic effects Δ_{OPPIS} and Δ_{cyc} are constant in each beam line configuration. This is usually not the case during

regular parity data taking. Equation 2.30 can be used, however, to estimate the magnitude of any residual systematic errors.

2.6.2 Beam size convergence

In the absence of external magnetic fields, the spin axis of a free particle will not precess. Also, there are no magnetic steering or focussing elements along the final 7 m of the $4A/2$ beam line. Therefore, if the trajectory of a proton in the beam is not parallel to the z-axis, the first moment arising from that proton will simply vary linearly with distance, z, along the beam line. Since the first moment of the beam is proportional to the linear sum of the first moments of the individual protons, the first moment of the beam will also vary linearly with z, passing through zero at some location (the magic point). This is normally close to the location of the beam waist. By adjusting the beam focusing, the first moment can be made to pass through zero at the magic point.

Figure 2.23 shows an example of a linear convergence of intrinsic first moment xP_y along the $4A/2$ beam line. In this example, the intrinsic first moment converges as it approaches the target (right of figure). The intrinsic moments at PPM2 are related to the moments at PPM1 by the ratios

$$R_y \equiv \frac{\langle yP_x \rangle_2}{\langle yP_x \rangle_1} \; and \; R_x \equiv \frac{\langle xP_y \rangle_2}{\langle xP_y \rangle_1} \, . \tag{2.31}$$

One of the main objectives in a four week long data run is to maintain a consistent beam line tune before and after beam line helicity reversal. If the beam size convergence is consistent upon beam line helicity reversal, then the sensitivity of the parity apparatus to intrinsic first moments of polarization will also be more consistent in both beam line tunes.

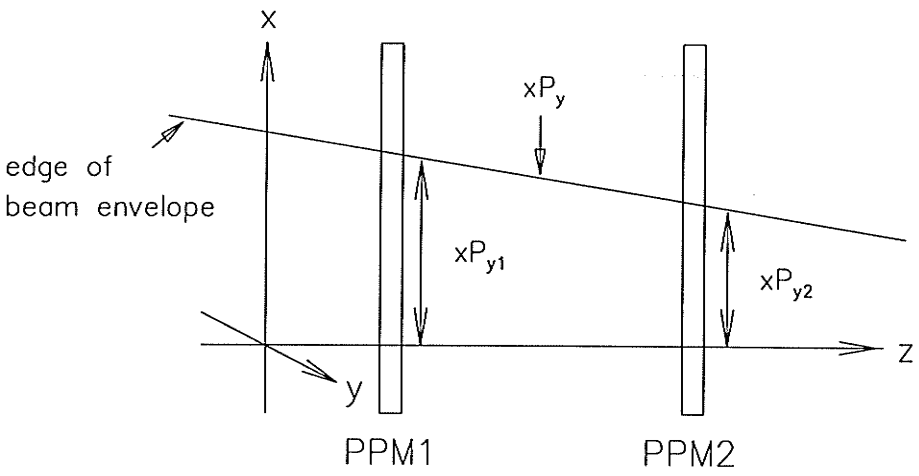

Figure 2.23: *Example of linear intrinsic moment convergence. The intrinsic moment scales linearly with the size of the beam. As the beam converges from left to right in the figure, the intrinsic moment converges as well. The ratio of convergence is found from correlation analysis of data measured at both PPMs.*

2.6.3 Beam energy modulation compensation

Beam energy modulation compensation is an applied intrinsic energy modulation which is introduced to the beam at the source. The compensation is introduced by applying a spin-correlated square wave voltage bias to the sodium ionizer cell (refer to Figure 2.3). The purpose of the compensation is to cancel the intrinsic energy modulation produced intrinsically at the source and provide a beam with zero net coherent energy modulation for injection into the cyclotron.

Approximately once per day during regular data taking, the beam energy spectrometer is used to estimate the intrinsic energy modulation produced at the source. Usually the source is tuned to minimize coherent beam intensity and energy modulation. Unfortunately, however, after tuning, a small intrinsic energy modulation will often remain in the beam. Moreover, the result of the measurements consistently show that the source produces a systematic positive intrinsic energy modulation (section 3.4.1). This means that the source

produces the spin $\uparrow$ state with systematically higher energy than the spin $\downarrow$ state. Beam energy modulation compensation is able to reduce the beam energy in the spin $\uparrow$ state and thus remove coherent beam energy modulation in the injected beam.

2.6.4 "Box balance"

"Box balance" scans are calibration runs, conducted every 1-3 days during regular data taking, designed to minimize the systematic effect of correlated intensity modulation. The scans investigate the sensitivity of the parity apparatus to enhanced CIM (introduced via the photoneutralization laser) over a range of DC voltage levels, corresponding to different settings of the fine gain, g, of the TRIC1 preamp output.

Figure 2.24 shows a graph of a typical box balance scan. This particular scan was taken at the beginning of the Jul98 data run. Each data point represents roughly 5 minutes of data acquisition time.

The box balance scans are taken with unpolarized beam and with the injection line feedback loops on, which maintains the nominal beam intensity at 200 nA. These scans are important to conduct as the sensitivity of the parity apparatus to CIM varies with changing beam conditions, and operating the subtraction module at the ideal DC level will minimize the net systematic error in the measurement of A_z.

2.6.5 Position feedback loop

The position feedback system locks the beam on the neutral axis and minimizes false analyzing power by reducing the amplitude of oscillations of the beam about this axis. The feedback system also allows for small modifications to the neutral axis beam position to be made, online, prior to individual data runs.

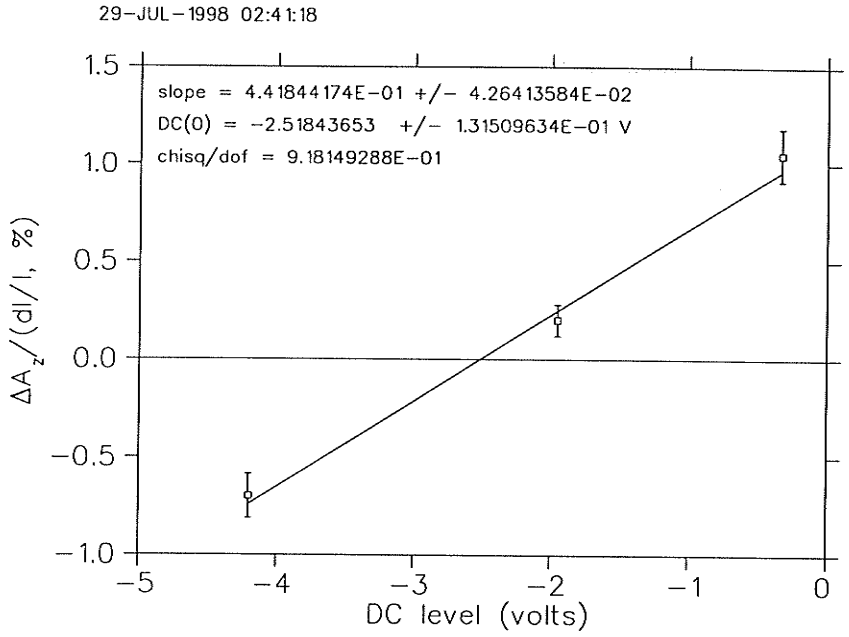

Figure 2.24: *A typical box balance calibration scan, taken during the Jul98 data run. The plot shows the sensitivity of the TRIC difference signal to CIM as a function of the subtractor box DC level. The data were taken with CIM of approximately* 0.1%. *This particular scan gave an ideal DC level of* $-2.6V$ *for zero sensitivity to CIM.*

The beam position is stabilized by sending position corrections to the two ferrite core steering magnets (FCSMs). Each FCSM can steer the beam in the horizontal and vertical directions using four sets of steering coils (H1,V1,H2 and V2). The correction signals are processed by a custom built, dedicated, pulsed integrating feedback amplifier (PIFA).

The PIFA is a single width NIM module which integrates the error signals from the beam centroid evaluator (BCE). The BCE forms an analog voltage signal, proportional to the position of the beam centroid on the IPM strips, by using a combination of summing amplifiers and analog dividers. The BCE signals are integrated over an entire event pair in order to reduce high frequency noise pickup from the target pump and beam position instability.

PIFA alternates between integrating loop 1 (H1 and V1) and loop 2 (H2 and V2). A change in integration from one loop to the other is triggered by a negative going NIM signal at the rear panel "trigger" input of the PIFA module. When a negative trigger is received, PIFA sends the output signal to the front panel of the module and switches integration to the loop it is not integrating at the time of the trigger. The PIFA is gated to the IPM/TRIC integration period so that beam scatter caused by the rotating PPM blades will not affect the correction signal.

The PIFA correction signals are sent to the FCSMs during the dead time at the end of the last substate of an event pair (every 400 ms). Because the feedback loop makes corrections to the nominal beam position at the end of an event pair, the system does not correct helicity-correlated modulation of beam position.

In addition to the above features, the DC level inputs on the PIFA module can be used to create an enhanced coherent beam position modulation by applying a square wave voltage bias in phase with the spin flip. The helicity-correlated beam position modulation studies—usually conducted once or twice during a four week data run—allow for a systematic study of the sensitivity of the parity apparatus to coherent modulations of the beam position about the neutral axis position. The steering magnets, which are wired in normal data taking mode so that deflections of the beam position in the vertical and horizontal directions can be made independently, can be re-wired in quadrupole mode thus creating a controlled, helicity-correlated, change in beam size (beam breathing).

Unfortunately, because the FCSMs are used to create an artificially enhanced beam breathing, the beam position can not be properly stabilized during the beam size modulation study. It will be seen in the next chapter that the sensitivity of the parity apparatus to beam breathing can not be sufficiently

determined to correct the main parity data for the effect of this systematic error.

The following chapter will present the final result of this analysis of the TRIUMF E497 parity experiment.

Chapter 3

E497 data analysis and results

3.1 Introduction

This analysis of the parity experiment is based on three major data runs, each approximately one month long in duration, acquired between February 1997 and June 1999. These runs represent the culmination of fifteen years of experimental effort. The effort includes many shorter test runs when systematic errors were studied and techniques were developed to minimize these errors. The analysis of these data focuses on developing techniques to treat all the major data runs in a consistent manner.

During each of the major data runs, only half of the running time is spent on investigating the parity violating component of the proton-proton interaction. The other half of the running time is spent on tune-up and systematic error calibrations.

Tuning at OPPIS is done to minimize the systematic effect of beam energy and intensity modulations. Also, investigations of the sensitivity of the parity apparatus to coherent modulations of beam position, beam size, and transverse moments of polarization are conducted at interleaved periods of data taking. As discussed in section 2.6.1, to cancel the net effect of coherent beam energy modulation, the beam line helicity is periodically reversed. This requires retuning of the beam line magnets. Beam line helicity reversal is performed approximately every three days of data acquisition time. The amount of data acquired in each beam line helicity produces a measurement of the analyzing power with a raw statistical error bar of roughly $\pm 1.2 \times 10^{-7}$.

The process of refining the analysis began with the latest data set (May99). The technique developed was extended to the other two data sets (Feb97 and Jul98), and this required a more general treatment of data quality cuts and of estimation of systematic error sensitivities. The process became iterative as each data set presented new challenges and called for a refinement in the

method of analysis. There are three stages in the analysis process: (i) performing data quality cuts on the raw data to remove spurious events; (ii) conducting calibration tests; and (iii) application of systematic error corrections to the measured analyzing power. These procedures and the final result of the analysis are presented in this chapter. A brief description of each of the major data runs is presented in the following section.

3.2 Summary of data runs

3.2.1 *Feb97*

The Feb97 data run ran from 12 February 1997 through 12 March 1997. Eight sets of data were acquired with a total raw asymmetry statistical error of approximately 0.5×10^{-7}.

The Feb97 run is the first major run that is included in this analysis of the results of the experiment. Over two hundred polarized data runs were acquired in total. Data were taken in all four Wien filter/beam line configurations. Feb97 Set 8 data were taken with a $2.5\frac{mg}{cm^2}$ stripping foil (see section 2.1.2). This foil, of the same length and width, replaced the $5\frac{mg}{cm^2}$ stripping foil which was used throughout the first seven sets of Feb97. In addition to using a different stripping foil for Set 8, it is seen that the set likely has a significantly different first moment sensitivity. For these reasons, Set 8 is not included in the final analysis. All data taken during Feb97 were acquired using IPM3 in fast feedback mode.

The Feb97 run is the only major data run which used IPM3 in fast feedback mode. Because of this fact, it is difficult to calibrate and estimate systematic uncertainty to coherent beam position and beam size modulations as well as extrinsic first moments of polarization. The difficulty arises in comparison of

the beam position and size during the Feb97 run versus the Jul98 and May99 runs which used IPM2 in fast feedback mode. For comparison purposes, measurements taken at IPM3 during the Feb97 run have been projected backward along the $4A/2$ beam line to the position of IPM2. Beam position measurements used in the calculation of extrinsic moments must be projected to the PPMs. These projections increase the uncertainty associated with systematic error corrections. The effect on the distribution of the systematic error correction can be seen in section 3.6.1.

The Feb97 run has been independently analysed and presented as the focus of a Ph.D. thesis [2]. The result of that analysis was a measurement of $A_z = (0.33 \pm 0.56(stat.) \pm 0.34(syst.)) \times 10^{-7}$. The largest systematic error correction to these data was for the systematic effect of intrinsic first moment $\langle xP_y \rangle$. Unfortunately, work was not completed on the systematic effect of beam energy modulation during the previous analysis.

3.2.2 *Jul98*

The Jul98 data run ran from 20 July 1998 through 21 August 1998. Nine sets of data were acquired with a total raw asymmetry statistical error of approximately 0.4×10^{-7}.

The Jul98 data run is, statistically, the largest major run that is included in this analysis of the parity experiment. Nearly three hundred polarized data runs were acquired in total. Data were taken in the + Wien filter setting. All sets were acquired using IPM2 in fast feedback mode. The asymmetry data were taken with a $2.5 \frac{mg}{cm^2}$ stripping foil.

The Jul98 data run includes the most comprehensive online calibration of the effect of helicity-correlated beam energy modulation. Nearly 30 energy modulation calibration runs were conducted and over 60 measurements of the

intrinsic energy modulation at OPPIS were taken. Most of the asymmetry data were acquired with beam energy modulation compensation applied at the source.

In an attempt to reduce the intrinsic first moment sensitivity based on what had been inferred from the Feb97 data, the geometric beam size convergence was set to 0.85 in x and y. Unfortunately, the intrinsic first moment sensitivity found from direct regression (section 3.5.3) is not consistent in both beam line helicities, and this approach did not result in zero sensitivity to the intrinsic first moment.

3.2.3 *May99*

The May99 data run ran from 19 May 1999 through 23 June 1999. The five week May99 data run was successful, and approximately three weeks of usable data were obtained. A $1.4\frac{mg}{cm^2}$ stripping foil was used throughout the data run. Seven sets of data were acquired with a raw statistical error of approximately 0.4×10^{-7} in the measured asymmetry. Statistical variation of the raw asymmetry during the May99 run is approximately 20% noisier than the previous Jul98 data run. The cause of the instability is unknown, and a careful examination of the beam parameters is undertaken in the analysis of this and all major data runs.

Based on conclusions drawn from earlier data runs [31], the geometric size convergence of the beam was set to 0.86 and 0.80, in x and y, respectively, in an attempt to eliminate sensitivity to intrinsic first moments. Although not eliminated, a reduction of the intrinsic first moment sensitivity—with respect to previous data runs—was achieved.

3.3 Data reduction

This thesis will refer to three distributions of analyzing power: A_z^{raw} which is the measured raw asymmetry multiplied by beam line helicity before beam quality cuts, $A_z^{reduced}$ which is the uncorrected analyzing power after beam quality cuts, and A_z^{corr} which is the final result after beam quality cuts and systematic error corrections. Future reference to the three distributions will imply the total distribution of the combination of the three major data runs (Feb97, Jul98 and May99) unless otherwise stated. In addition, sets 1-7 will refer to sets 1-7 of the Feb97 run, sets 8-16 will refer to sets 1-9 of the Jul98 run, and sets 17-23 will refer to sets 1-7 of the May99 run. Thus, the final parity data set, hereafter referred to as the grand set, consists of 23 sets of asymmetry data.

Twelve sets of the grand set were acquired in (Wien filter,beam line tune) configuration (+,+); 9 in (+,−); 1 in (−,+); and 1 in (−,−). Over 3.8 million event pairs were recorded to tape with slightly more than half taken in + beam line helicity. In all, 375 polarized runs were taken in positive beam line helicity and 368 runs were taken in negative beam line helicity. In addition to these polarized data runs, calibration runs conducted during the acquisition of the grand set number 80 position modulation runs, 81 size modulation runs, 42 energy modulation runs, and 109 neutral axis scans. All runs were recorded on magnetic tape and processed via the offline NOVA reduction routine. In the remainder of this thesis, the Feb97 data run may sometimes be treated as an independent subset of the grand set. This was done because data acquired during the Jul98 and May99 data runs used IPM2 in fast feedback mode, in contrast to the Feb97 data run which used IPM3 in fast feedback mode.

3.3.1 Raw analyzing power

Table 3.1 summarizes the raw analyzing power and the reduced chi-squared of the 23 sets: $A_z^{raw} = (1.43 \pm 0.22) \times 10^{-7}$. The uncertainty of A_z^{raw} is the standard error estimated from the statistical distribution of the event pairs. Figure 3.1 shows the distribution of raw analyzing power as a function of set. The large value of reduced chi-squared, $\chi^2_\nu = 11.3$, suggests that one or more significant systematic errors are present within the raw analyzing power. The remainder of this chapter focuses on removing spurious events in the data stream as well as applying systematic error corrections to improve confidence in the final result. The next section will discuss the *timecuts* process which is the first data reduction procedure implemented to improve data quality.

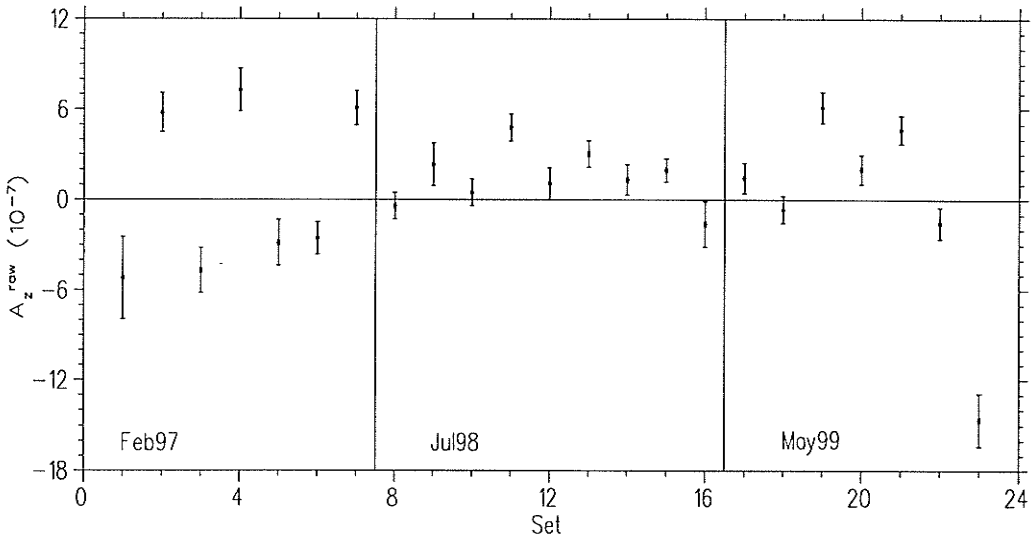

Figure 3.1: A_z^{raw} *as a function of set. The raw analyzing power, measured in units of* 10^{-7}*, during the Feb97 data run is* 1.45 ± 0.52*; during the Jul98 data run is* 1.64 ± 0.32*; and during the May99 data run is* 0.90 ± 0.39*. The reduced chi-squared of the 23 sets is* 11.3 *which suggests one or more significant systematic errors occurred during the measurement of the raw analyzing power.*

Set,(Wien filter,beam line)	$A_z^{raw}(10^{-7})$	2-events
1,(+,+)	-5.21 ± 2.72	91,834
2,(+,−)	5.78 ± 1.30	221,066
3,(+,+)	-4.69 ± 1.50	140,468
4,(+,−)	7.29 ± 1.44	134,541
5,(+,+)	-2.84 ± 1.51	123,851
6,(−,+)	-2.55 ± 1.07	213,246
7,(−,−)	6.09 ± 1.13	171,494
8,(+,+)	-0.42 ± 0.87	205,437
9,(+,−)	2.32 ± 1.41	74,728
10,(+,+)	0.47 ± 0.88	185,003
11,(+,−)	4.80 ± 0.90	163,406
12,(+,+)	1.06 ± 1.05	135,967
13,(+,−)	3.02 ± 0.88	185,143
14,(+,+)	1.31 ± 1.00	158,702
15,(+,−)	1.93 ± 0.77	229,885
16,(+,+)	-1.60 ± 1.50	80,254
17,(+,+)	1.42 ± 0.99	198,785
18,(+,−)	-0.65 ± 0.88	272,415
19,(+,+)	6.12 ± 1.03	206,388
20,(+,−)	2.00 ± 0.97	244,813
21,(+,+)	3.31 ± 0.94	221,214
22,(+,−)	-1.55 ± 1.03	157,219
23,(+,+)	-14.62 ± 1.75	62,130
Average (χ^2_ν)	1.43 ± 0.22 (11.3)	3,874,801
(+,+)	0.56 ± 0.33	1,806,845
(+,−)	2.32 ± 0.33	1,683,216
(−,+)	-2.55 ± 1.07	213,246
(−,−)	6.09 ± 1.13	171,494

Table 3.1: *Summary of sets of A_z^{raw}. See Figure 3.1 for a graphical display of these data.*

3.3.2 *Timecuts*

The measurement of A_z is particulary susceptible to ac noise and pickup from the ion chambers due to the fact that the TRICs are operated in current mode. The ac noise appears as enhanced width of the digitized A_z distribution.

A reduction procedure was designed to reduce and categorize the statistical sample of asymmetry data. The procedure is called the *timecuts* process; this is a subjective test in which continuous blocks of asymmetry data are rejected. The decision to remove blocks of data is based on whether the subtractor box output had become anomalously noisy—with respect to the run as a whole—indicating a sudden change to the experimental conditions.

The timecuts procedure essentially consists of categorizing, on a run-by-run basis, the quality of the asymmetry data. This is accomplished by grouping the data into one of two categories: "good" or "bad". Figure 3.2 shows a typical time plot of subtractor noise for a "good" and "bad" run. The standard deviation of the digitized ion chamber difference signal, denoted by σ_{eps}, is calculated for consecutive bundles of 50 event pairs. Deciding which group a particular run should be placed in is determined from a visual check of the statistical spread of the asymmetry signal along the time axis. The choice of 50 event pairs per bundle should enable identification of changing beam conditions over a 20 second timescale—or longer—while ensuring that the standard error of σ_{eps} is approximately four standard deviations from zero. At this level of statistical resolution, systematic variation of the asymmetry data becomes clearly identifiable; as the figure shows. The *timecuts* process was first implemented for the analysis of the May99 run. To ensure a consistent treatment of the grand set, the process has been applied to all three major data runs.

A total of 46 runs have been placed in the "bad" category and removed from the grand set. Many of the "bad" runs are short—parity collaborators likely noticed degenerating beam conditions online and took corrective actions.

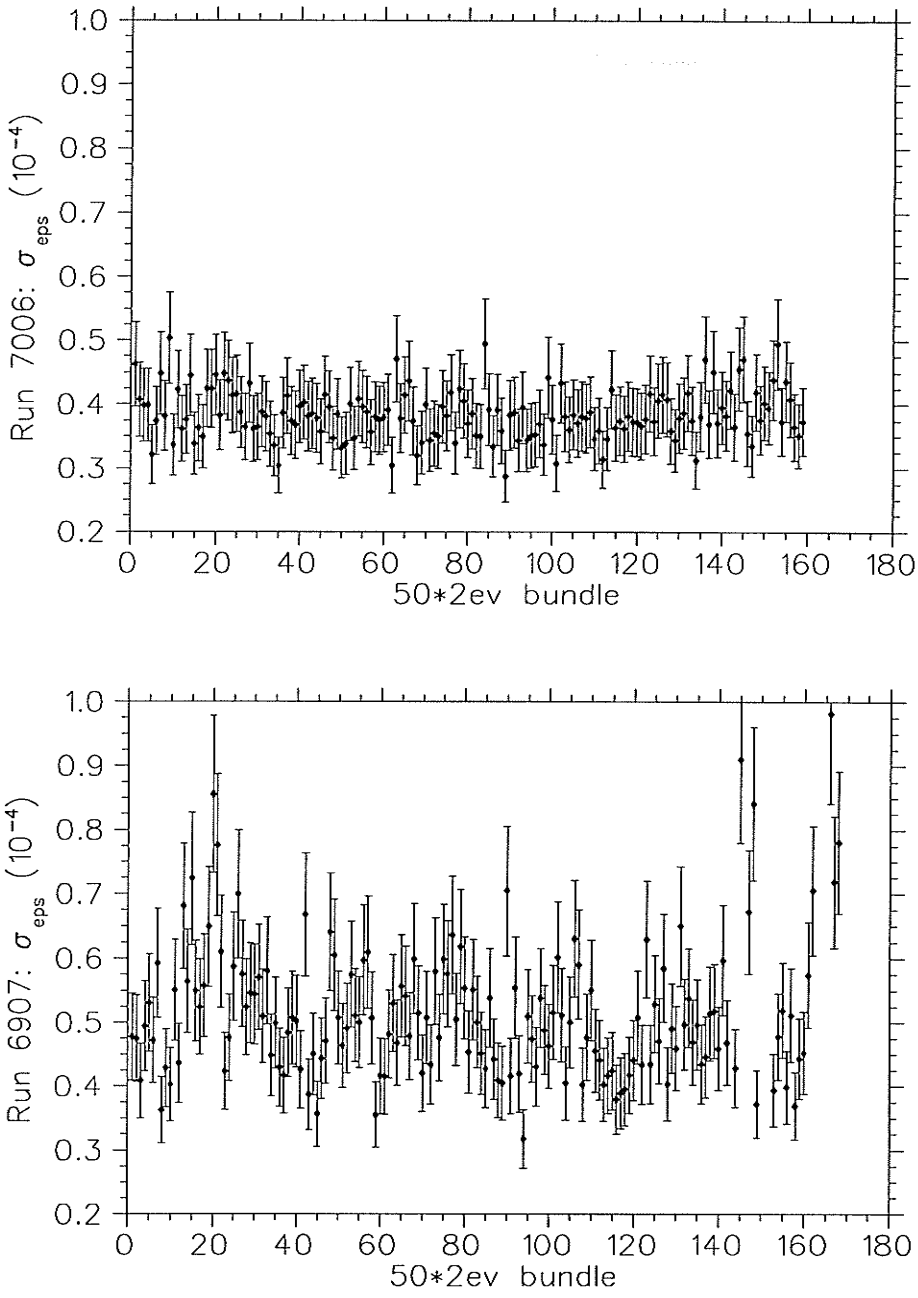

Figure 3.2: *Time plot of subtractor noise for a "good" (top) and "bad" (bottom) run. Both runs are taken from the May99 data set. Notice how the subtractor box signal distribution increases in width near the end of run 6907. All runs which display instability in the distribution of the asymmetry signal, common with run 6907, are removed from the grand set. A 50*2ev bundle is a bundle of 50 consecutive event pairs.*

These runs represent a small portion of the grand set and no significant loss of statistics results from their removal. The entire process reduced the raw data sample by only a few percent.

Because of the varying beam quality and detector noise conditions during the May99 data run—even after the *timecuts* procedure is applied—weighted averages were used in evaluating beam parameter values and A_z values. Weighting each data bundle by $1/\sigma^2$ gave less weight to blocks of data which had large statistical uncertainty. By using the method of weighted averages on the grand set, further compensation for time varying changes in σ_{eps} is made. Data reduction to improve the quality of the beam parameter distributions is explored in the following section.

3.3.3 Beam quality cuts

Beam quality cuts are placed on all major beam properties. This is done to minimize systematic error in the estimate of the false analyzing power which is subtracted from the main signal. During the Feb97 run, sparks in one of the IPM3 foil packs created the appearance of large excursions of the beam from its polarization neutral axis. This may have led to anomalously large false corrections if the data stream were not treated carefully [2]. Table 3.2 summarizes the acceptance windows for each of the parameters considered for beam quality cuts during the analysis.

There are two types of beam quality cuts: hard cuts and soft cuts. Hard cuts on a beam parameter reject all event pairs that contain measurements of the beam parameter which are outside of an acceptance window. The soft cuts remove events, using a nine stage iterative process, outside of three standard deviations of the beam parameter centroid. Hard cuts on the beam size distribution are placed on the centroids of the beam size and are applied individually for the Feb97, Jul98, and May99 runs. Hard cuts on the neutral axis

Beam Parameter	Acceptance Window
Neutral axis x, y	± 0.3 mm
Avg IPM positions	$\pm 3\sigma$ (soft)
σ_x, σ_y	± 1.0 mm
IPM skew	± 0.2 mm
Intensity	196-204 nA
Intrinsic Moments	± 3.0 mm

Table 3.2: *Summary of data reduction cuts. Except for the beam intensity, the center of the acceptance window for each of the parameters is the measured centroid of the beam parameter distribution. The hard cuts are wide enough to include at least four standard deviations for each of the beam parameters.*

positions are centered on the "neutral axis". Further hard cuts, on the beam skew and intrinsic first moments, are mainly precautionary and are centered on zero skewness and 0 mm, respectively. All soft cuts are applied individually for the Feb97, Jul98, and May99 data runs.

Other quality cuts

Occasionally during data-taking, a run may lack a polarized beam or may be subjected to unstable beam conditions in the cyclotron which were not observed online. There may be any number of other systematic errors in the run which may justify exclusion of the data once investigations of each run are made offline. The grand set was carefully checked and reduced by eliminating candidate data runs taken with spurious beam conditions.

The entire data reduction process reduced the size of the grand set by 30%. The process significantly increased the quality of the data sample, which can be seen in the following section.

3.3.4 Reduced data set

The reduced data sample includes all runs categorized as "good" by the time-cuts procedure. The results are shown in Table 3.3: $A_z^{reduced} = (1.55 \pm 0.27) \times 10^{-7}$. Data quality is improved as suggested by the change in χ^2_ν from 11.3 to 5.48. A helicity dependent offset of $\pm 0.3 \times 10^{-7}$ exists in the reduced data, as compared to the raw data which contained an offset of $\pm 0.5 \times 10^{-7}$. The error estimates are calculated from the standard error of the mean of the distribution on a set by set basis. The average quantities are weighted averages of the set data. Figure 3.3 shows the reduced analyzing power as a function of set.

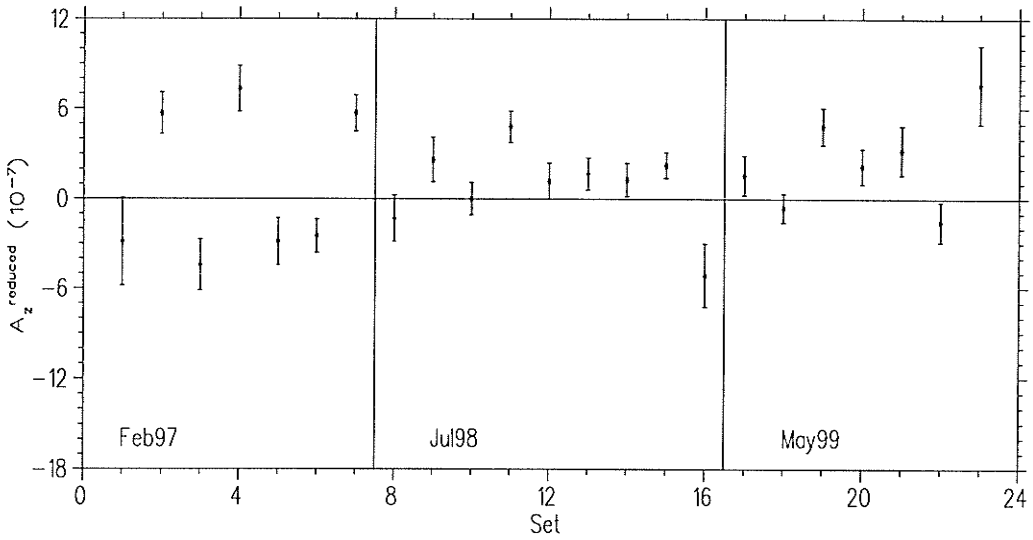

Figure 3.3: $A_z^{reduced}$ *as a function of set. Notice the improvement of the data quality once data reduction cuts have been implemented. The reduced analyzing power, measured in units of* 10^{-7}*, during the Feb97 data run is* 1.52 ± 0.55*; during the Jul98 data run is* 1.56 ± 0.39*; and during the May99 data run is* 1.56 ± 0.49*. The reduced chi-squared of the 23 sets is 5.48 which suggests one or more significant systematic errors exist within the reduced analyzing power.*

Set	$A_z^{reduced}(10^{-7})$	2-events
1	-2.88 ± 2.96	79,247
2	5.69 ± 1.39	195,364
3	-4.43 ± 1.72	105,557
4	7.35 ± 1.53	117,815
5	-2.86 ± 1.57	114,377
6	-2.50 ± 1.12	193,989
7	5.70 ± 1.21	150,106
8	-1.31 ± 1.54	66,653
9	2.61 ± 1.48	67,409
10	0.01 ± 1.09	118,274
11	4.79 ± 1.05	119,531
12	1.18 ± 1.19	104,276
13	1.68 ± 1.07	122,648
14	1.29 ± 1.11	125,672
15	2.24 ± 0.85	184,587
16	-5.13 ± 2.13	37,860
17	1.56 ± 1.32	115,246
18	-0.62 ± 0.96	221,423
19	4.84 ± 1.23	139,631
20	2.16 ± 1.17	147,932
21	3.21 ± 1.62	70,026
22	-1.55 ± 1.33	95,260
23	7.62 ± 2.63	24,469
Average (χ^2_ν)	1.55 ± 0.27 (5.48)	2,717,352
(+)	1.20 ± 0.40	1,251,394
(−)	1.84 ± 0.36	1,465,958

Table 3.3: *Summary of sets of $A_z^{reduced}$. See Figure 3.3 for a graphical display of these data.*

3.3.5 Beam parameters

A beam property is a characteristic of the beam, such as the beam size. A beam parameter is defined as the value of a beam property measured at a particular monitor in the parity beam line. An example of a beam parameter is $\Delta\sigma_{x_1}$: the helicity-correlated modulation of the beam size as determined from the standard deviation of the beam intensity distribution—along the x-axis—measured at IPM1. Beam parameters are used to estimate systematic error sensitivities and corrections.

Helicity-correlated beam parameters can introduce systematic shifts to the measured analyzing power. Helicity-correlated beam parameters include beam position and size modulations, beam intensity and energy modulations, and transverse polarization components.

All helicity-correlated beam properties must arise at the ion source. These modulations can be enhanced by the cyclotron and beam transport systems, resulting in coherent modulations of beam position, energy and size at the target. Coherent modulations of the beam position and size are coupled to a path length change through the ion chambers thus producing a false asymmetry.

Tables 3.4 and 3.5 display helicity-correlated beam position and size measurements for the Feb97 data run, and combined Jul98 and May99 data runs, respectively. It is important to re-iterate that IPM3 was used in fast feedback mode for the Feb97 data run. This fact makes a direct comparison of all beam position and size measurements taken throughout the grand set impossible. Multiple scattering upstream of IPM3, together with AC noise picked up from target and pump vibrations, increased the uncertainty of beam position measurements at IPM3 (in relation to measurements at IPM2); hence, the feedback loops and overall beam stability were much worse during the Feb97 data run. This can be seen in the increased statistical uncertainty of measurements taken during the Feb97 data run. Table 3.6 summarizes the other helicity-correlated

beam parameters of the grand set which can be combined into one data set. Figure 3.4 displays the measured intrinsic first moments as a function of set.

	Wien filter +		Wien filter −	
Parameter	Beam line +	Beam line −	Beam line +	Beam line −
$\Delta\sigma_{x_1}(nm)$	119 ± 49	-137 ± 43	-101 ± 59	8 ± 48
$\Delta\sigma_{x_3}(nm)$	65 ± 79	-156 ± 76	-110 ± 118	-45 ± 91
$\Delta\sigma_{y_1}(nm)$	126 ± 44	-212 ± 44	-36 ± 54	41 ± 45
$\Delta\sigma_{y_3}(nm)$	81 ± 75	-200 ± 72	-54 ± 116	-11 ± 84
$\Delta x_1(nm)$	5 ± 33	19 ± 28	-34 ± 40	38 ± 36
$\Delta x_3(nm)$	-30 ± 34	-40 ± 34	10 ± 46	4 ± 37
$\Delta y_1(nm)$	-46 ± 26	89 ± 27	-7 ± 33	-10 ± 27
$\Delta y_3(nm)$	-27 ± 36	-12 ± 33	24 ± 55	-78 ± 43

Table 3.4: *Summary of helicity-correlated beam position and size for the Feb97 data run. The table only includes coherent beam position and size modulations related to the positions of IPM1 and IPM3.*

Averaged beam parameters are properties of the beam which are averaged over both spin states. These parameters include beam position and size, beam intensity and energy, and longitudinal polarization. Although average beam parameters can not create a false asymmetry, they can be adjusted to minimize the sensitivity of the apparatus to helicity-correlated modulations of beam parameters. Tables 3.7 and 3.8 display the averaged beam parameters for the Feb97 data run, and combined Jul98 and May99 data runs, respectively.

	Wien filter +	
Parameter	Beam line +	Beam line −
$\Delta\sigma_{x_1}(nm)$	-17 ± 38	0 ± 35
$\Delta\sigma_{x_2}(nm)$	8 ± 8	-35 ± 7
$\Delta\sigma_{y_1}(nm)$	-6 ± 37	1 ± 35
$\Delta\sigma_{y_2}(nm)$	17 ± 7	-37 ± 5
$\Delta x_1(nm)$	1 ± 14	-1 ± 6
$\Delta x_2(nm)$	7 ± 11	-9 ± 5
$\Delta y_1(nm)$	17 ± 11	3 ± 8
$\Delta y_2(nm)$	16 ± 10	2 ± 7

Table 3.5: *Summary of helicity-correlated beam position and size for the combined Jul98 and May99 data runs. The table only includes coherent beam position and size modulations related to the positions of IPM1 and IPM2.*

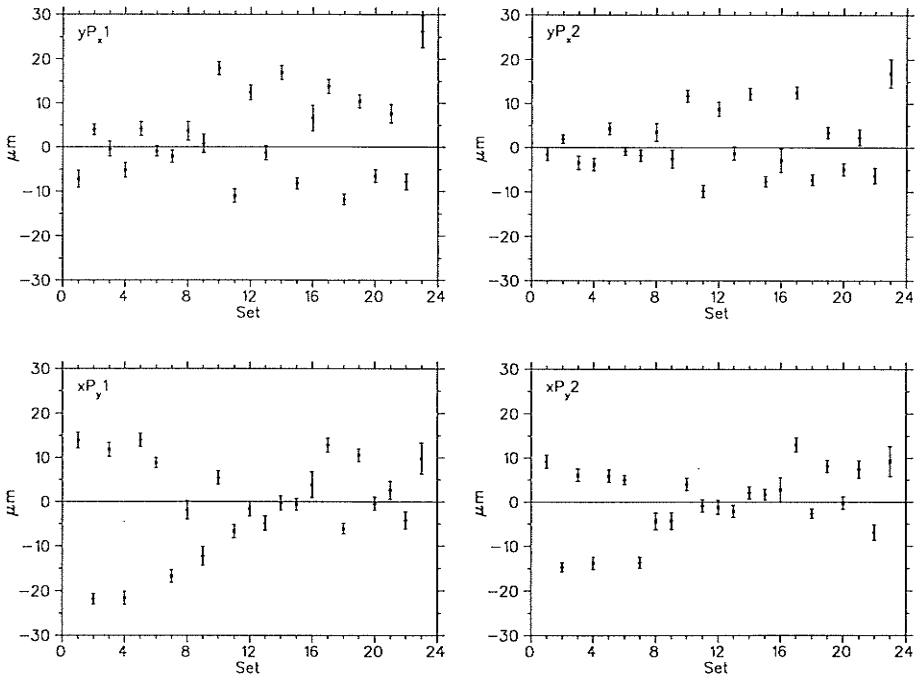

Figure 3.4: *Average intrinsic first moments of the grand set. In general, a convergence of the first moment from PPM1 to PPM2 can be seen for yP_x and xP_y*

	Wien Filter +		Wien Filter −	
Parameter	Beam line +	Beam line −	Beam line +	Beam line −
$A_z^{reduced}(10^{-7})$	0.65 ± 0.42	2.34 ± 0.38	-2.50 ± 1.12	5.70 ± 1.21
spin off A_z	0.58 ± 1.09	1.14 ± 0.99	-0.26 ± 2.44	0.77 ± 2.74
$P_x(10^{-4})$	-3.2 ± 0.9	8.3 ± 0.8	0.5 ± 2.1	6.7 ± 2.3
$P_y(10^{-4})$	7.6 ± 0.9	18.1 ± 0.8	-5.7 ± 2.2	-8.2 ± 2.4
$y_1 * P_x(\mu m)$	0.02 ± 0.01	-0.06 ± 0.01	-0.02 ± 0.02	-0.03 ± 0.01
$y_2 * P_x(\mu m)$	0.12 ± 0.03	-0.30 ± 0.03	-0.01 ± 0.06	-0.17 ± 0.06
$x_1 * P_y(\mu m)$	-0.04 ± 0.01	-0.08 ± 0.01	0.12 ± 0.04	0.12 ± 0.04
$x_2 * P_y(\mu m)$	-0.15 ± 0.04	-0.37 ± 0.04	0.46 ± 0.18	0.65 ± 0.20
$\langle yP_x \rangle(\mu m)$	15.3 ± 0.7	-10.3 ± 0.7	-1.5 ± 1.5	-3.9 ± 1.9
$\langle xP_y \rangle(\mu m)$	12.5 ± 0.7	-13.6 ± 0.7	13.8 ± 1.6	-30.3 ± 1.8
$\Delta I/I(ppm)$	-28 ± 1	52 ± 1	53 ± 2	-42 ± 2
ΔE *(estimated)*	3-20 meV			

Table 3.6: *Summary of helicity-correlated beam parameters of the grand set. Except for spin off A_z, systematic error corrections to the reduced analyzing power are calculated using measurements of the parameters in the table. Intensity modulation is measured at TRIC1.*

	Wien filter +		Wien filter −	
Parameter	Beam line +	Beam line −	Beam line +	Beam line −
$\sigma_{x_1}(mm)$	5.0654 ± 0.0002	5.0618 ± 0.0003	5.0719 ± 0.0003	5.1547 ± 0.0002
$\sigma_{x_3}(mm)$	6.0365 ± 0.0002	6.0765 ± 0.0002	6.0786 ± 0.0002	6.2569 ± 0.0002
$\sigma_{y_1}(mm)$	5.1094 ± 0.0003	5.1010 ± 0.0003	5.1335 ± 0.0004	5.1878 ± 0.0003
$\sigma_{y_3}(mm)$	5.9205 ± 0.0002	6.0251 ± 0.0002	5.8818 ± 0.0002	6.0616 ± 0.0002
$x_1(mm)$	0.018 ± 0.000	0.002 ± 0.000	-0.030 ± 0.000	-0.012 ± 0.000
$x_3(mm)$	-1.762 ± 0.000	-1.774 ± 0.000	-1.827 ± 0.000	-1.827 ± 0.000
$y_1(mm)$	-0.010 ± 0.000	0.002 ± 0.000	-0.014 ± 0.000	-0.003 ± 0.000
$y_3(mm)$	-0.723 ± 0.000	-0.707 ± 0.000	-0.617 ± 0.000	-0.621 ± 0.000
Intensity (nA)	199.9 ± 0.0	200.0 ± 0.0	200.0 ± 0.0	200.0 ± 0.0
P_z (%)	77 ± 1			

Table 3.7: *Summary of averaged beam parameters of the Feb97 data run. P_z is the longitudinal beam polarization, see section 3.6.3.*

	Wien filter +	
Parameter	Beam line +	Beam line −
$\sigma_{x_1}(mm)$	5.0518 ± 0.0004	5.1108 ± 0.0004
$\sigma_{x_2}(mm)$	4.3130 ± 0.0004	4.3660 ± 0.0003
$\sigma_{y_1}(mm)$	5.0486 ± 0.0004	5.0706 ± 0.0004
$\sigma_{y_2}(mm)$	4.1907 ± 0.0003	4.2122 ± 0.0003
$x_1(mm)$	0.001 ± 0.000	0.002 ± 0.000
$x_2(mm)$	-0.005 ± 0.000	-0.026 ± 0.000
$y_1(mm)$	0.006 ± 0.000	0.004 ± 0.000
$y_2(mm)$	-0.241 ± 0.000	-0.248 ± 0.000
Intensity (nA)	200.4 ± 0.0	200.3 ± 0.0
P_z (%)	74 ± 2	

Table 3.8: *Summary of averaged beam parameters of the combined Jul98 and May99 data runs. P_z is the longitudinal beam polarization, see section 3.6.3.*

3.4 External calibrations

3.4.1 Modulation calibrations at OPPIS

There exist naturally occurring helicity-correlated beam parameters which are produced at the optically pumped polarized ion source. Rigorous tuning of the source can minimize these modulations. Calibration studies of the systematic effect of these intrinsic properties of the source are important to conduct and can be done by purposely enhancing the modulations.

Helicity-correlated modulations artificially enhanced at the ion source produce false analyzing effects which can be monitored at the target. The systematic effect of position modulation at the source has been shown to be an order of magnitude smaller than the effect of beam energy modulation. Beam position modulation at the source is also expected to be strongly correlated to beam position and size modulations downstream in beam line $4A/2$. It will be seen in section 3.6.5 that a systematic error in the measurement of A_z arising from coherent modulations of the beam position and size in beam line $4A/2$ is insignificant in relation to the statistical uncertainty in the measurement of A_z. For these two reasons, the systematic effect of beam position modulations at the source are not corrected in the measurement of A_z.

Intensity modulation

As discussed in chapter 2, the ion source injection line contains a dedicated photoneutralization laser capable of producing enhanced CIM for diagnostic purposes. The data acquisition timing system is set so that 10 % of TRIC integration time is devoted to calibrating the effect of enhanced CIM. Figure 3.5 shows typical enhanced CIM data from a run taken during the May99 data run.

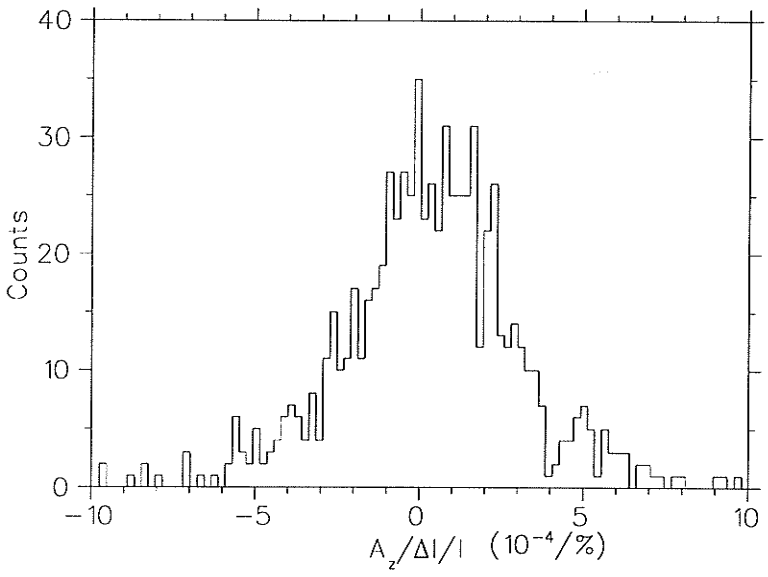

Figure 3.5: *CIM data taken during run 6559 (May99 data run). The plot shows a histogram of the measured asymmetry to* $\frac{\Delta I}{I}$ *during the CIM mode of run 6559. Data have been excluded for which* $|\Delta I/I| < 0.06$ *%. The mean sensitivity for these data is* $(227 \pm 97) \times 10^{-7}/\%$.

The false analyzing power produced by helicity-correlated modulations of beam intensity is given by [2]

$$\Delta A_z = \frac{\Delta I}{I} \times \left\langle \frac{A_z}{\frac{\Delta I}{I}} \right\rangle_{CIM} , \tag{3.1}$$

where the subscript CIM indicates that only data taken during the enhanced CIM mode of the data acquisition is used in the calculation. The term in $\langle\ \rangle$ represents the average $(A_z/\frac{\Delta I}{I})$ for all CIM event pairs measured during each month-long run. While the subtractor box is periodically tuned to minimize the sensitivity to CIM as described in section 2.6.4, a small but significant sensitivity remains in the data, which must be corrected for this effect.

During CIM data-taking, it is possible to lose enhanced $\frac{\Delta I}{I}$ due to misalignment of the CIM laser which causes the calibration data to become statistically uncertain. Because of the possibility of a misalignment, the CIM data have been reduced by excluding data for which $|\Delta I/I| < 0.06$ %. Table 3.9 displays

the results of the CIM data analysis.

Set	Sensitivity (10^{-7}/%)	CIM events	χ^2_ν
1-7	36 ± 19	83,636	1.00
8-16	138 ± 8	106,520	1.00
17-23	73 ± 11	90,955	1.00
All	86 ± 7	281,111	1.00

Table 3.9: *Sensitivities to* $\frac{\Delta I}{I}$. *The sensitivities are determined by averaging CIM data for which abs*$(\frac{\Delta I}{I}) \geq 0.06$ *%. The sensitivity determined by averaging all of the CIM data from the grand set is shown for purposes of comparison. The data runs are corrected separately using their corresponding sensitivities. The total systematic error correction applied to the grand set is* $(0.18 \pm 0.02) \times 10^{-7}$.

Coherent energy modulation

One of the largest contributors to systematic uncertainty in this experiment is helicity correlated energy modulation. The helicity-correlated energy modulation ΔE can not be determined simultaneously with parity data taking, but must be obtained from interleaved diagnostic measurements at the ion source. This section describes a reasonable estimate for this systematic error. The sensitivity to intrinsic energy modulation is expressed as:

$$\Delta A_z = \omega \Delta E, \tag{3.2}$$

where ΔE is coherent energy modulation at the source and ΔA_z is the resultant false analyzing power measured at the target.

Twenty-eight energy modulation calibration runs were conducted at interleaved periods of data-taking during the Jul98 data run. Fourteen additional runs were taken during the May99 data run and 13 runs during the Feb97 data

run. In each case, 100-1000 meV of peak to peak helicity-correlated energy modulation was applied to the 3 keV beam at the source using the method described in the previous chapter.

During the calibration runs, the beam is unpolarized. Other false effects correlated with energy modulation can be corrected independently. In particular, intensity modulation contributes a relatively large false asymmetry in the calibration data. Helicity-correlated beam position and size modulations (in beam line $4A/2$) were found to be consistent with zero and are not corrected for in the calibration data. The calibration data are fit using the method of least squares and on a run by run basis to the following equation:

$$\Delta A_z = b + m \times \frac{\Delta I}{I} \tag{3.3}$$

where ΔA_z is the false analyzing power and $\frac{\Delta I}{I}$ is the correlated intensity modulation measured during the calibration run. The sensitivity ω is determined from the fitted parameters as:

$$\omega = \frac{b}{\Delta E} \,. \tag{3.4}$$

Tables 3.10 and 3.11 summarize the results of the least squares fits. The uncertainties of the ω values are determined from the systematic uncertainty, δb, of the offset in the linear fit. Figure 3.6 shows the raw and corrected calibration data for runs taken in + beam line tune during the Jul98 data run. The measured effect of energy modulation during the various calibration runs is roughly the same magnitude as the systematic error correction due to $\frac{\Delta I}{I}$. Similar behaviour is seen in − beam line tune and in other data sets. Table 3.12 summarizes the results of the calibration studies when bundled according to beam line helicity.

The fluctuations seen in the calibrated sensitivities are likely due to small differences in beam tune arising after beam line helicity reversal. The different beam tunes can alter the particle distribution in the tails of the beam. These

Beam line +					
Run	$\Delta E(eV)$	$\omega(10^{-7}/eV)$	Run	$\Delta E(eV)$	$\omega(10^{-7}/eV)$
2638	0.47	50 ± 51	5970	-0.5	68 ± 16
2936	0.5	-217 ± 59	6007	-0.5	155 ± 21
2938	0.1	-79 ± 132	6145	-0.25	46 ± 25
2939	0.25	-414 ± 130	6146	-0.5	65 ± 13
3315	0.2	-70 ± 40	6184	-0.25	113 ± 37
3367	0.5	-35 ± 22	6185	-0.5	144 ± 28
3368	0.2	4 ± 50	6553	-1.0	26 ± 5
5602	-0.5	101 ± 18	6591	-1.0	18 ± 14
5732	-0.5	122 ± 16	7034	1.0	97 ± 12
5775	-0.5	58 ± 19	7036	1.0	75 ± 14
5782	-0.5	175 ± 22	7119	1.0	27 ± 11
5819	-0.5	129 ± 20	7171	1.0	20 ± 12
5836	-0.5	71 ± 15	7182	-1.0	49 ± 10
5845	-0.5	79 ± 15	7193	-1.0	38 ± 11
5967	-0.5	78 ± 42			

Table 3.10: *Sensitivities to ΔE (at OPPIS) in + beam line tune. Calibration runs 2638-3368 are conducted during the Feb97 data run, runs 5602-6185 are conducted during the Jul98 data run, the remainder of the runs are conducted during the May99 data run.*

Beam line −					
Run	$\Delta E(eV)$	$\omega(10^{-7}/eV)$	Run	$\Delta E(eV)$	$\omega(10^{-7}/eV)$
2836	0.48	-180 ± 54	6061	-0.5	-13 ± 16
2872	0.48	96 ± 69	6089	-0.5	110 ± 18
3034	0.2	27 ± 34	6229	-0.25	-41 ± 24
3035	0.1	-7 ± 77	6230	-0.5	3 ± 11
3040	0.1	190 ± 214	6259	-0.25	42 ± 21
3268	0.2	11 ± 34	6260	-0.5	9 ± 14
5666	-0.5	-63 ± 21	6304	-0.25	-29 ± 32
5679	-0.5	-43 ± 16	6714	1.0	-58 ± 11
5912	-0.5	-76 ± 15	6741	1.0	-3 ± 7
5935	-0.5	-55 ± 15	6901	1.0	-74 ± 14
5970	-0.5	-68 ± 16	7220	-1.0	5 ± 7
6007	-0.5	-155 ± 21	7221	-1.0	-3 ± 8
6024	-0.5	-114 ± 17	7262	-1.0	-68 ± 11

Table 3.11: *Sensitivities to ΔE (at OPPIS) in − beam line tune. Calibration runs 2836-3268 are conducted during the Feb97 data run, runs 5666-6304 are conducted during the Jul98 data run, the remainder of the runs are conducted during the May99 data run.*

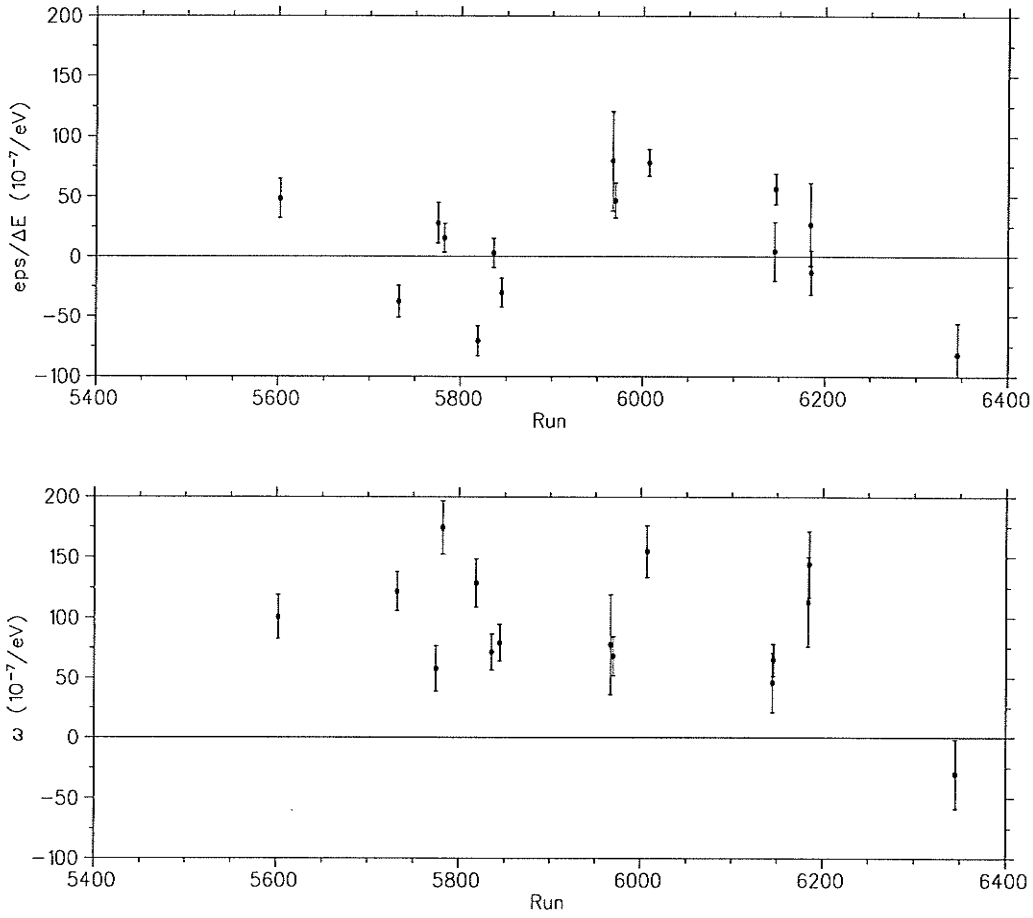

Figure 3.6: *The Jul98 energy modulation calibration in + beam line tune. The upper panel shows the raw calibration data eps* $= \Delta A_z$*; the lower panel shows the sensitivity,* ω*, after correcting the data for the effects of coherent intensity modulation. Immediately prior to run 6345 there were cyclotron instabilities. Following the run, the instabilities were so severe that data aquisition was discontinued for approximately three hours. This run was excluded from the final analysis. The weighted average of these data, excluding run 6345, is* $(89 \pm 11) \times 10^{-7}/eV$*. The reduced chi-squared of the fit is 3.8.*

Set	Beam line helicity	$A_z^{raw}(10^{-7}/eV)$	$\omega(10^{-7}/eV)$	χ^2_ν	d.o.f.
Feb97	(+,+)	-10 ± 32	-83 ± 58	4.6	4
Feb97	(−,−)	-66 ± 16	-29 ± 16	0.5	1
Jul98	+	12 ± 13	89 ± 11	3.8	13
May99	+	3 ± 14	38 ± 9	6.0	7
Feb97	(+,−)	-27 ± 40	9 ± 47	3.5	4
Feb97	(−,+)	8 ± 34	11 ± 34	N/A	0
Jul98	−	-30 ± 9	-39 ± 14	8.6	12
May99	−	-10 ± 13	-17 ± 14	14	5

Table 3.12: *Calibrated sensitivities to intrinsic energy modulation. The energy modulation calibration runs are bundled according to beam line helicity and data run after the individual calibration runs are linearly fit against systematic intensity modulation.*

differences in the tails are undetectable by the IPMs and are therefore very difficult to monitor, control, or replicate but may contribute to asymmetries measured at the TRICs.

The cyclotron is also known to have an amplification factor of intrinsic beam energy modulations of between 100-200. The amplification factor was measured during an engineering run in beam line $4B$ at TRIUMF, and was found to vary considerably with changing conditions in the cyclotron. Qualitatively, however, the results of the energy modulation calibration study are encouraging. It has been determined previously that the sensitivity (at the target) due to coherent energy modulations in the beam line is $(0.29 \pm 0.03) \times 10^{-7}/eV$ [2]. The values in Table 3.12 above show an average sensitivity, $|\omega|$, of approximately $40 \times 10^{-7}/eV$, which corresponds to an average cyclotron amplification factor of 130, in agreement with previous measurements.

In addition to the calibration runs, 62 measurements of the intrinsic energy

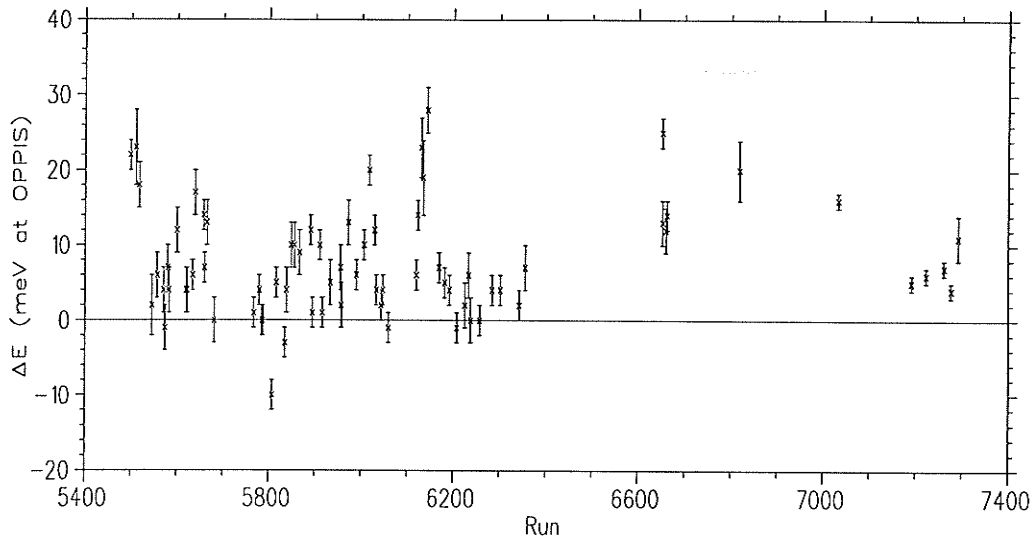

Figure 3.7: *Measured ΔE (at OPPIS) during the Jul98 and May99 runs. Runs after run 6600 were measured during the May99 data run. The measurements taken during Jul98 include approximately 6-12 meV of energy modulation compensation. The result of the compensation is a smaller intrinsic energy modulation at the source during the Jul98 data run. The average ΔE is (7 ± 4) meV during the Jul98 data run and (15 ± 5) meV during the May99 data run. Coherent energy modulation at OPPIS has been estimated at 5-15 meV for the Feb97 run.*

modulation, ΔE, at OPPIS were taken during the Jul98 data run and 11 during the May99 data run. Figure 3.7 shows the data graphically. Using these data, an effective energy modulation ΔE can be calculated.

Almost all of the regular parity data acquired during the Jul98 data run is subject to 6-12 meV of energy modulation compensation. No compensation is applied to any of the Feb97 or May99 runs that are included in this analysis.

The average ΔE are shown in Table 3.13. The final instrumentation needed to conduct measurements of ΔE was not in place at the commencement of the Feb97 data run. However, a prototype ΔE monitor was in place which allowed parity collaborators to measure the combined effect of beam position

and energy modulation using a single-arm spectrometer at the ion source. Considering the combined effect of these two systematic modulations, which were analyzed offline, and results from measurements using the energy modulation spectrometer (once it was in place), an estimate of ΔE at OPPIS during the Feb97 data run was made at (10 ± 5) meV [32].

Set	ΔE (meV at source)
Feb97	10 ± 5
Jul98	7 ± 4
May99	15 ± 5

Table 3.13: *Measured coherent energy modulation at OPPIS.*

Systematic uncertainty due to ΔE

It is expected that ΔE intrinsically produced at the source will not change sign, or magnitude, as a function of beam line tune. Therefore, false asymmetry due to ΔE in $+$ and $-$ beam line tune may cancel in the measurement of A_z, provided an equal amount of parity data is acquired in both beam line tunes and the effect of the modulation at the target is constant.

Acquiring equal statistics was one of the objectives during data acquisition, however, due to offline data quality cuts, the reduced grand set contains slightly more data with a $-$ beam line tune. As a result, an estimate of the systematic error in each beam line state must be weighted by the fraction of data acquired in the beam line tune. A magnitude estimate of the systematic error produced by energy modulation is calculated by using ΔE and the sensitivities using equation 3.2.

Table 3.14 shows an estimate of the false effect of coherent energy modulation during the three data runs based on the measurements of ΔE and the sensitivities ω. The Feb97 data run calculation includes the estimate of

$\Delta E = (10 \pm 5)\ meV$. Effective sensitivities for each Wien filter/beam line configuration are calculated by scaling ω by the fraction of event pairs in the data run measured in the configuration. The uncertainty in the false analyzing power estimated for each data run is a quadrature sum of the relative uncertainty in the measurements of ΔE and the effective sensitivity.

Feb97		
$\Delta E = (0.010 \pm 0.005)$ eV		
(WF,BL)	Fraction of event pairs	Eff. sensitivity $(10^{-7}/eV)$
(+,+)	0.31	$0.31(-83 \pm 58)$
(+,−)	0.33	$0.33(9 \pm 47)$
(−,+)	0.20	$0.20(11 \pm 34)$
(−,−)	0.16	$0.16(-29 \pm 16)$
Total	1.00	-25 ± 24
$\Delta A_z = (0.010 \pm 0.005) \times (-25 \pm 24) \times 10^{-7} = (-0.25 \pm 0.27) \times 10^{-7}$		

Jul98		
$\Delta E = (0.007 \pm 0.004)$ eV		
Beam line	Fraction of event pairs	Eff. sensitivity $(10^{-7}/eV)$
+	0.48	$0.48(89 \pm 11)$
−	0.52	$0.52(-39 \pm 14)$
Total	1.00	22 ± 7
$\Delta A_z = (0.007 \pm 0.004) \times (22 \pm 7) \times 10^{-7} = (0.16 \pm 0.10) \times 10^{-7}$		

May99		
$\Delta E = (0.015 \pm 0.005)$ eV		
Beam line	Fraction of event pairs	Eff. sensitivity $(10^{-7}/eV)$
+	0.43	$0.43(38 \pm 9)$
−	0.57	$0.57(-17 \pm 14)$
Total	1.00	6.6 ± 8.9
$\Delta A_z = (0.015 \pm 0.005) \times (7 \pm 9) \times 10^{-7} = (0.09 \pm 0.12) \times 10^{-7}$		

Table 3.14: *Estimate of systematic error due to* ΔE.

Table 3.15 shows an estimate of the false effect of coherent energy modulation in the grand set. It was found that attempting a correction for the systematic effect of coherent energy modulation on a set by set basis increased the spread of corrected A_z values. This occurs because of the cancellation of the systematic effect in opposing beam line helicities. The reduction in the overall systematic uncertainty due to the cancellation of the effect, disproportionately decreases the systematic uncertainty in the corrections when applied on a set by set basis: the result being an increase in the χ^2_ν of the A_z distribution. For this reason and the fact that the net shift due to ΔE was found to be zero, no systematic error correction is made for the effect: however, the uncertainty in the correction is added in quadrature to the total systematic error in the final result (see section 3.6.5).

Data run	$\Delta A_z(10^{-7})$
Feb97	-0.25 ± 0.27
Jul98	0.16 ± 0.10
May99	0.09 ± 0.12
Average	0.00 ± 0.11

Table 3.15: *Estimate of total ΔA_z due to helicity-correlated energy modulation at OPPIS. The estimate of a net systematic shift in A_z is zero for the effect of intrinsic energy modulation; however, the uncertainty in this estimate is added in quadrature to the uncertainty in the final result (see section 3.6.5).*

3.4.2 Beam parameter modulation calibration in $4A/2$

Using the steering magnets and beam line assembly to induce correlated modulations of the beam size, beam position, and extrinsic moments of polarization allows for a systematic study of the effect of these types of coherent modulations which occur during real parity data-taking. The calibration data are

bundled according to 100 event pairs and regression analysis is performed on the data to find the sensitivity of the apparatus to amplified modulations of each of the beam parameters. There are three types of direct calibration studies performed during regular data-taking. They are studies of the effect of helicity-correlated beam position, beam size, and transverse polarization components.

Neutral axis scans

The polarization neutral axis is, by definition, a symmetry axis through the parity apparatus. The apparatus is insensitive to transverse polarization components on the neutral axis.

It is important to determine empirically where the neutral axis is at the start of each major data run and to lock the beam in place accordingly with the position feedback loops. Three neutral axis scans were conducted during each major data run. Unfortunately, during each data run, one of the three neutral axis scans contained a considerable number of spurious events making analysis of those particular scans very difficult. The remaining two neutral axis scans during each major data run were combined, and the sensitivities $\{a_1, ..., b_3\}$ of equation 2.19 were determined by regression analysis. The results are shown below in Table 3.16. Note the agreement of the (a_1, a_2, b_1, b_2) parameter sensitivities across the three major data runs. The a_3 and b_3 sensitivities are overall position offsets that change when the monitor is removed from the beam line for servicing and/or replaced.

It will be seen that using the results of the extrinsic sensitivities, the net systematic effect of transverse components on the measured A_z—in the final analysis of the grand set—is predicted to be consistent with zero at the 10^{-9} level. This suggests that the polarized beam during all three major data runs travelled sufficiently close to the neutral axis.

Sensitivity (10^{-7})	Feb97	Jul98	May99
$a_1(mm^{-1})$	$1,907 \pm 26$	$1,847 \pm 13$	$1,833 \pm 18$
$a_2(mm^{-1})$	$-2,467 \pm 8$	$-2,469 \pm 7$	$-2,435 \pm 10$
a_3	-549 ± 5	$-1,149 \pm 7$	-263 ± 7
$b_1(mm^{-1})$	$-1,505 \pm 32$	$-1,493 \pm 11$	$-1,490 \pm 16$
$b_2(mm^{-1})$	$2,016 \pm 43$	$1,995 \pm 6$	$1,981 \pm 12$
b_3	1314 ± 28	-354 ± 6	497 ± 8
bundlesize	100	100	100
χ^2_ν	1.17	1.96	2.05
d.o.f.	391	399	313

Table 3.16: *Fitted sensitivities to the neutral axis scans.*

Figure 3.8 shows two graphs of the results of the analysis of the Feb97 study. The left graph displays measured A_z as a function of the predicted effect of extrinsic moments as determined from the parameter sensitivities. The right graph displays the residual from a straight line. Both graphs are a function of the 18 calibration runs taken during the Feb97 data run and show the P_x and P_y calibration scans together.

The calibration data were reduced by placing 3σ cuts on position and current, and 198-202 nA hard cuts on intensity. Manual hard cuts on IPM data were unnecessary to complete the calibration. The position data were projected to the PPMs, and the statistical uncertainties of the fit parameters were multiplied by the square root of χ^2_ν. This was done to account for the additional variation in the fitted results that was not entirely accounted for by the assigned statistical errors.

Various regression fits were attempted according to a variety of bundlesizes, but no dependence on bundlesize of the parameter sensitivities was observed. A bundlesize of 100 event pairs was chosen to represent the results of the study. The following two sections present the results of the beam position and size

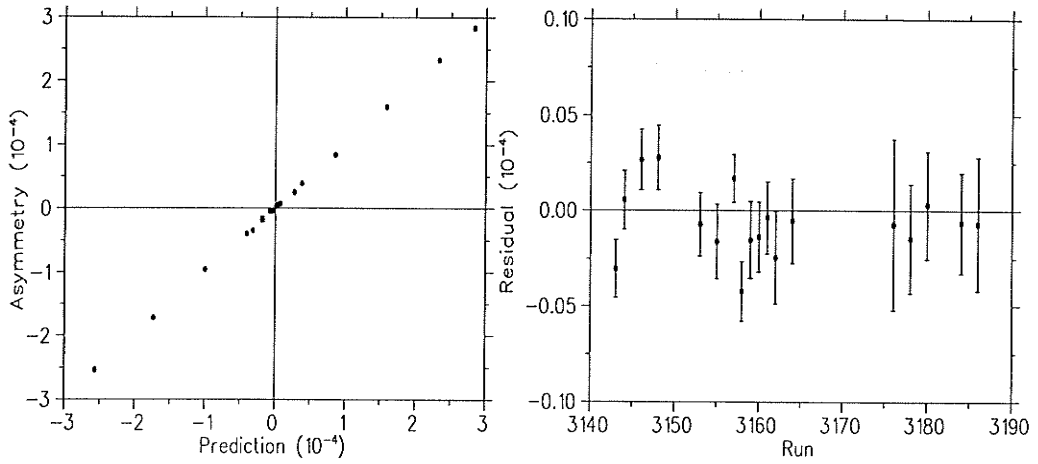

Figure 3.8: *(left) A_z as a function of the predicted false asymmetry based on the results of the calibration, and (right) the fit residuals as a function of calibration run number for the Feb97 neutral axis scans. The P_x and P_y scans are shown together.*

modulation studies conducted during the major data runs. These studies are performed relative to the neutral axis as determined during online analysis of the neutral axis calibration scans.

Position modulation

During both Jul98 and May99 data runs, 30 calibration runs were taken to find the beam position modulation sensitivities (a_x, ..., f_y) of equation 2.25. Only 20 calibration runs were obtained during the Feb97 position modulation study. The fitted values for the position modulation sensitivities from each study are displayed in Table 3.17. The statistical uncertainties in the parameter sensitivities quoted in the table have been multiplied by the square root of χ^2_ν. As for the neutral axis scan data, this has been done to account for systematic variation of the parameter sensitivities due to other false effects which may have occurred during the calibration.

The Jul98 and May99 calibrations—both using IPM2 in fast feedback

Sensitivity (10^{-4})	Feb97 Value	Jul98 Value	May99 Value
$a_x(mm^{-2})$	1.7 ± 1.1	-7.6 ± 0.3	-9.2 ± 0.1
$b_x(mm^{-2})$	1.4 ± 1.2	10.4 ± 0.2	13.8 ± 0.2
$c_x(mm^{-1})$	5.2 ± 2.0	-1.7 ± 0.1	6.0 ± 0.1
$d_x(mm^{-2})$	-3.7 ± 1.7	45.6 ± 0.8	51.0 ± 0.5
$e_x(mm^{-2})$	-0.4 ± 1.8	-59.8 ± 0.7	-71.7 ± 0.7
$f_x(mm^{-1})$	-0.8 ± 3.1	8.1 ± 0.2	-25.6 ± 0.3
$a_y(mm^{-2})$	2.8 ± 0.3	2.0 ± 0.2	-4.1 ± 0.1
$b_y(mm^{-2})$	-1.7 ± 0.2	-1.2 ± 0.2	5.6 ± 0.1
$c_y(mm^{-1})$	-3.8 ± 0.1	10.6 ± 0.1	-3.5 ± 0.1
$d_y(mm^{-2})$	-6.6 ± 0.9	25.7 ± 0.8	26.5 ± 1.0
$e_y(mm^{-2})$	1.9 ± 1.2	-20.0 ± 0.7	-35.6 ± 0.8
$f_y(mm^{-1})$	26.7 ± 0.9	52.4 ± 0.6	80.8 ± 0.5
χ^2_ν	2.45	2.07	1.47
d.o.f.	216	449	523

Table 3.17: *Fitted sensitivities to the beam position modulation calibration scans. The results from the Feb97 scan have been projected to the position of IPM2 for comparison with the results of the other two scans.*

mode—produced qualitatively similar results. The discrepancy is likely due to the fact the two scans were locked on a different neutral axis and the beam position sensitivity of the apparatus is slightly different in the vicinity of these two different axes. For purposes of comparison with Jul98 and May99, the Feb97 sensitivities are projected to the positions of IPM1 and IPM2 in Table 3.17.

Sensitivities determined from the Feb97 scan show much larger statistical uncertainty as well as smaller values of the sensitivities. This was due to the instability of the position signals and feedback loop which was symptomatic of the Feb97 data run. In addition, the Feb97 calibration did not examine the full parameter space that the Jul98 and May99 studies explored. It will be

seen in section 3.6.5 that the net correction applied to the final data set for the systematic effect of beam position modulation is consistent with zero.

All of the calibration data were reduced by applying 3σ cuts on average positions and 198-202 nA hard cuts on intensity. All calibration runs were investigated for evidence of beam excursions in the position data. There were some spurious events found, and these were removed by hand.

Figure 3.9 shows two graphs of the results of the analysis of the May99 beam position study. The left graph displays measured A_z as a function of the predicted effect of position modulation as determined from the parameter sensitivities. The right graph displays the residual from a straight line. Both graphs are a function of the 30 position modulation runs taken during the study.

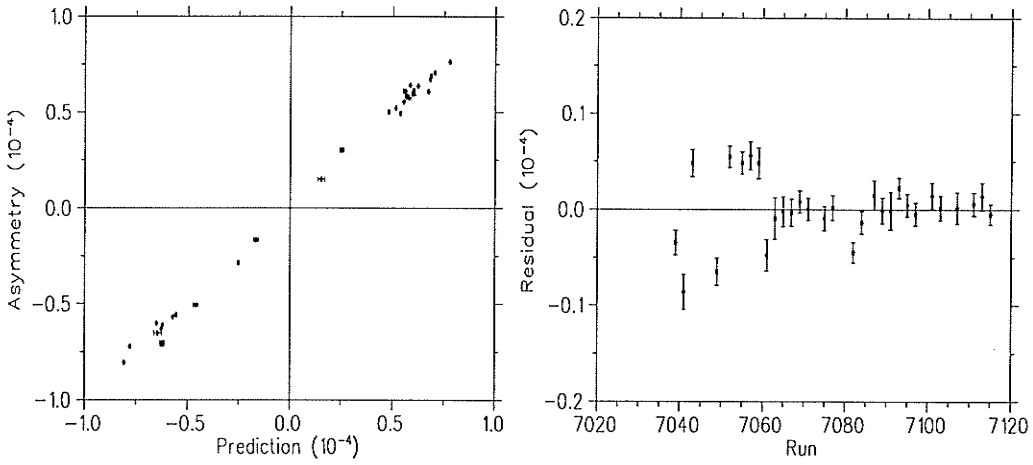

Figure 3.9: *(left) A_z as a function of the predicted false asymmetry based on the results of the beam position modulation calibration, and (right) the fit residuals as a function of run number for the May99 beam position modulation study.*

Size modulation

A total of 81 calibration runs were conducted to determine the beam size modulation sensitivities ($\alpha_x, .., \beta_y$) of equation 2.28. The calibration data were

reduced by placing 3σ cuts on average positions and 198-202 nA hard cuts on intensity. During the beam size modulation calibration, the position feedback loops must be turned off in order to artificially enhance coherent size modulations. As a result, the beam position is unstable and both beam position and size modulation must be fit simultaneously. The results of the May99 calibration study are shown in Figure 3.10.

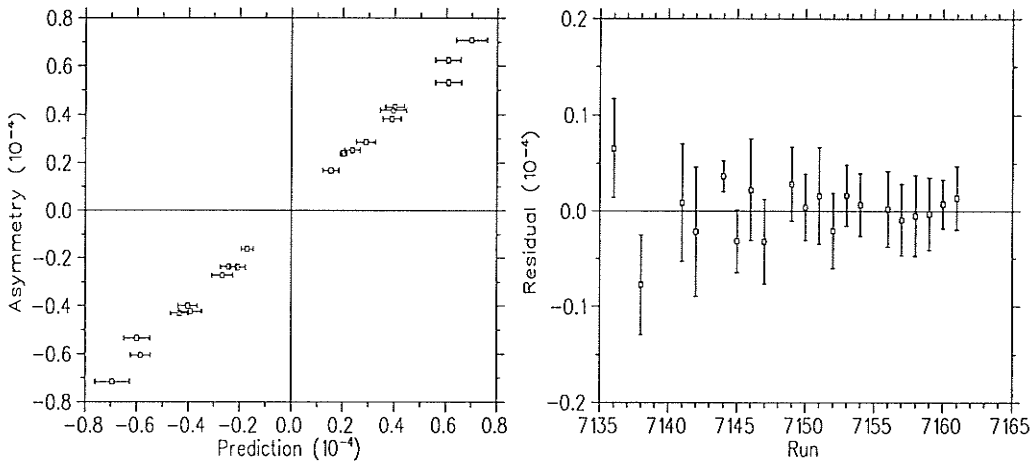

Figure 3.10: *(left) A_z as a function of the predicted false asymmetry based on the results of the beam size modulation calibration, and (right) the fit residuals as a function of run number for the May99 beam size modulation study.*

The beam size calibration studies also demonstrate a strong dependence of the parameter sensitivities on the bundle size used in the fitting routine. The sensitivities determined from the calibration data are, for these reasons, too unreliable to correct $A_z^{reduced}$ for coherent beam size modulation. Instead, the real parity data must be regressed to determine the sensitivity of the parity apparatus to coherent beam size modulation. Table 3.18 displays the findings by direct regression of $A_z^{reduced}$ to coherent beam size modulations. The final column of the table includes the results from the May99 external calibration study. When the external sensitivities were used to correct the parity data during the analysis of the May99 data set, the agreement of the A_z measurements was significantly worsened. This supports the conclusion

that the external calibration sensitivities are not appropriate to describe the sensitivity of the parity apparatus under normal running conditions.

Sensitivity	Feb97	Jul98 and May99	May99 ext. study
$\alpha_x(10^{-7}/mm^2)$	-88 ± 40	285 ± 90	$-3,290 \pm 130$
$\beta_x(10^{-7}/mm^2)$	5 ± 17	$1,004 \pm 103$	$5,910 \pm 360$
$\alpha_y(10^{-7}/mm^2)$	24 ± 42	-290 ± 91	$3,670 \pm 140$
$\beta_y(10^{-7}/mm^2)$	5 ± 19	$-2,388 \pm 156$	$-9,950 \pm 550$
χ^2_ν	1.08	1.00	1.35
bundlesize	100	100	20
d.o.f.	9,575	17,613	1,418

Table 3.18: *Regressed sensitivities to helicity-correlated beam size modulation. The final column includes the results of the May99 external calibration study.*

It is seen that for the combined Jul98 and May99 result, the long lever arm associated with the positioning of IPM1 and IPM2 contributes to a larger absolute uncertainty in the sensitivities in relation to the results of the Feb97 data run regression. However, the relative errors in the parameter sensitivities are much smaller than for the Feb97 data.

3.5 Sensitivity to intrinsic first moments

The largest contributor to a false asymmetry in the grand set is expected to be due to the systematic effect of intrinsic first moments of polarization. The intrinsic moments are difficult to control and measure. Unfortunately, the sensitivity of the parity apparatus leads to relatively large corrections to A_z with typical polarization moments measured during regular data taking. While the sensitivity to intrinsic moments is, in principle, determined during the neutral axis scans, application of the corrections leads to large statistical uncertainty in the false asymmetry due to the limited precision of the PPMs.

An improved statistical error on the correction is obtained by determining the sensitivities from regression analysis applied to the full parity data sample. However, in this case it is assumed that the sensitivities are constant. Since the sensitivity is strongly dependent on beam tune, as noted in the previous chapter, it is extremely important to maintain a consistent beam line tune throughout a data run. There are three techniques to determine the first moment sensitivity explored in this analysis: the extrinsic method, the ratio method, and direct first moment regression, as discussed below.

3.5.1 Extrinsic method

The extrinsic method makes use of the sensitivities found from analyzing the neutral axis scans to calculate and correct for the effect of intrinsic first moments. Using extrinsic moment sensitivities, the false asymmetry due to intrinsic first moments of polarization can be expressed as

$$\Delta A_z = a_1\langle yP_x\rangle_1 + a_2\langle yP_x\rangle_2 + b_1\langle xP_y\rangle_1 + b_2\langle xP_y\rangle_2, \tag{3.5}$$

where (a_1, a_2, b_1, b_2) are determined from the neutral axis scans. The tabulated values of the sensitivities are shown in section 3.4.2. Figure 3.11 shows A_z^{corr} as a function of set using the extrinsic moment sensitivities. The data shown in the figure are also corrected for the systematic effects of coherent beam intensity modulation and extrinsic moments of polarization.

The disadvantage to using the extrinsic method is the large statistical variation that the method introduces to the correction ΔA_z. In the final analysis, this technique is not used to correct $A_z^{reduced}$ because of the large statistical error in the measurement of the intrinsic moments.

A considerable amount of effort was spent during the earlier stages of the experiment developing improved ways to correct for the effect of intrinsic moments [2]. An improved technique, called the "ratio method" combines the

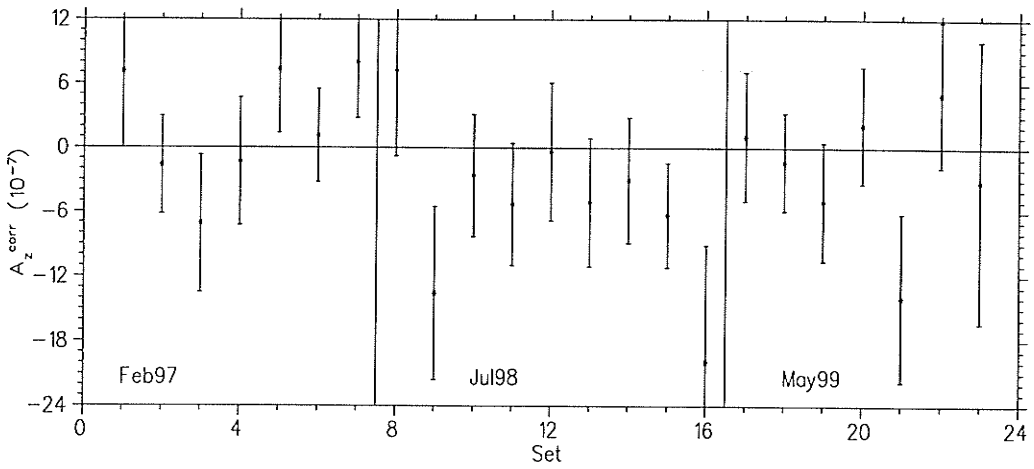

Figure 3.11: A_z^{corr} *as a function of set using the extrinsic moment sensitivities to correct for the effect of intrinsic moments. The weighted average of* A_z^{corr}*, measured in units of* 10^{-7}*, for the 23 sets is* $-2.56 \pm 1.23(stat.)$*. The reduced chi-squared of the 23 sets is 1.11. The data are also corrected for the systematic effect of coherent beam intensity modulation and extrinsic moments of polarization.*

extrinsic sensitivities with knowledge of the beam convergence in order to derive effective first moment sensitivities. The results of the ratio method are presented in the following section.

3.5.2 Ratio method

The ratio method of first moment correction exploits knowledge of the beam convergence along $4A/2$ to determine an effective sensitivity to intrinsic moments. This is done by assuming that intrinsic first moments of polarization vary linearly with position along the beam line in the region of the parity apparatus. Recall from section 2.6.2 that the intrinsic moments at PPM2 are

related to the moments at PPM1 by the ratios

$$R_y = \frac{\langle yP_x \rangle_2}{\langle yP_x \rangle_1} \; and \; R_x = \frac{\langle xP_y \rangle_2}{\langle xP_y \rangle_1}.$$

The correction to $A_z^{reduced}$ is then expressed as:

$$\begin{aligned} \Delta A_z &= \left(\frac{1}{1+R_y}\right)(a_1 + R_y a_2)(\langle yP_x \rangle_1 + \langle yP_x \rangle_2) \\ &+ \left(\frac{1}{1+R_x}\right)(b_1 + R_x b_2)(\langle xP_y \rangle_1 + \langle xP_y \rangle_2) \\ &= h_a(\langle yP_x \rangle_1 + \langle yP_x \rangle_2) + h_b(\langle xP_y \rangle_1 + \langle xP_y \rangle_2) \\ &= h_a\langle yP_x \rangle + h_b\langle xP_y \rangle, \end{aligned} \tag{3.6}$$

where $\langle yP_x \rangle$ and $\langle xP_y \rangle$ are the sum of the averaged intrinsic first moments measured at the two PPMs.

A regression routine applied to the PPM data determines the ratios R_y and R_x by examining the correlation between moments at each PPM. A chi-squared minimization is performed during the regression analysis using the software package MINUIT [33]. The effective sensitivities are then calculated according to equation 3.6 using R_y, R_x, and the sensitivities (a_1, a_2, b_1, b_2) determined from the neutral axis scans. Figure 3.12 shows A_z^{corr} as a function of set using the effective first moment sensitivities h_a and h_b. The figure shows the corrected A_z on a smaller scale as for Figure 3.11. The data shown in the figure are also corrected for the systematic effects of coherent beam intensity modulation and extrinsic moments of polarization.

It will be shown below that a direct regression of $A_z^{reduced}$ on intrinsic moments determines more accurate sensitivities to the intrinsic moments. Therefore, the sensitivities calculated by the ratio technique are not used to correct $A_z^{reduced}$ in the final analysis. However, the corrected A_z value based on the results of the ratio method is in very good agreement with a direct regression

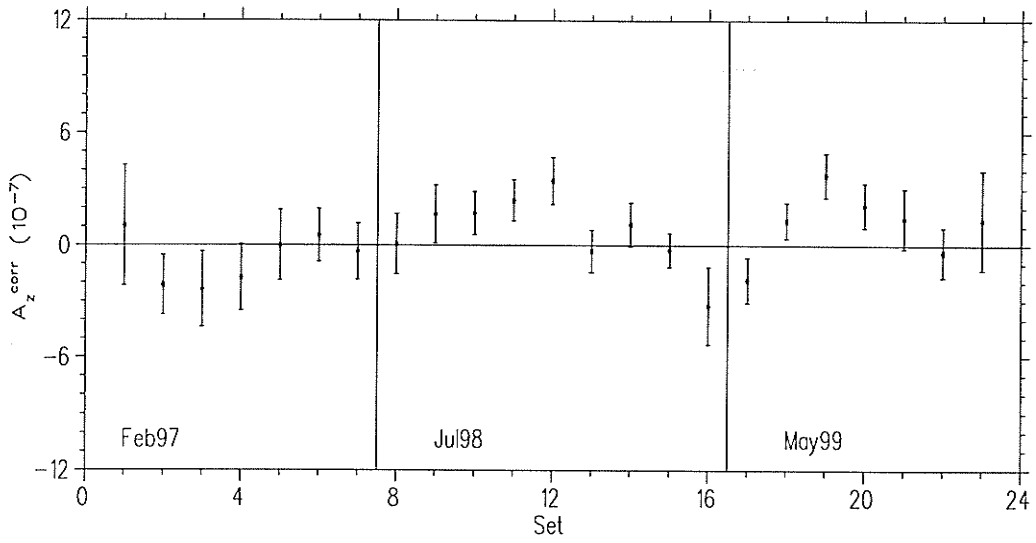

Figure 3.12: A_z^{corr} *as a function of set using the effective sensitivities* h_a *and* h_b *to correct for the effect of intrinsic moments. The weighted average of* A_z^{corr}*, measured in units of* 10^{-7}*, for the 23 sets is* $0.89 \pm 0.33(stat.)$*. The reduced chi-squared of the 23 sets is 1.43. The data are also corrected for the systematic effects of coherent beam intensity modulation and extrinsic moments of polarization.*

of the parity data to intrinsic first moments. The following subsection will present the results of the direct regression method.

3.5.3 Direct first moment regression using *MINUIT*

The most straightforward regression method available for the analysis of parity data is a direct regression of $A_z^{reduced}$ to the intrinsic first moments. The chi-squared minimization package, MINUIT [33], is used to determine the sensitivities of the parity apparatus to intrinsic moments. The false asymmetry due to intrinsic moments is given by:

$$\Delta A_z \;=\; g_a\langle yP_x\rangle + g_b\langle xP_y\rangle \tag{3.7}$$

Figure 3.13 displays the bundlesize dependence of the regressed first mo-

ment sensitivity for the May99 data run. It is seen that g_a and g_b are independent of the bundlesize used in the regression for bundlesizes greater than about 1,000 event pairs. The Feb97 and Jul98 data runs show similar vanishing bundlesize dependence for bundlesizes greater than 2,000-3,000 event pairs. The following section summarizes the results of the intrinsic first moments regression of the grand set.

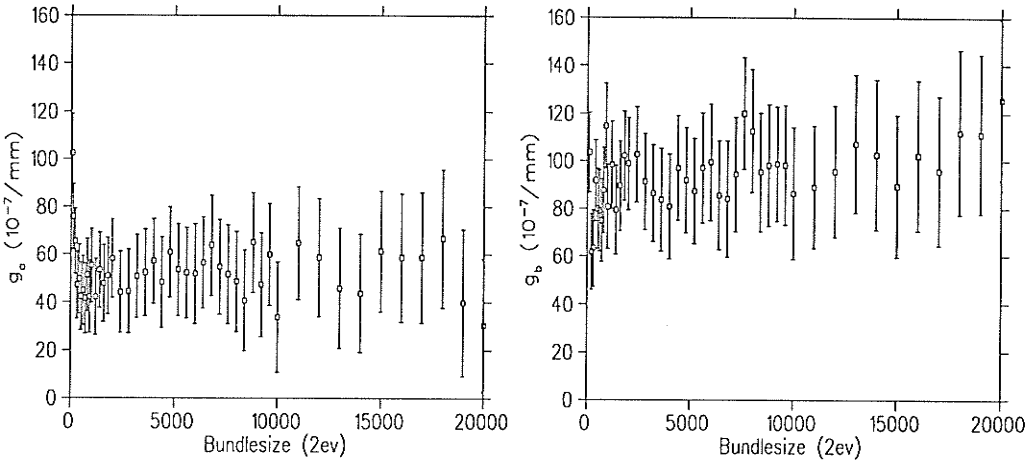

Figure 3.13: *Bundlesize dependence of first moment sensitivity during the May99 data run. The sensitivities do not display dependence to bundlesizes greater than 1000 event pairs.*

3.5.4 Summary of first moment sensitivities

Sensitivities to first moments for all three parity runs were determined using the direct regression technique described above. Table 3.19 summarizes the results of the regression.

Sets 1-7 were regressed according to a bundlesize of 5,000 event pairs. The eighth set acquired during the Feb97 data run (labelled as "Feb97 Set 8" in the table) was acquired in a different beam line tune and is seen to have a significantly different sensitivity to intrinsic first moments as compared to sets 1-7. For this reason, Feb97 Set 8 has been removed from the grand set. A

Set	$g_a(10^{-7}/mm)$	$g_b(10^{-7}/mm)$	Bundlesize (2ev)	χ^2_ν
1-7	90 ± 66	-167 ± 24	5,000	1.06
8-16	-62 ± 15	-6 ± 21	5,000	1.56
Jul98 +	-32 ± 29	10 ± 38	5,000	1.47
Jul98 −	-90 ± 18	-41 ± 30	5,000	1.52
17-23	24 ± 28	102 ± 36	1,800	1.00
Feb97 Set 8	118 ± 60	-17 ± 37	5,000	1.02

Table 3.19: *Sensitivities to intrinsic first moments. The sensitivities determined for Feb97 Set 8 appear to disagree with the first seven sets of the Feb97 data run. The g_a sensitivities corresponding to Sets 1-7 and 17-23 were modified from the MINUIT findings in the final analysis using a "do-it-yourself" chi-squared minimization technique described in reference [34].*

bundlesize of 5,000 event pairs was also used for the analysis of the intrinsic moment sensitivities during the Jul98 data run. However, a consistent sensitivity could not be determined for all of the Jul98 sets. As a result, systematic error corrections to the Jul98 data run are applied using different sensitivities according to beam line helicity. For the May99 data run, a bundlesize of 1,800 event pairs was used for the regression.

3.6 Corrected PNC analyzing power

3.6.1 Methodology of systematic error correction

Recall that one event pair produces one measurement of A_z and one measurement of many different helicity-correlated beam parameters. Consecutive spin-on events are bundled in sequence, and a mean and standard error are calculated for each parameter. The bundlesize, N, is chosen to be 10,000 event pairs (approximately 80 minutes of TRIC integration time). Most likely, a set

will contain a number of event pairs which can not be bundled into an integer number of bundles. So as not to exclude event pairs, a "runt" bundle is calculated at the end of each set. A runt bundle is a bundle containing the last $(\Gamma - N \times n_b)$ event pairs of a set, where Γ is the total number of event pairs in the set and n_b is the number of bundles in the set (excluding the runt bundle).

A weighted average is performed on all bundles in the grand set. The weighting function W, used in the calculation of the average for *all* parameters, is the inverse square statistical uncertainty of $A_z^{reduced}$ calculated for each bundle. If σ_i is defined as the standard error of the mean of the i^{th} bundle of $A_z^{reduced}$, then the weighting function for a data set containing $(n_b + 1)$ bundles is given by:

$$W = \left\{ \frac{\frac{1}{\sigma_1^2}}{\sum_{i=1}^{(n_b+1)} \frac{1}{\sigma_i^2}} , \cdots , \frac{\frac{1}{\sigma_{(n_b+1)}^2}}{\sum_{i=1}^{(n_b+1)} \frac{1}{\sigma_i^2}} \right\} . \tag{3.8}$$

All parameters are averaged using the same weighting function. Once the value of all parameters are determined, estimates of a false analyzing power are calculated.

The false analyzing power produced by coherent modulations of n beam parameters is given by

$$\Delta A_z = \sum_{i=1}^{n} \alpha^i \times \Delta\zeta_i \equiv \alpha^i \Delta\zeta_i \, , \tag{3.9}$$

where α^i is the sensitivity of the parity apparatus to helicity-correlated parameter $\Delta\zeta_i$. Thus, the corrected analyzing power is

$$A_z^{corr} = A_z^{reduced} - \Delta A_z = A_z^{reduced} - \alpha^i \Delta\zeta_i \, . \tag{3.10}$$

Hereafter, estimates of the corrected analyzing power will be accompanied by a quadrature sum δA_z^{corr} of two contributions: $\delta A_z^{stat.}$ and $\delta A_z^{syst.}$ unless otherwise noted. The first error is the standard error in the mean of the

A_z^{corr} distribution. The second error is the sum of squares of the systematic uncertainties of the correction terms. Thus, for a data set containing $(n_b + 1)$ bundles,

$$\delta A_z^{stat.} = \sqrt{\frac{1}{\sum_{i=1}^{(n_b+1)} \frac{1}{(\sigma A_{z,i}^{corr})^2}}}, \tag{3.11}$$

$$\delta A_z^{syst.} = \sqrt{\sum_{i=1}^{n} (\Delta\alpha^i \times \Delta\zeta_i)^2} \tag{3.12}$$

and

$$\delta A_z = \sqrt{(\delta A_z^{stat.})^2 + (\delta A_z^{syst.})^2}, \tag{3.13}$$

where $\Delta\alpha^i$ is the systematic uncertainty in the estimate of α^i.

In spite of the conservative approach to the data reduction procedure, the distribution of the total systematic error correction ΔA_z still contained some anomalous data. It is possible that the spurious events in the correction distribution represent relatively large excursions of a unique combination of beam parameters. It is also possible that the large error corrections are introducing additional systematic error to the measurement of A_z. At the very least, the anomalously large corrections increase the overall statistical uncertainty of A_z^{corr}, and a soft 3σ cut was placed on the correction distribution. In the final analysis, event pairs are excluded which require an absolute total systematic error correction of greater than $3\sigma = 462 \times 10^{-7}$.

Figure 3.14 shows a logarithmic histogram plot of the set by set correction once 3σ cuts have been applied to the distribution of the total error correction. The 3σ cuts reduced the number of event pairs in the grand set by 517. All of the histograms in the plot are shown on the same scale. The first seven sets (Feb97) have significantly wider systematic error correction distributions than the rest of the sets. This is due to the process of projecting beam position and size measured at IPM3 to IPM2 and PPM2 as well as the overall instability of

the feedback loop during the Feb97 data run. The following sections present the final result of the parity experiment once systematic error corrections are applied to the reduced data set.

3.6.2 The grand set

Figure 3.15 compares A_z^{corr} to $A_z^{reduced}$ for the various methods of correcting for intrinsic first moments. The figure displays four graphs, all as a function of the 23 sets: from top to bottom they are $A_z^{reduced}$, A_z^{corr} using the extrinsic moment sensitivities, A_z^{corr} using the ratio method effective sensitivities, and, A_z^{corr} using the direct regression sensitivities. The extrinsic sensitivities method of correction introduces large statistical variation in the corrected sets and is not used to correct for intrinsic first moments in the final analysis. The ratio method and the direct regression method both produce extremely consistent predictions for A_z: $A_z = (0.95 \pm 0.35(stat.)) \times 10^{-7}, \chi^2_\nu = 1.43$ from the ratio method versus $A_z = (0.84 \pm 0.29(stat.)) \times 10^{-7}, \chi^2_\nu = 1.08$ from the direct regression sensitivities. The latter method produces a final result with lower reduced chi-squared and lower statistical uncertainty; therefore, the sensitivities found from direct regression of intrinsic first moments are used to correct the grand set for the systematic effect of intrinsic first moments.

Table 3.20 shows the result of applying systematic error corrections to the 23 sets. The corrections are applied at the end of each set and the averaged A_z^{corr} has been calculated by weighting each set result by W as defined by equation 3.8. The uncertainty of A_z^{corr} for each set is calculated using equation 3.13. The systematic uncertainty associated with applying error corrections to A_z^{corr} is summarized in the following two sections.

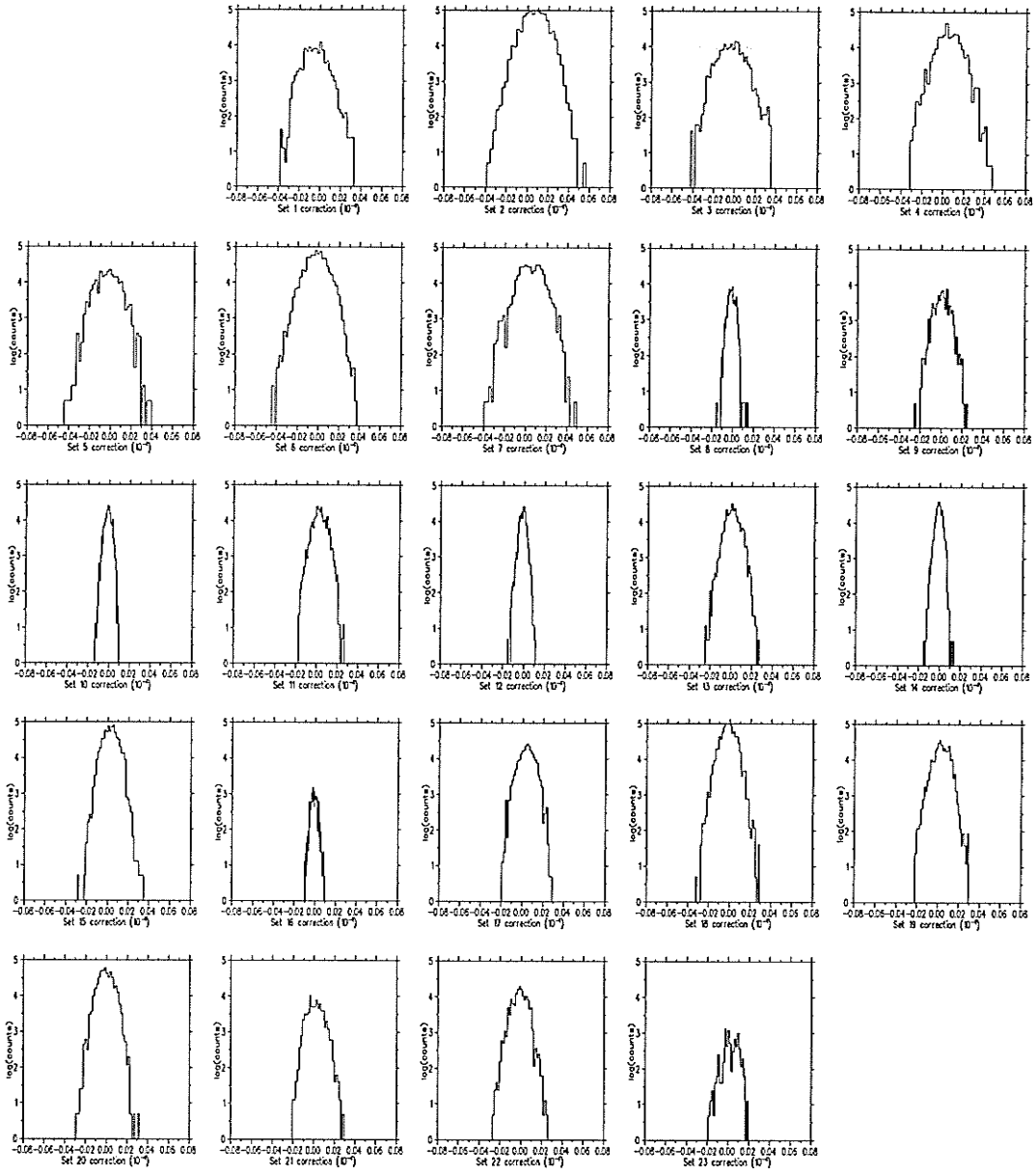

Figure 3.14: *Logarithmic histograms of the reduced total correction ΔA_z as a function of set. The distributions show the total correction once 3σ cuts on the total error correction distribution are applied. The total correction distribution has a standard deviation of $\sigma = 154 \times 10^{-7}$. Each event in the histograms are bundles of 100 event pairs. All of the histograms in the figure are plotted on the same scale. Refer to the text for an explanation of the increased width of the distributions from sets 1-7.*

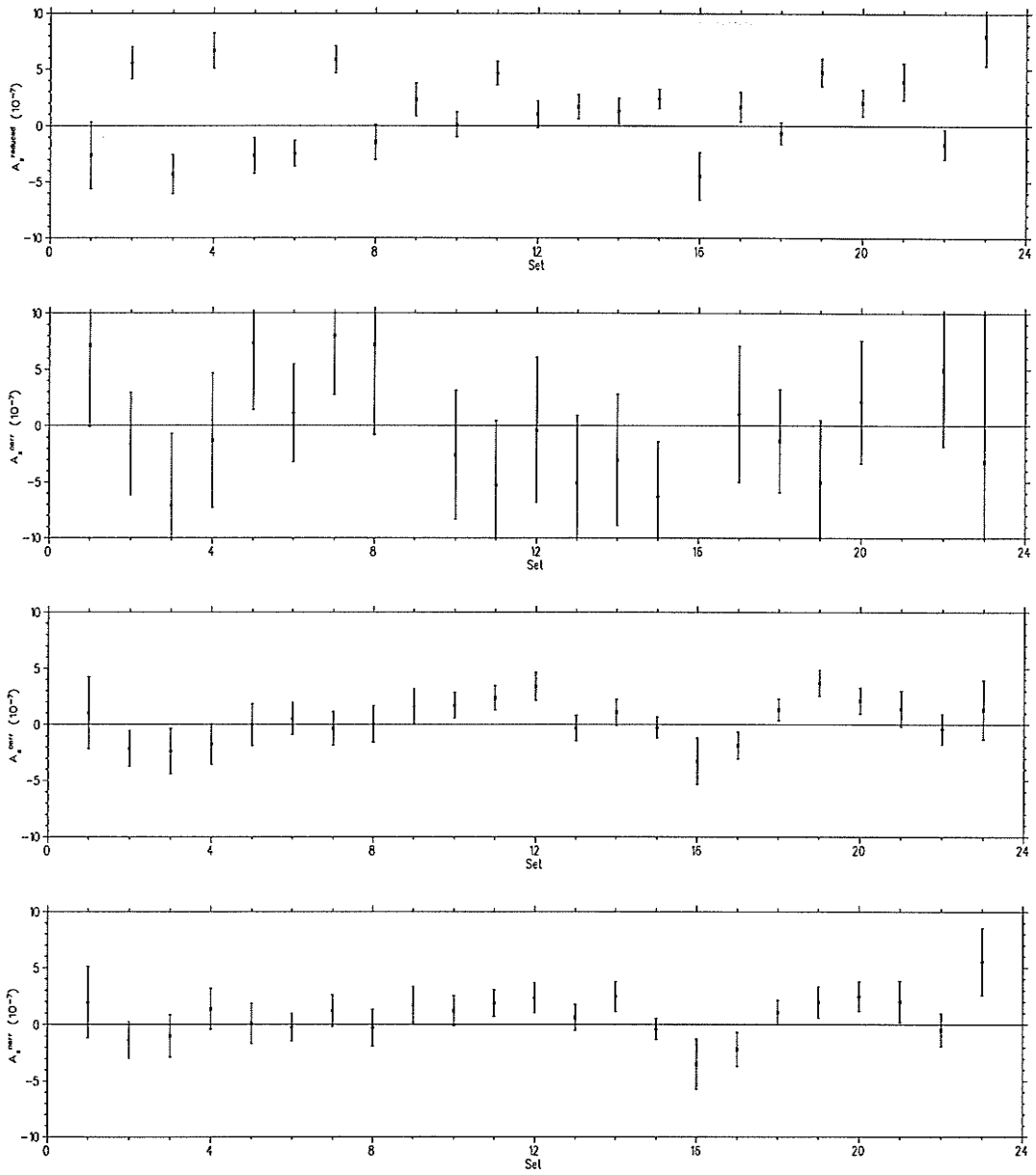

Figure 3.15: A_z^{corr} *as a function of set using the three methods of correction for intrinsic moments. From top to bottom:* $A_z^{reduced}$*, the corrected analyzing power via the extrinsic moment sensitivities, the corrected analyzing power via the ratio method, and the corrected analyzing power via direct first moment regression. In the extrinsic method graph, the corrected analyzing power for Set 9, 16 and 21 are below the y-axis scale.*

Set	$A_z^{reduced}(10^{-7})$	Event pairs	$A_z^{corr}(10^{-7})$
1	-2.62 ± 2.99	79,217	1.96 ± 3.14
2	5.58 ± 1.41	195,266	-1.35 ± 1.63
3	-4.31 ± 1.74	105,491	-1.01 ± 1.88
4	6.67 ± 1.55	117,731	1.40 ± 1.81
5	-2.65 ± 1.60	114,324	0.09 ± 1.77
6	-2.47 ± 1.14	193,908	-0.20 ± 1.25
7	5.90 ± 1.22	150,001	1.91 ± 1.18
8	-1.45 ± 1.56	66,653	-0.25 ± 1.64
9	2.35 ± 1.49	67,409	1.76 ± 1.62
10	0.14 ± 1.10	118,274	1.23 ± 1.33
11	4.67 ± 1.05	119,531	1.91 ± 1.18
12	1.04 ± 1.19	104,276	2.37 ± 1.33
13	1.70 ± 1.07	122,648	0.63 ± 1.15
14	1.32 ± 1.12	125,672	2.49 ± 1.31
15	2.41 ± 0.86	184,587	-0.39 ± 0.95
16	-4.50 ± 2.14	37,860	-3.49 ± 2.24
17	1.71 ± 1.32	115,246	-2.16 ± 1.53
18	-0.65 ± 0.97	221,423	1.09 ± 1.10
19	4.78 ± 1.24	139,631	1.98 ± 1.39
20	2.07 ± 1.18	147,932	2.48 ± 1.31
21	3.95 ± 1.64	70,026	2.03 ± 1.84
22	-1.65 ± 1.33	95,260	-0.45 ± 1.51
23	7.99 ± 2.65	24,469	5.55 ± 3.03
Average (χ^2_ν)	$1.58 \pm 0.27(stat.)$ (5.18)	2,716,835	$0.79 \pm 0.27(stat.)$ (1.08)
Feb97	$1.53 \pm 0.56(stat.)$ (10.7)	955,938	$0.13 \pm 0.58(stat.)$ (0.45)
Jul98	$1.58 \pm 0.39(stat.)$ (2.95)	946,910	$0.91 \pm 0.39(stat.)$ (1.25)
May99	$1.61 \pm 0.49(stat.)$ (4.33)	813,987	$1.08 \pm 0.50(stat.)$ (1.74)

Table 3.20: *Summary of sets of* A_z^{corr}.

3.6.3 Correction for longitudinal polarization P_z

By convention, during the NOVA reduction phase of the data analysis, the subtractor box output is assumed to be sampling a beam with 80% longitudinal polarization P_z. In fact, P_z is usually lower than 80% as inferred during the neutral axis scans. Thus, the final result for A_z must be rescaled by a polarization correction factor, η, as outlined below.

During regular data-taking, the solenoids precess the spin direction of the beam—which is in the vertical direction at the stripping foil—into the longitudinal direction. Vertical polarization of the beam is obtained by turning off the solenoids. The procedure is performed during the neutral axis scans so that the transverse polarization of the beam can be enhanced for the calibration scans and a measurement of the transverse polarization can be made. The longitudinal polarization can be inferred from the vertical polarization of the beam during the neutral axis scans by assuming P_y is equivalent to the longitudinal polarization, P_z, during regular data taking.

Table 3.21 summarizes the measurements of "P_z" taken during the neutral axis scans. Since the relative contribution to the total error in A_z arising from the limited measurements of P_y is small, a single overall scale factor, η, is used in the analysis. The correction factor to A_z^{corr} is given by:

$$\begin{aligned} A_z^{corr} &= \eta \times (A_z^{reduced} - \Delta A_z)\,, \\ \eta &= \tfrac{80}{75\pm1} = (1.067 \pm 0.014)\,. \end{aligned} \tag{3.14}$$

3.6.4 Correction for intrinsic energy modulation

The systematic error estimates for coherent energy modulation, calculated in section 3.4.1, can now be applied to A_z^{corr}. The result of applying the correction on a set by set, or beam line helicity basis, increased the reduced

Data run	P_y(%)	Date
Feb97	75	14 Feb 97
	77	20 Feb 97
	78	2 Mar 97
Jul98	76	23 Jul 98
	69	27 Jul 98
	71	18 Aug 98
May99	77	28 May 99
	70	31 May 99
	78	20 Jun 99
Average $P_y = (75 \pm 1)\%$		

Table 3.21: *Summary of measurements of the vertical polarization P_y [35] taken during the neutral axis scans. Each measurement has a systematic error of 1-2%. It is assumed during regular data taking that the longitudinal polarization, P_z, is equivalent to the above values.*

chi-squared of the twenty-three sets which suggests the systematic uncertainty in the calibration data is too large to allow corrections for this systematic error to be made on a set by set, or beam line helicity basis. Thus, *no correction is performed on the $A_z^{reduced}$ distribution for the systematic effect of coherent energy modulation.*

The estimate of a net systematic correction due to coherent energy modulation is $(0.00 \pm 0.12) \times 10^{-7}$, including the polarization scale factor η. For purposes of illustration, corrections for the systematic effect of energy modulation can be applied on the corrected results of the major data runs. It is seen that, on this scale, the energy modulation "correction" does improve data quality. Table 3.22 shows the result of applying a correction to the three major data runs for the systematic effect of coherent energy modulation. Not only does the correction shift the result of each corrected data run toward the grand

set average, but it also brings the results of all three individual data runs into statistical agreement. The data in the table have been adjusted to account for the P_z correction outlined above. Unfortunately, the energy modulation correction is not well enough determined to correct individual sets, and the systematic error due to ΔE can not be included in the calculation of reduced chi-squared of the 23 corrected sets.

Data run	$A_z^{corr}(10^{-7})$	$\Delta A_z(10^{-7})$	$A_z^{corr}(10^{-7})$ (incl. "correction")
Feb97	$0.14 \pm 0.62(stat.)$	-0.27 ± 0.29	0.41 ± 0.68
Jul98	$0.97 \pm 0.42(stat.)$	0.17 ± 0.11	0.80 ± 0.43
May99	$1.15 \pm 0.53(stat.)$	0.10 ± 0.13	1.05 ± 0.55

Table 3.22: *Applying a "correction" to A_z^{corr} for ΔE. The correction is applied to the data-run-averaged A_z^{corr} for purposes of illustration. The total uncertainty estimates shown in the table include the systematic error due to energy modulation added in quadrature to the statistical uncertainty of A_z^{corr}. The values in this table have been scaled by η.*

3.6.5 Summary of systematic error corrections

This section will summarize the systematic error corrections applied to $A_z^{reduced}$. In the final analysis, systematic error corrections to $A_z^{reduced}$ are applied for the systematic effects of coherent intensity modulation and extrinsic and intrinsic first moments of polarization. No corrections to $A_z^{reduced}$ are made for the systematic effects of coherent beam position, size, or energy modulation, as the net effects of these modulations are consistent with zero, and incorporating these corrections does not improve the data quality.

Coherent beam position and size modulation

An independent analysis was performed to search for correlations within the real parity data to coherent beam position and size modulations at the IPMs [36]. The result of the correlation analysis predicted a net shift of A_z consistent with zero. This result is also consistent with a systematic error calculation based on the beam position and size sensitivities determined from independent calibrations. Table 3.23 below compares the two predictions of the combined systematic effect of coherent beam position and size modulations in the measurement of A_z. Both predictions are consistent with each other, and the uncertainty associated with each analysis is statistics dominated due to the relatively large statistical uncertainty in the driving terms creating the false asymmetry.

Prediction based on calibrated sensitivities	Prediction based on correlation analysis
$0.0 \pm 0.09(stat.) \pm 0.03(syst.)$	0.0 ± 0.11

Table 3.23: *Comparison of predicted systematic effects of combined coherent beam position and size modulations in the grand set. All values in the table are in units of* 10^{-7}.

In the final analysis, the result based on the calibration sensitivities is used to estimate a systematic uncertainty in the measurement of A_z. The statistical and systematic uncertainties in the net correction are added in quadrature and the result is scaled by the number of event pairs in each of the 23 corrected sets. The scaled error, which is statistics dominated, is added in quadrature to the calculated systematic uncertainty due to other error corrections for each set. No correction is applied to the grand set; however, the uncertainty in each corrected set is increased slightly to account for the statistical variation of the helicity-correlated beam position and size parameters, and is thus accounted

for in the calculation of χ^2_ν for the grand set.

Regressing the grand set

Analyzing the corrected grand set for a sensitivity to the beam parameters used in the process of systematic error correction is an alternative method to check for any residual dependence of A_z^{corr} on coherent beam parameters. This procedure found no significant residual systematic error in the corrected data. The systematic uncertainties in the regressed sensitivities are multiplied by the corresponding helicity-correlated beam parameters (averaged over the entire grand set), then added in quadrature to estimate a systematic uncertainty in the calculation of A_z^{corr}. Table 3.24 shows the regressed residual sensitivities of A_z^{corr} to the three non-zero contributors to ΔA_z. All are consistent with zero.

Table 3.25 displays the various corrections to the analyzing power due to coherent modulations of measured beam properties. The average values of the properties are calculated using the same weighting function as for $A_z^{reduced}$. The statistical error on A_z^{corr} is calculated from the statistical spread of the corrected analyzing power and therefore takes correlations between correction parameters into account. The systematic error estimates shown in the table are based on sensitivities obtained through regression analysis of the corrected grand set.

Property	Sensitivity (10^{-7})
$\langle yP_x \rangle$	$(4 \pm 10)\ mm^{-1}$
$\langle xP_y \rangle$	$(17 \pm 29)\ mm^{-1}$
$\Delta I/I$	$(-12 \pm 13)\ \%^{-1}$

Table 3.24: *Summary of regressed "residual" sensitivities to* A_z^{corr}.

Property	Average Value	$\Delta A_z(10^{-7})$
$A_z^{reduced}(10^{-7})$	$1.68 \pm 0.29(stat.)$	
$y * P_x(\mu m)$	-0.1 ± 0.0	-0.01 ± 0.01
$x * P_y(\mu m)$	-0.1 ± 0.0	0.01 ± 0.03
$\langle yP_x \rangle(\mu m)$	1.1 ± 0.4	0.11 ± 0.01
$\langle xP_y \rangle(\mu m)$	-2.1 ± 0.4	0.54 ± 0.06
$\Delta I/I(ppm)$	15 ± 1	0.19 ± 0.02
$\Delta + \Delta\sigma$		0 ± 0.10
$\Delta E(meV at OPPIS)$	7–15	0.0 ± 0.12
Total		$0.84 \pm 0.17(syst.)$
$A_z^{corr}(10^{-7})$	$0.84 \pm 0.29(stat.) \pm 0.17(syst.)$	
$\chi^2_\nu(23sets)$	1.08	

Table 3.25: *Summary of helicity-correlated beam properties and systematic error corrections to* $A_z^{reduced}$. $A_z^{reduced}$, A_z^{corr}, *and all of the* ΔA_z *values have been muliplied by* η *to account for the* P_z *correction described above. The* $\Delta + \Delta\sigma$ *term represents the estimated total systematic effect of coherent position and size modulations.*

3.6.6 Final result

An important validation of the systematic error correction techniques is provided by comparing A_z^{corr} under the reversal of the beam line helicity tune. As discussed earlier, the ion source produces an intrinsic energy modulation which is coherent with the spin flip pattern. The systematic effect of energy modulation (and all other coherent beam properties originating at the source) changes sign in opposing beam line helicities. Thus, comparing results for A_z^{corr} according to beam line helicity should yield evidence of whether any residual ion source related systematic error is present in the final result. Table 3.26 summarizes the reduced and corrected analyzing power according to beam line helicity.

	Beam line +	Beam line −
$A_z^{reduced}$	$1.41 \pm 0.43(stat.)$	$1.90 \pm 0.39(stat.)$
ΔA_z	$0.40 \pm 0.06(syst.)$	$1.20 \pm 0.17(syst.)$
A_z^{corr}	$1.01 \pm 0.43(stat.)$	$0.70 \pm 0.39(stat.)$
$\Delta A_z(\Delta E)^\dagger$	$0.15 \pm 0.23(syst.)$	$-0.14 \pm 0.15(syst.)$
$A_z^{corr\dagger}$	0.86 ± 0.49	0.84 ± 0.45

Table 3.26: *Summary of A_z^{corr} according to beam line helicity in units of 10^{-7}. The row containing the $\Delta A_z(\Delta E)^\dagger$ term is a prediction of the systematic effect of coherent beam energy modulation using the method described in section 3.4.1. The row containing the $A_z^{corr\dagger}$ term includes a correction for the systematic effect of coherent beam energy modulation. NB This method produce a different systematic uncertainty, and therefore a different overall uncertainty, in the final than the method used in the final analysis.*

The $A_z^{corr\dagger}$ term represents the corrected analyzing power in the two beam line tunes after an energy modulation correction is applied. Although no correction is made for the systematic effect of coherent beam energy modulation

in the final analysis of the grand set, it is interesting to illustrate here the qualitative improvement in the result should such an error correction be attempted. The agreement of the results of the analysis of the reduced data from the two opposing beam line helicity tunes is striking. The result supports a conclusion that no significant systematic errors remain in the final result. And so, the final result of the complete analysis of the Feb97, Jul98, and May99 data runs, which is presented as the focus of this thesis, is

$$A_z = (0.84 \pm 0.29(stat.) \pm 0.17(syst.)) \times 10^{-7}\,, \quad \chi^2_\nu = 1.08.$$

Chapter 4

Conclusion

The parity violating longitudinal analyzing power, A_z, of $\vec{p}p$ elastic scattering at an incident proton energy of 221 MeV has been measured with the following results:

$$A_z = (0.84 \pm 0.29(stat.) \pm 0.17(syst.)) \times 10^{-7}$$

$$h_\rho^{pp} = (-25 \pm 10) \times 10^{-7} .$$

The above result is the focus of a review letter submitted by the TRIUMF E497 collaboration for publication at the time of writing [37]. The letter will summarize the results of this analysis and will be followed by a much longer, more detailed, account of the TRIUMF E497 experiment.

The main systematic uncertainty arises from uncertainty in the systematic effects of coherent beam position, size and energy modulation. The systematic shift in A_z due to the modulation of these beam parameters has been independently verified to be zero at the 10^{-8} level by regression analysis of the corrected data and external calibrations. The weak coupling constant, h_ρ^{pp}, has been calculated using equation 1.8, and its uncertainty is the scaled quadrature sum of the statistical and systematic error bars in A_z. Figure 4.1 shows a close up of the corrected A_z as a function of data set for the 23 sets. Figure 4.2 shows the final result for A_z at the $^1S_0$-$^3P_0$ zero crossing energy.

The TRIUMF E497 experiment has been successful in achieving a measurement of A_z at the $^1S_0$-$^3P_0$ zero crossing energy with a definite sign. The experimental result is somewhat larger than predicted by the meson exchange model based on the DDH prediction for h_ρ^{pp}. Unfortunately, the result for A_z is not at the level of precision the experiment was designed to obtain. This was due to the fact that insufficient statistics and unstable beam conditions exist in the final data set, which substantially limited the precision of the final result.

A new experiment being proposed at TRIUMF, E761 [38], will attempt to further constrain the value of the h_ρ^{pp} weak coupling constant by repeating the

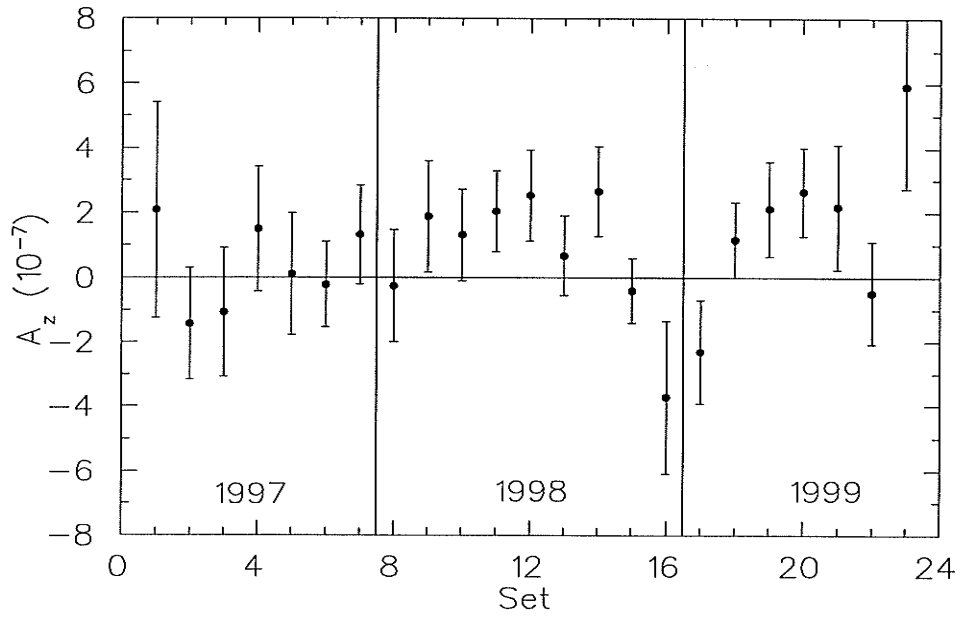

Figure 4.1: *A close-up of A_z^{corr} as a function of set. The reduced chi-squared of these data is 1.08. The data are not corrected for the systematic effects of coherent beam position, size and energy modulations.*

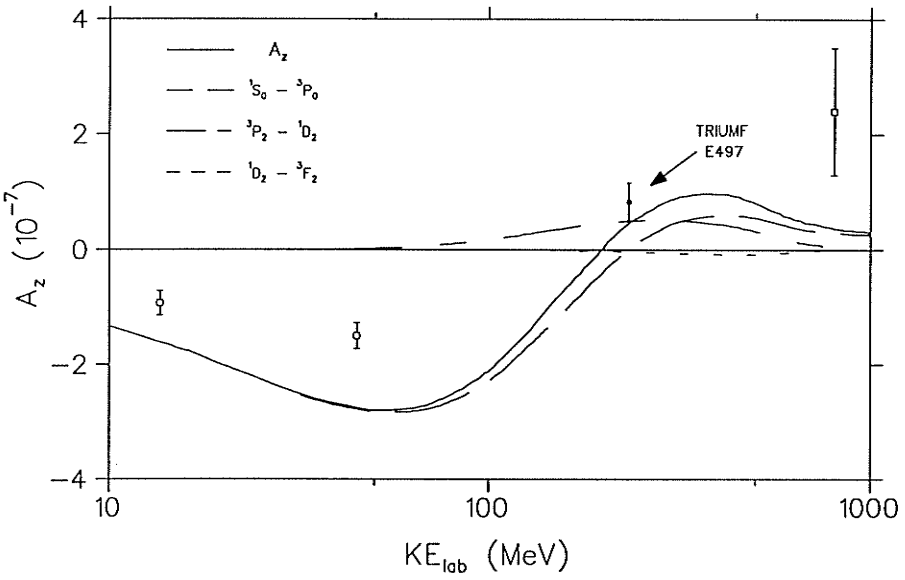

Figure 4.2: *The final result for A_z at the $^1S_0$-$^3P_0$ zero crossing energy. The TRIUMF E497 result is plotted against the DM theoretical curve alongside the other experimental results for A_z [8] [9] in the low and intermediate energy range.*

measurement of A_z at the $^1S_0$-$^3P_0$ zero crossing energy with the aim of reducing the total error bar to $\pm 0.2 \times 10^{-7}$. The new experiment will be conducted in the $4A/2$ beam line and will use new integrating polarimeters to improve the statistical resolution of transverse polarization parameters.

4.1 Systematic error discussion

One of the challenges encountered during the analysis of the grand set was the calibration of the systematic effect of helicity-correlated intensity modulation. It was found that the subtractor box drifted significantly during data taking, and this led to non-trivial error corrections to the measured A_z for the effect of correlated intensity modulation and significant data loss due to data quality cuts based on unstable sensitivity to CIM. E761 will attempt to improve on the performance of the subtractor module by using higher sensitivity V:F converters and implementing direct digital subtraction of the TRIC signals. This will lower the systematic effect of CIM by enabling the optimum fine gain adjustment to be made on the subtracted signal during offline analysis.

Another challenge in the analysis of the grand set was calibrating the effect of coherent beam size modulation. Unfortunately, the helicity-correlated beam size calibration never conclusively determined the sensitivity of the parity apparatus to the systematic effect of beam breathing. In the final analysis, an estimate based on the calibration studies and a regression of the real parity data was used in the calculation of the systematic uncertainty of A_z to this effect. An improvement in the quality of the calibration data may be obtained by imposing the coherent beam size modulation further upstream, possibly near the entrance to the $4A/2$ beam line, in order to observe the effect of the various bending magnets and beam line components on beam size modulation. It is also important to maintain a stable beam position during the beam size

calibration studies. This was not achieved during past studies due to the fact that the beam position feedback system could not be used to stabilize the beam position about the neutral axis at the same time.

Improvement in the measurement of A_z can be made by employing a more systematic approach to the calibration of the effect of coherent beam energy modulation. The sensitivity of the parity apparatus to this effect is very dependent on the cyclotron tune and should, therefore, be studied once or twice per day during regular data taking. Frequent measurements of the intrinsic energy modulation produced at OPPIS must also be maintained. Also, the E761 experimental collaboration has upgraded the polarization monitors to perform current mode measurements of the polarization profile of the beam. This has led to an ability to measure intrinsic first moments of polarization to, at least, 10X better resolution. These systematic improvements to the experimental process should enable the E761 collaboration to achieve a total uncertainty in A_z of $\pm 0.2 \times 10^{-7}$ in the same TRIC integration time as the data comprised by the grand set (300 hours of integration time).

4.2 Constraints on the values of h_ρ^{pp} and h_ω^{pp}

Figure 4.3 shows a graph of the experimental constraint on the value of h_ρ^{pp} against the DDH "best guess" and other theoretical predictions. It is evident that the present TRIUMF E497 result has significantly constrained the possible values of h_ρ^{pp} in contrast to a much wider range of theoretical predictions.

Figure 4.4 is a graph of the possible values of the weak coupling constants h_ρ^{pp} and h_ω^{pp} based on experimental constraints. The angled parallel lines in the graph show the possible values of h_ρ^{pp} and h_ω^{pp} based on two high precision measurements of A_z at lower energies and a calculation by AAH [2].

The future TRIUMF E761 experiment will attempt to reduce uncertainty

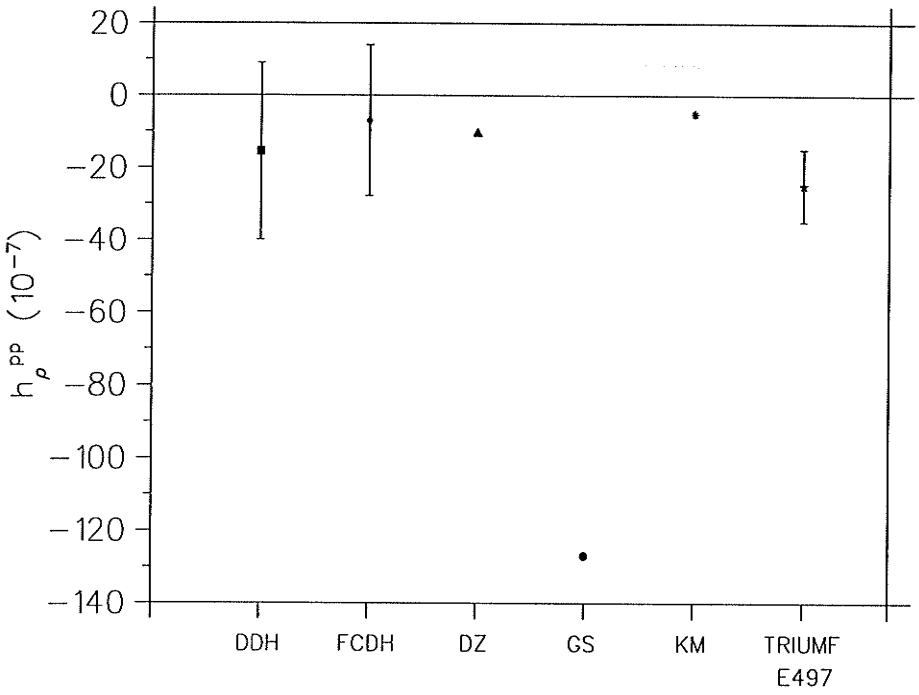

Figure 4.3: *The TRIUMF E497 result versus the DDH "best guess" and other theoretical predictions of the h_ρ^{pp} weak coupling constant. Included in the graph are predictions made by: Feldman, Crawford, Dubach, and Holstein [39] (FCDH); Dubovic and Zenkin [40] (DZ); Grach and Shmatikov [41] (GS); Kaiser and Meissner [42] (KM).*

in the measurement of A_z at the $^1S_0$-$^3P_0$ zero crossing energy and, therefore, the present uncertainty in h_ρ^{pp}. Much more experimental work in the low and intermediate energy sector, in addition to TRIUMF E761, is necessary in order to further constrain the values of the seven weak meson-nucleon coupling constants.

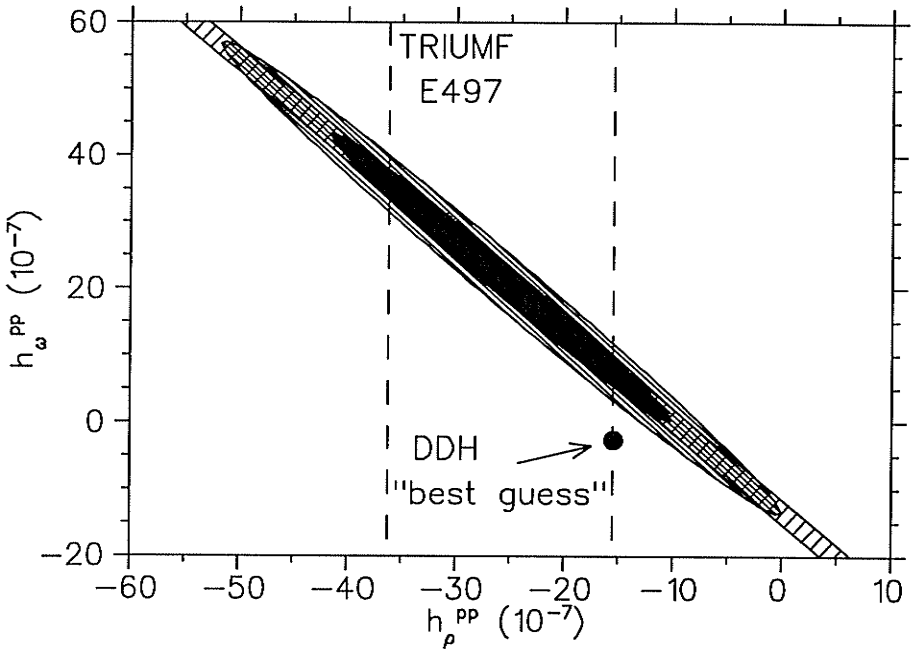

Figure 4.4: *Experimental constraints on the values of the weak coupling constants h_ρ^{pp} and h_ω^{pp}. The dashed vertical lines indicate the range of h_ρ^{pp} based on the TRIUMF E497 result presented in this thesis. The angled parallel lines indicate the range of possible values of h_ρ^{pp} and h_ω^{pp} based on the experimental results of the two high precision measurements of A_z [2] at 13.6 MeV and 45 MeV. The solid inner ellipse represents the limit of one standard deviation from the experimental mean values. The shaded outer ellipse represents the limit of two standard deviations from the experimental mean values. For contrast, the DDH "best guess" values of h_ρ^{pp} and h_ω^{pp} are indicated by the circle.*

References

[1] B. Desplanques, J. F. Donoghue, and B. Holstein. Ann. Phys. **124**, 449 (1980).

[2] Araz Alice Hamian. The measurement of parity violation in proton-proton scattering at 221 MeV. Ph.D. thesis, University of Manitoba, (1998).

[3] E. G. Adelberger and W. C. Haxton, Ann. Rev. Nucl. Sci. **35**, 501 (1985).

[4] C. Caso *et al.*, in *The European Physical Journal C* (Review of Particle Physics), edited by D. Haidt, P. M. Zerwas *et al.* **3**,1-4, pp. 25-26 (1998).

[5] S. A. Page, Phys. Rev. C **46**, 149 (1990).

[6] W. M. Kloet, R. R. Silbar, and J. A. Tjon, Phys. Rev. C **41**, 2263 (1990).

[7] B. Holstein. Phys. Rev. **D23**, 1618 (1981).

[8] P. D. Eversheim *et al.*, Phys. Lett. B **256**, 11 (1991).

[9] S. Kistryn *et al.*, Phys. Rev. Lett. **58**, 1616 (1987).

[10] V. Yuan *et al.*, Phys. Rev. Lett. **57**, 1680 (1986).

[11] D. E. Driscoll and G. A. Miller, Phys. Rev. C **39**, 1951 (1989).

[12] J. Birchall. *Energy for* $A_z(^1S_0\text{-}^3P_0) = 0$ (TRIUMF E497 internal report), 1995 (unpublished).

[13] M. Simonius, in *Interaction Studies in Nuclei*, edited by H. Jochim and B. Ziegler, (North Holland, Amsterdam, 1975), p. 3; in *High Energy Physics with Polarized Beams and Targets*, edited by C. Joseph and J. Soffer (Birkhauser Verlag, Basel, 1981), p. 355.

[14] J. Birchall and W. D. Ramsay, private communication, 2001.

[15] M. J. Iqbal and J. A. Niskanen, Phys. Rev. C **42**, 1872 (1990).

[16] M. J. Iqbal and J. A. Niskanen, Phys. Rev. C **49**, 355 (1994).

[17] S. A. Page *et al.* Measurement of the Flavor Conserving Hadronic Weak Interaction (TRIUMF Proposal E497), 1987 (unpublished).

[18] The photo was obtained from the E497 webpage on the TRIUMF website at *www.triumf.ca/E497/index.html.*

[19] A. N. Zelenski et al. Nucl. Inst. and Meth. **A334**, 285 (1993).

[20] P. G. Sona. Energia Nucl. **14**, 295 (1967).

[21] S. Diane Reitzner. A study and optimization of helicity-correlated beam properties generated from the TRIUMF optically pumped ion source for the parity violation experiment at 221 MeV. M.Sc. thesis, University of Manitoba, (1996).

[22] S. G. Kadantsev, C. D. P. Levy, M. M. Mouat, and A. N. Zelenski. The laser control system for the TRIUMF optically pumped polarized H^- ion source, in *Real Time Data Acquisition*, (1994).

[23] *TRIUMF Users Handbook*, unpublished.

[24] The photo was obtained from the TRIUMF website at *www.triumf.ca.*

[25] T. J. Stocki. Transverse field ionization chamber for the parity violation experiment at 230 MeV. M.Sc. thesis, University of Alberta, (1993).

[26] A. R. Berdoz et al. Nulc. Inst. and Meth. **A307**, 26 (1991).

[27] A. M. Sekulovich. Beam intensity profile monitor for a parity violation experiment at 230 MeV. M.Sc. thesis, University of Manitoba, (1989).

[28] A. R. Berdoz *et al.* Nucl. Inst. and Meth. **A457**, 288 (2001).

[29] D. Quarrie, CERN CDF Note No. 166 (V3.4), 1985 (unpublished).

[30] P. W. Green. *Introduction to the NOVA Data Analysis System*, 1991 (unpublished).

[31] R. J. Woo, private communication, 1999.

[32] A. Zelenski, private communication, 1998, and W. D. Ramsay, private communication, 2001.

[33] F. James, MINUIT Long Writeup, CERN Computer Centre Program Library, 1985 (unpublished).

[34] Louis Lyons, in *Statistics for nuclear and particle physicists* (Cambridge University Press, Cambridge, 1986), pp. 120-124

[35] W. D. Ramsay, private communication, 2001.

[36] J. Birchall, private communication, 2001.

[37] A. R. Berdoz *et al.* Phys. Rev. Lett.(to be published), 2001.

[38] J. Birchall *et al.* Parity violation in pp scattering (TRIUMF proposal E761), 1999 (unpublished).

[39] G. B. Feldman, G. A. Crawford, J. Dubach, and B. R. Holstein, Phys. Rev. C **43**, 863 (1991).

[40] V. M. Dubovic and S. V. Zenkin, Ann. Phys. **172**, 100 (1986).

[41] I. Grach and M. Shmatikov, ITEP preprint Moscow **100**, 52 (1988).

[42] N. Kaiser and U. G. Meissner, Nucl. Phys. **A499**, 699 (1989).